

1423
NPS63-89-003

NAVAL POSTGRADUATE SCHOOL

Monterey, California



FINAL TECHNICAL REPORT OF GRANT ATM 8610354
AIR FLOW OVER LARGE SCALE TOPOGRAPHY

by

Mary Alice Rennick

Roger T. Williams

June 1989

Final Report for Period 1 Oct 86 to 31 Mar 89

Approved for public release; distribution is unlimited.

Prepared for: National Science Foundation
Washington, D.C. 20550

FedDocs
D 208.14/2
NPS-63-89-003

**NAVAL POSTGRADUATE SCHOOL
Monterey, California 93943**

Rear Admiral R. W. West
Superintendent

H. Shull
Provost

The work reported herein was supported by the National Science Foundation, Division of Atmospheric Sciences, Global Atmospheric Research Program, under Grant ATM 8610354. Publication of the report does not constitute approval of the sponsor for the findings or conclusions. It is published for information and for the exchange and stimulation of ideas.

Reproduction of all or part of the report is authorized.

This report was prepared by:

REPORT DOCUMENTATION PAGE

DUDLEY KNOX LIBRARY
NAVAL POSTGRADUATE SCHOOL
MONTEREY CA 93943-5101

REPORT SECURITY CLASSIFICATION UNCLASSIFIED		1b RESTRICTIVE MARKINGS	
SECURITY CLASSIFICATION AUTHORITY		3 DISTRIBUTION/AVAILABILITY OF REPORT Approved for public release; distribution is unlimited.	
DECLASSIFICATION/DOWNGRADING SCHEDULE			
PERFORMING ORGANIZATION REPORT NUMBER(S) NPS-63-89-003		5 MONITORING ORGANIZATION REPORT NUMBER(S)	
NAME OF PERFORMING ORGANIZATION Naval Postgraduate School	6b OFFICE SYMBOL (if applicable) 63	7a NAME OF MONITORING ORGANIZATION	
ADDRESS (City, State, and ZIP Code) Monterey, CA 93943		7b ADDRESS (City, State, and ZIP Code)	
NAME OF FUNDING/SPONSORING ORGANIZATION National Science Foundation	8b OFFICE SYMBOL (if applicable) GARP	9 PROCUREMENT INSTRUMENT IDENTIFICATION NUMBER ATM8610354	
ADDRESS (City, State, and ZIP Code) Washington, DC 20550		10 SOURCE OF FUNDING NUMBERS PROGRAM ELEMENT NO PROJECT NO TASK NO WORK UNIT ACCESSION NO	
TITLE (Include Security Classification) Air Flow over Large Scale Topography (U) (Technical Report of Grant ATM 86 10354)			
PERSONAL AUTHOR(S) Rennick, Mary Alice, and Williams, Roger T.			
TYPE OF REPORT Final	13b TIME COVERED FROM 86/10/1 TO 89/3/31	14 DATE OF REPORT (Year Month Day) 1989, June	15 PAGE COUNT
SUPPLEMENTARY NOTATION			
COSAT CODES ELD GROUP SUB-GROUP		16 SUBJECT TERMS (Continue on reverse if necessary and identify by block number) Topographic Effects cyclones Fronts	
This project studied the following two aspects of topographic influence on transient atmospheric motions:			
1) <i>Lee Cyclogenesis.</i> It is observed that cyclones frequently form on the lee side of mid-latitude mountain ranges. This problem is investigated with a long mountain range which is perpendicular to a vertically sheared basic current. The prediction equations are solved with both analytic and numerical methods. It is found that lee cyclogenesis can be partially explained by a superposition effect involving a counterclockwise rotating cyclone and a clockwise rotation circulation forced by the mountain range.			
2) <i>Effects of topography on fronts.</i> It is often observed that fronts are strongly affected by topography. A two-dimensional numerical model is used for this study. The model predicts the formation of fronts through the effects of a confluent horizontal wind field. When a front is placed on the upwind side of a mountain range, it weakens relative to the no-mountain solution as it moves up the slope, and it strengthens as it moves down the lee slope. The collapse of a front to very small scales is studied with a non-hydrostatic numerical model. It is found that this process excites gravity waves.			
DISTRIBUTION/AVAILABILITY OF ABSTRACT UNCLASSIFIED/UNLIMITED <input checked="" type="checkbox"/> SAME AS RPT <input type="checkbox"/> DTIC USERS		21 ABSTRACT SECURITY CLASSIFICATION UNCLASSIFIED	
NAME OF RESPONSIBLE INDIVIDUAL Roger T. Williams		22a TELEPHONE (Include Area Code) (408)646-2296	22b OFFICE SYMBOL 63WU

FORM 1473, 64 MAR

83 ARK edition may be used until exhausted
All other editions are obsolete

SECURITY CLASSIFICATION OF THIS PAGE

unclassified

Table of Contents

1. Scientific Collaborators
2. List of Publications
3. Thesis (abstract)
Numerical Investigation of Orographically Enhanced Instability, G.T. Byrne (1987)
4. Reprints
Gravity Waves Generated during Frontogenesis, R.L. Gall, R.T. Williams and T.L. Clark, (1988)
On the Minimum Scale of Surface Points, R.L. Gall, R.T. Williams and T.L. Clark, (1987).
Lee Cyclogenesis. Part I: Analytic Studies, J.L. Hayes, R. T. Williams and M. A. Rennick (1987).
5. Preprint
Lee Cyclogenesis: Part II: Numerical Studies, J.L. Hayes, R. T. Williams and M. A. Rennick (1989).
6. Initial Distribution List

1. Scientific Collaborators

Captain Gerald T. Byrne, USAF, graduate student, Naval Postgraduate School

Dr. Robert L. Gall, Professor of Atmospheric Science, Institute of Atmospheric Physics, University of Arizona

Mrs. Olivera Haney, Meteorologist, Naval Postgraduate School

Dr. David J. Knight, Assistant Professor of Atmospheric Sciences, State University of New York at Albany.

Dr. Melinda S. Peng, Adjunct Research Professor, Naval Postgraduate School

2. List of Publications

- Byrne, G. T., 1987: Numerical investigation of orographically enhanced instability, M.S. Thesis, Naval Postgraduate School, 59 pp.
- Gall, R. L., R. T. Williams and T. L. Clark, 1987: On the minimum scale of fronts. *J. Atmos. Sci.*, **44**, 2562-2574.
- Gall, R. L., R. T. Williams and T. L. Clark, 1988: Gravity waves generated during frontogenesis. *J. Atmos. Sci.*, **45**, 2204-2219.
- Hayes, J. L., R. T. Williams and M. A. Rennick, 1987: Lee Cyclogenesis, Part I: Analytic Studies. *J. Atmos. Sci.*, **44**, 432-442.
- Hayes, J. L., R. T. Williams and M. A. Rennick, 1989: Lee Cyclogenesis, Part II: Numerical Studies. Submitted to *J. Atmos. Sci.*
- Williams, R. T., M. S. Peng and D. A. Zankofsky, 1989: Effects of fronts on topography. (in preparation).

Numerical Investigation of Orographically
Enhanced Instability .

. by

Gerald T. Byrne
Captain, United States Air Force
B.S., Drexel University, 1974

The NEPRF spectral baroclinic primitive equation with six layers was numerically integrated over time to examine the effects that vertical wind profiles have on the development of lee cyclogenesis. In addition, the model was run in both linear and nonlinear modes to isolate their effects on the tests. The objective was to simulate a cold front moving over a high mountain ridge, similar to the Alps or Rockies, by implementing a wind reversal profile to determine if this was conducive to lee cyclogenesis. It was found that the wind reversal profile produced favorable cyclonic growth, particularly when the model was in a linear mode. A nonlinear wind reversal test also produced positive results but only for a relatively short time; thereafter nonlinear interactions dampened cyclonic growth considerably. In addition, two tests were run that allowed the mountain to grow in a very short time to isolate inertial gravity wave interactions. The gravity waves did produce considerable oscillations in the two tests, but after 15 hours or so these two tests showed similar cyclonic growth to the previous tests.

Master of Science in
Meteorology
September 1987

Advisor: R.T. Williams
Department of
Meteorology

Classification of Thesis:
Unclassified

Gravity Waves Generated during Frontogenesis

R. L. GALL

Institute of Atmospheric Physics, The University of Arizona, Tucson, Arizona

R. T. WILLIAMS

Dept. of Meteorology, Naval Postgraduate School, Monterey, California

T. L. CLARK

National Center for Atmospheric Research, Boulder, Colorado*

(Manuscript received 17 June 1987, in final form 22 February 1988)

ABSTRACT

Gravity waves forced by nonhydrostatic and nongeostrophic processes within a frontal zone are discussed. In particular, stationary waves immediately above and below the surface front are considered.

The waves that appear above the front are horizontally stationary with respect to the front, but are vertically propagating. The vertical wavelength here is given by $2\pi v/N$, since the waves are nearly hydrostatic.

The horizontal wavelength of the waves above the front is determined by standing waves that set up below the front. These waves corrugate the frontal surface, and these corrugations, in turn, determine the horizontal scale of the waves above the front.

The waves under the front are standing and are trapped between the earth's surface and the frontal zone which, due to its conditions of flow reversal and small Ri , is assumed to be a reflector of gravity waves. The horizontal scale of the standing waves is determined by their vertical wavelength and the slope of the frontal surface. These waves are shown to break, and additional stationary waves appear above each of the breaking zones.

We suggest that the waves described here might account for some of the banding seen in satellite images of frontal zones.

Introduction

Perhaps one of the most striking features of satellite images in frontal regions is the banded nature of the clouds. Almost any picture of a frontal region reveals long thin streaks of clouds, more or less parallel to the front itself and extending from hundreds to a thousand kilometers or more. Figure 1 shows two such images and emphasizes examples of different types of banding that can often be seen associated with fronts.

There have been a number of suggestions to explain at least some of the banded features associated with fronts, though not necessarily the banded features in the clouds themselves. Most of the explanations involve the banded structure observed within the precipitating parts of the front. Houze and Hobbs (1982) summarize

some of the details of these features. Perhaps the most widely accepted explanation of bands is that the flow within the frontal zone is unstable with respect to symmetric overturnings and that the waves so generated organize the precipitation and clouds into parallel lines. Extensive discussions of the role of the symmetric instability (or slantwise convection) in the rainbands of frontal regions is available in papers by Bennetts and Hoskins (1979) and Emanuel (1983a,b).

We have little difficulty in accepting these concepts for those regions of the front where there is precipitation. In those regions, the conditions necessary for the onset of symmetric instability can be established by the release of latent heat. Hoskins (1974) has shown that negative regions of potential vorticity are necessary for symmetric instability. Since potential vorticity is usually positive in the atmosphere, diabatic or viscous processes are necessary to set off symmetric instability. In frontal regions, the primary diabatic heat source is due to latent heat release, and thus it appears that precipitation is necessary before this form of instability can appear. Emanuel (1983b) has demonstrated that it is possible that symmetric overturnings occur in some fronts.

* The National Center for Atmospheric Research is sponsored by the National Science Foundation.

Corresponding author address: Dr. Robert L. Gall, Institute of Atmospheric Physics, University of Arizona, Building #81, Tucson, AZ 85721.

There are, however, considerable problems with associating symmetric instability with cloud features in portions of the front where there is little precipitation. For example, the portions of the cold front well south of the surface low often have little precipitation, but comprise a region where banded clouds are often seen. Good examples of banded features well south of the surface low along fronts off the coast of California are shown in Fig. 1. In this region, ocean temperatures are cool, thus the atmosphere is convectively stable, further suggesting a lack of precipitation along this portion of the front. Due to the lack of precipitation, symmetric instability is an unlikely cause of the banding.

An alternative mechanism is gravity waves generated during frontogenesis. Ley and Peltier (1978), using the Hoskins and Bretherton (1972) model of frontogenesis, demonstrated that the nongeostrophic and nonhydrostatic accelerations in the region of increasing temperature gradient will generate gravity waves whose amplitudes at large distance from the front are comparable to oscillations observed in the surface pressure field ahead of fronts. They did not examine details of the waves in the vicinity of the front, so little could be said from their results concerning the banding of the clouds in these regions.

Lindzen and Tung (1976) discussed the role of gravity waves in organizing convection into bands especially in the vicinity of fronts. Much of this discussion centered on the role of convection in first generating the waves, and the waves, in turn, influencing the convection. However, some of the concepts they develop can be used to examine the properties of the waves generated by other means in frontogenesis, and we will use these in the subsequent discussion.

In this paper, we will examine the waves generated by the front discussed in a companion paper (Gall et al. 1987). In that paper, we described a numerical simulation of frontogenesis forced by stretching deformation. In the results reported there, a nesting procedure allowed very high horizontal and vertical resolution in frontal regions. Primary interest in that paper was the minimum scale of the simulated front. The primary result was that the minimum scale of the front was determined by the horizontal and vertical resolution of the model, even at the highest resolution. (A horizontal grid spacing of 280 m and a vertical spacing of 35 m).

2. The model

Details of the model are available in Gall et al. (1987). Therefore, we will only outline its features. The model is the nonhydrostatic model described by Clark (1977). The model uses a terrain-following coordinate system although, in the calculations reported here, the terrain height everywhere is zero. The model allows up to three levels of nesting, details of which are given in Clark and Farley (1984). We used this nesting to

achieve very high horizontal and vertical resolution in the vicinity of the surface front. Resolutions used in the experiments and the location of the inner nested models are available in Gall et al. and Table 1.

Initial conditions were those used by Williams (1972) and included a constant vertical static stability and a horizontal temperature distribution given by

$$\theta(y, z, 0) = \frac{\partial \theta_I}{\partial z} (z - H/2) - a(2/\pi) \arctan(\sinh \alpha y) \quad (1)$$

where

$$\alpha = f\pi H^{-1}(g\theta_0^{-1}\partial\theta_I/\partial z)^{-1/2}$$

$$f = 10^{-4} \text{ s}^{-1}, \quad \frac{\partial \theta_I}{\partial z} = 4 \text{ K km}^{-1}$$

$$H = 9 \text{ km}, \quad g\theta_0^{-1} = 0.033 \text{ m s}^{-2}/\text{K}.$$

In these simulations, any variations of perturbation quantities (or time-dependent quantities) in x (perpendicular to the temperature gradient) are neglected. The initial component of the wind parallel to x is computed from the geostrophic relation.

An initial vertical wind component and a wind component parallel to the horizontal temperature gradient are computed from the quasi-geostrophic circulation equation

$$\frac{g}{\theta_0 f^2} \frac{\partial \theta_I}{\partial z} \frac{\partial^2 \psi}{\partial y^2} + \frac{\partial^2 \psi}{\partial z^2} - \frac{1}{\rho_0} \frac{\partial \rho_0}{\partial z} \frac{\partial \psi}{\partial z} = \frac{2Dg\rho_0}{f^2 \theta_0} \frac{\partial \theta}{\partial y} \quad (2)$$

where ψ is the streamfunction for the ageostrophic flow perpendicular to the front. This latter condition pre-

TABLE 1. The various models used in the experiments. The Dy and Dz are the horizontal and vertical resolution, respectively, in km. Initial conditions denote the experiment from which the initial conditions are taken at the time indicated by the start time. Start time is in minutes from the introduction into experiment 1 of the initial conditions specified in the text.

Experiment		Dy	Dz	Initial condition	Start time
Single models					
1		20	.32	—	0
2		10	.32	1	1450
3		5	.32	2	2050
4		2.5	.32	3	2550
5		5	.16	3	2050
Doubly nested					
6	outer	2.5	.32	3	2250
	inner	.83	.11	3	2250
Triply nested					
7	outer	2.5	.32	6	2450
	middle	.83	.11	6	2450
	inner	.28	.04	6	2450

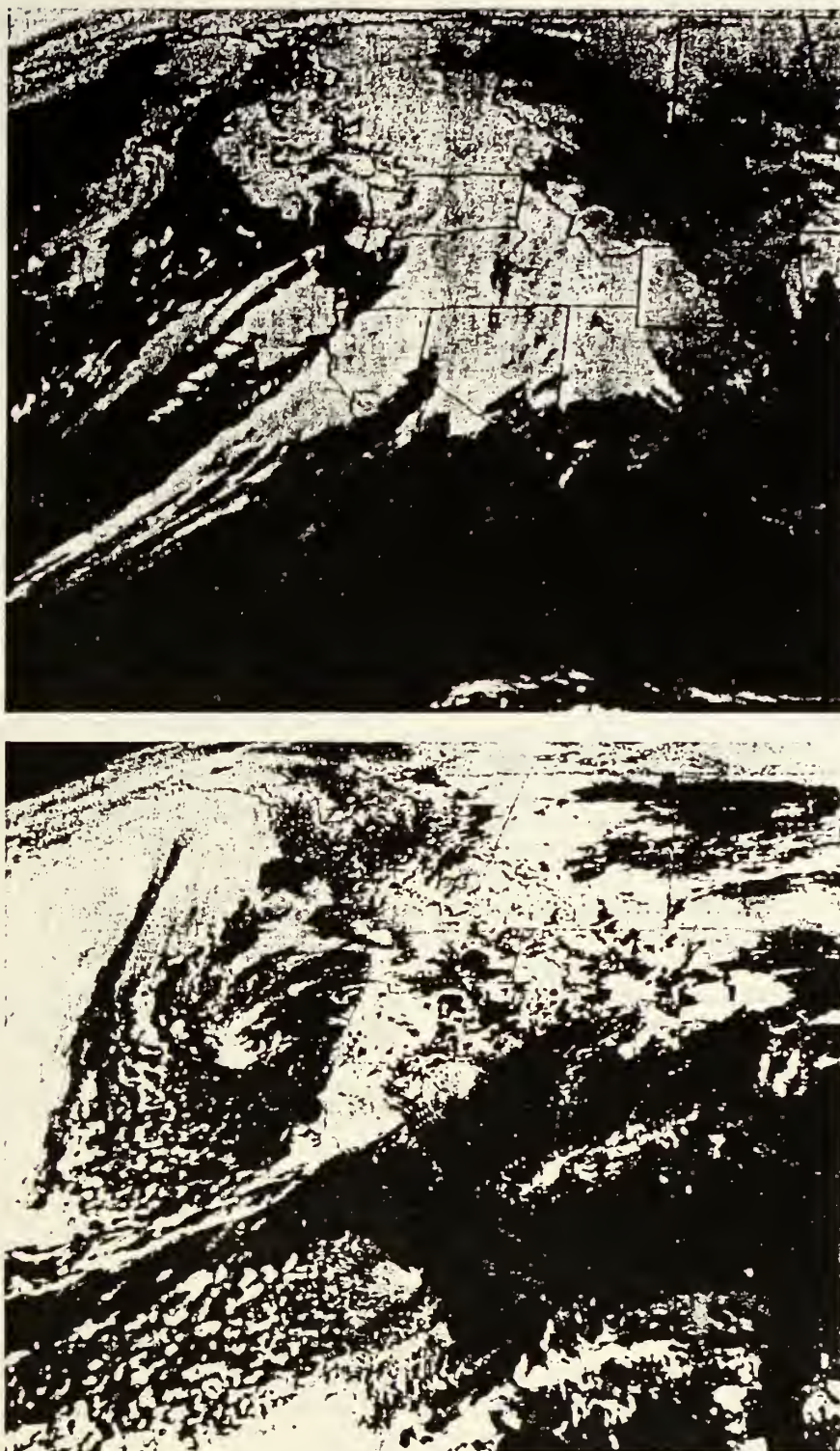


FIG. 1. Satellite images from GOES illustrating examples of cloud banding along fronts. Upper figure is an infrared image at 2130 UTC 22 January 1985. Lower figure is a visible image taken at 2100 UTC 28 May 1985.

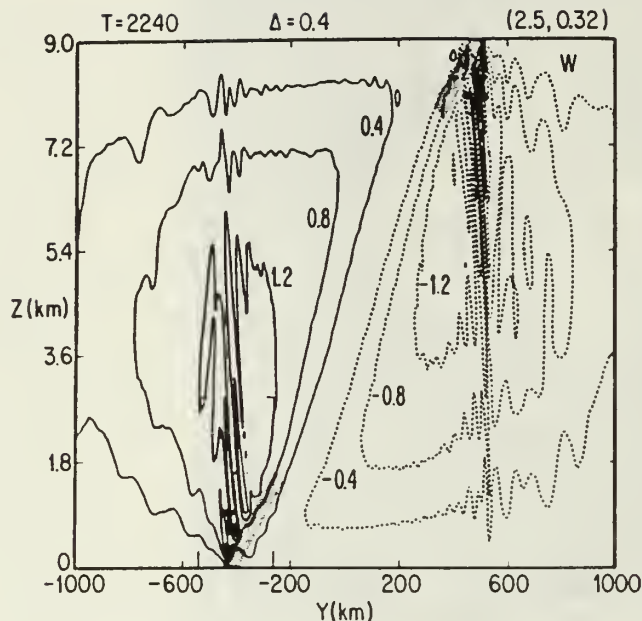


FIG. 2. Vertical velocity at $T = 2240$ min from the beginning of the experiment. The experiment that produced this figure had a horizontal resolution of 2.5 km and a vertical resolution of 320 m. This information is indicated within the parentheses where (D_Y, D_Z) is the convention. D denotes the contour interval in cm s^{-1} . The shaded region delineates the region of large temperature gradient that is the frontal zone.

vents an initial development of large-scale gravity waves. This is important for the results to be reported here, since we are concerned with the gravity-wave production by the front itself and not the initial conditions. Using Eq. (2), we found virtually no gravity-wave production early in the experiment, as opposed to runs where the across-front and vertical wind components were initially set to zero.

In addition to time-dependent wind components, a time-independent flow given by

$$\psi_0 = -Dxv \quad (3)$$

is included, where we take $D = 10^{-5} \text{ s}^{-1}$. It is this deformational flow that forces the front. Thus, we are considering the type of front forced by stretching deformation.

All runs were inviscid: thus there were no effects of surface stress. All simulations were dry and adiabatic. Table 1 summarizes the experiments that were performed and indicates resolution used and models used to initialize the various higher resolution experiments. The locations of the inner models used in the nested experiments are shown in Fig. 2 of Gall et al. In the discussion that follows, we will report results from whichever experiment shows a particular point most clearly. In all cases, the results of the various experiments were very similar, except that the higher reso-

lution experiments showed more detail in the frontal zone.

Numerical procedures were described in detail in Clark (1977). They were mostly standard centered differences where momentum, mass and energy integrals are conserved. The thermodynamic equation, however, was approximated using the second-order-in-time-and-space scheme of Smolarkiewicz (1983, 1984).

3. Waves in the frontal region

Figure 3 shows the vertical motion computed in our simulations at a time approximately 4 h before we estimate that the frontogenesis would first form a discontinuity at the surface in a semigeostrophic model (see Gall et al.). This particular figure shows only a portion of the total domain considered in the simulation that had a vertical resolution of 320 m and a horizontal resolution of 2.5 km. The total domain extended from $y = -1800$ km to $y = 1800$ km. In this figure, the surface front is located near $y = -450$ km, while the front on the upper surface is near $y = 500$ km. The overall pattern of descent on the right of the figure and ascent on the left is the familiar pattern observed for this form of frontogenesis (by stretching deformation).

Superimposed on the large-scale motion is considerable wave activity. From this point on, we will just discuss those features associated with the surface front since, in these simulations, the upper and lower fronts are very nearly identical. Over the surface front, there are a series of waves that are strongest just above the front and have phase lines that tilt, with height, into the across-front flow above the front. Recall in these simulations that there is a flow given by Eq. (3) from left to right up to $y = 0$ on the left-hand side of the figure and from right to left up to $y = 0$ on the right-hand side of the figure. The sum of the flow given by Eq. (3) and the secondary circulations forced by the front is shown in Fig. 4. We will show later that these waves are stationary with respect to the front and share properties with the waves that form over mountains.

Under the front, there are waves that are just barely visible in the figure, which are apparently standing waves. They form between the frontal surface and the lower boundary. We will show better pictures of these waves later.

Finally, there is considerable wave activity to the warm side of the surface front and to the cold side of the upper front. These waves are most clearly visible to the right of the upper front. In the space between the two fronts (from $y = -200$ to $y = 200$ km), there is very little wave activity.

In this paper, we will discuss only those waves directly above and below the surface front. These two classes of waves appear to be interdependent, thus it is natural to discuss them together. On the other hand, the dynamics of the waves ahead of the surface front

appear to be quite different and mostly independent of the presence of the waves near the front. In the interest of brevity, we will reserve a discussion of the waves ahead of the front to another paper.¹

In the discussion that follows, we will be drawn to the conclusion that the waves shown in Fig. 2 are gravity waves generated by imbalances in the frontal zone. One criticism of this notion is that, as the frontogenesis proceeds, very large shears will develop, and this in turn will lead to the development of Kelvin–Helmholtz waves, which may account in some way for all the waves shown in Fig. 2. Indeed, for the shear of the along-front wind, Richardson numbers less than 0.25 are eventually produced in a narrow region along the frontal zone extending from the surface up to about one kilometer. The phase lines of waves generated by the along-front shear would be perpendicular to this shear, however, and the two-dimensional constraint of these experiments precludes the development of these waves. The across-front shear can lead to shear generated waves in this experiment; however, this shear is an order of magnitude less than the along-front shear and only in a very small region at the surface does the Richardson number for this shear become less than 0.25. Since Kelvin–Helmholtz waves are confined to the region of Richardson less than 0.25, this type of instability cannot account for the waves observed in these experiments. Furthermore, for the reasons cited in the Introduction, since the flow is adiabatic and inviscid, neither can symmetric instability account for the waves.

¹ During the review process, one of the reviewers reported that, in frontogenesis experiments he had run that were similar to those reported here, extensive and apparently spurious wave generation occurred whenever the ratio of Dz to Dy in his model was not equal to the frontal slope. The reason, it was argued, was because the thermal wind balance could not be maintained when the frontal scale became equal to the grid spacing in one dimension and not the other and hence copious production of gravity waves would result. Indeed, results shown to us by that reviewer indicated that wave production was higher when Dz/Dy did not equal the frontal slope, although there still was significant wave production when the two were equal. At the rather low horizontal resolution used by the reviewer, the high wave production when Dz/Dy did not equal the frontal slope led to very noisy looking fields.

In the results reported here, Dz/Dy is not equal to the frontal slope. In fact, it is less by at least a factor of two for the lowest horizontal resolution and is even smaller for higher horizontal resolution. Thus the reviewer felt that, in order to demonstrate that our results are not due to a spurious production of waves resulting from the truncation, we should perform at least one experiment where Dz/Dy equals the frontal slope. These experiments are difficult and costly because of the large number of grid points that are required when the horizontal spacing is small. Nevertheless, we were able to try one experiment with a horizontal grid spacing of 10 km and a vertical spacing of 75 km that provides a ratio exactly equal to the frontal slope in this experiment. While the intensity of the waves generated by the front in this new experiment was less than reported here, the waves were otherwise quantitatively the same. The waves reported here were all present and had the same vertical and horizontal scales.

4. Stationary waves over the front

Figure 3 shows vertical velocity in a small region in the immediate vicinity of the surface front. In this figure, the surface position of the front is located near $y = -450$ km, and the upper edge of the region of high temperature gradient (indicated by the shaded region) is located just below the nodes of regularly spaced maxima that slant upward and to the left in the figure. Each of the three panels in Fig. 3 are at different times and so illustrate how the waves develop with time. Note that the waves above the front appear first near the point where the front intersects the surface and, with time, they extend upward away from the frontal surface and backward along it. The regular pattern associated with these waves ends abruptly over the nose of the front, as one moves toward the warm air at any level. Examination reveals that the phase lines of the waves tilt toward the left with height.

All of the features just mentioned are consistent with horizontally stationary, hydrostatic gravity waves propagating energy away from their source, which lies on the interface of the frontal zone. The horizontal wavelength of these nontrapped waves is about 50 km, suggesting negligible nonhydrostatic effects. For waves stationary with respect to the front, hydrostatic waves will appear only above the source, which would account for the sharp edge to the wave activity over the surface intersection of the front. If the front is the source, the waves must have propagated with a vertical component of group velocity upward away from the front for waves to appear above the front; and it is well-known that gravity waves stationary with respect to the flow and having a source at or near the ground will have phase lines tilting into the flow with height.

Figure 4 shows the total across-front velocity near the front. The frontal surface lies along the line of zero velocity. Above the front, flow is directed from warm to cold air, while the reverse occurs below the front. Since the flow is nonzero above the front, stationary waves are possible, and their phase lines must tilt toward the left in our figure, since the phase velocity must be into the flow or toward the warm air.

For hydrostatic stationary waves, the vertical wavelength is given by

$$L_z = \frac{2\pi v}{N}, \quad (4)$$

where v is the total across-front velocity and N is the Brunt–Väisälä frequency. Figure 5 shows L_z computed from Eq. (4) for the region shown. Note that in the frontal zone where v is zero, L_z is as well. Above the front, L_z increases with height simply because v increases; in this region, N is very nearly constant. The vertical wavelength of the stationary waves is about 2 km at an altitude of 3 km, which agrees well with the vertical wavelength of the waves in Fig. 3. Furthermore, this wavelength increases with height. A careful ex-

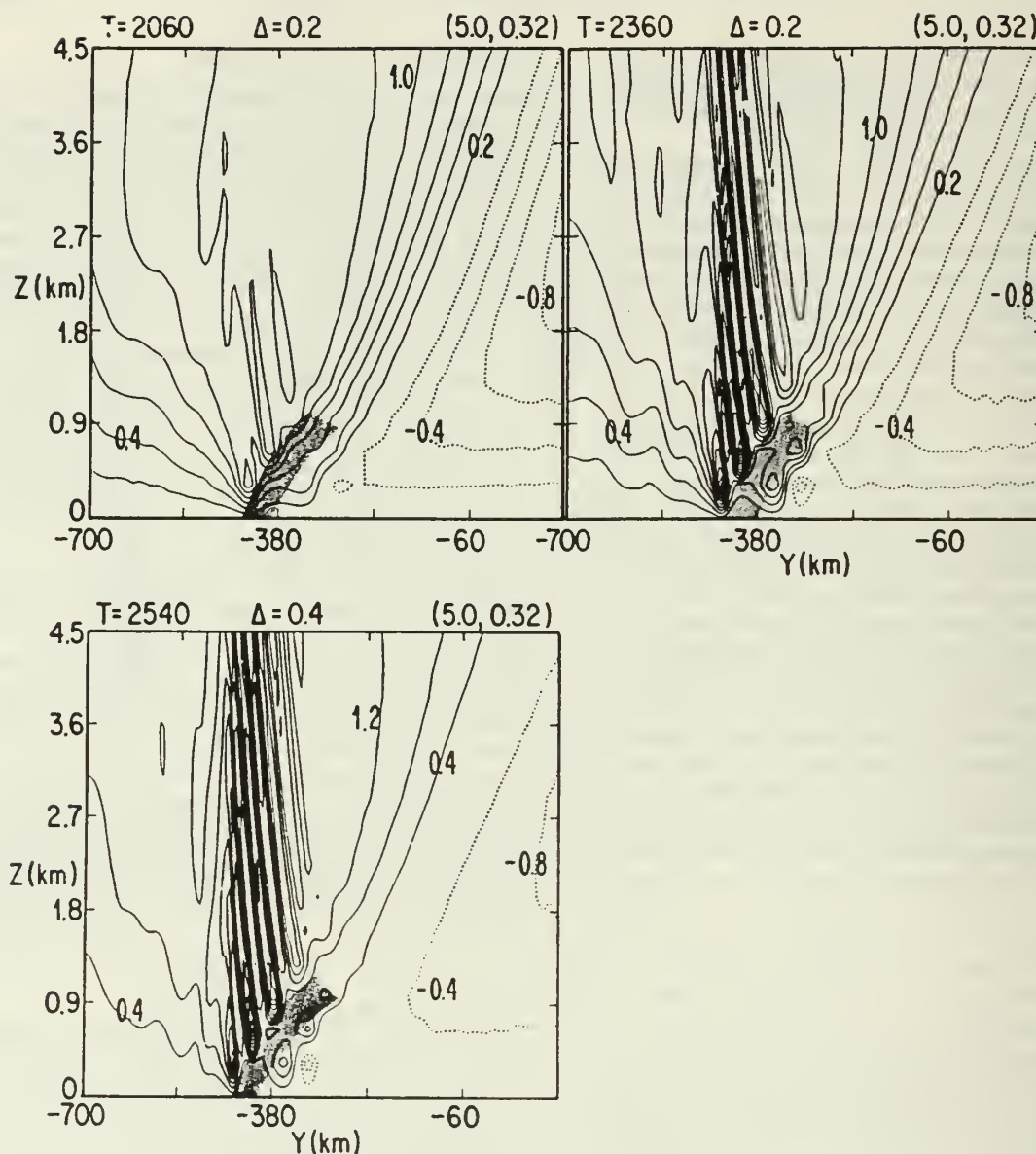


FIG. 3. As in Fig. 2 except at various times in a smaller region.

amination of the waves in Fig. 3 shows that the phase lines curve upward.

It is well known that, when there are small-scale, nongeostrophic or nonhydrostatic imbalances, gravity waves will be generated. Such imbalances are expected within frontal surfaces (see Ley and Peltier 1978), since the processes that are forcing the temperature gradient to grow ever stronger during the frontogenesis maintain mass and momentum fields slightly out of balance with one another. It is these imbalances that also force the secondary circulations associated with fronts. Figure 6 shows the development of the nongeostrophic and nonhydrostatic accelerations in the frontal zone in our simulations. Note that these two accelerations, which are about of the same magnitude, are confined to the

frontal zone, are strongest just behind the position of the leading edge of strong temperature gradient at the surface (near $y = -450$ km), and diminish upward along the front. These accelerations increase with time at all levels, which makes the pattern in Fig. 6 appear to develop upward along the frontal surface. This latter point is visible only for the nonhydrostatic accelerations. The waves discussed above are nongeostrophic, thus they dominate the nongeostrophic acceleration fields at the later time. The waves are hydrostatic; therefore, they do not appear in the fields of nonhydrostatic accelerations.

Since these accelerations are confined to the frontal region, there is a clear source for gravity waves confined to that region. This forcing increases with time and is

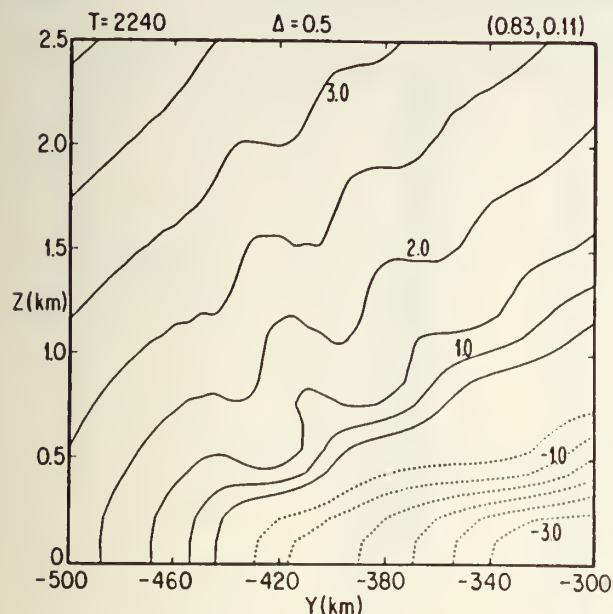


FIG. 4. Total horizontal across-front wind, v (m s^{-1}), parallel to the cross section. This velocity includes both the flow due to the large-scale deformation [Eq. (3)] and that due to the circulation induced by the frontogenesis. Dotted lines are negative. The zero line passes approximately halfway between the dashed and solid lines. Frontal surface is along the zero line. The Δ denotes the contour interval m s^{-1} , and the parentheses show resolution of the model as in Fig. 2.

strongest at the point where the front intersects the surface. Thus the stationary waves forced by these accelerations will appear first near the point of the surface intersection of the front and later further back along the frontal surface as the accelerations there increase. The apparent upward development of the waves visible in Fig. 3 simply marks the upward progression of the group after its initial forcing within the front.

Figure 7 shows correlations $v'w'$, $u'w'$ and $T'w'$ in a small region just above the surface front. Here the prime denotes a deviation of the quantity from the linear trend at a given level between the boundaries of the domain shown in Fig. 7. By defining the prime in this way, variations due mostly to the waves can be isolated, and any variations due to the front itself are mostly excluded.

If the waves considered here are indeed gravity waves, then v' and w' must be negatively correlated, since the phase lines for stationary waves in a flow that enters from the left of the figure must tend to the left with height. In other words, the waves carry negative across-front momentum away from the frontal zone. On the other hand, quantities such as potential temperature and along-front velocity should be uncorrelated with w' in a gravity wave which is independent of the along-front direction, as here. Figure 7 clearly shows the correlations we expect to find in gravity waves that would be stationary above the front.

Thus, to summarize, the waves above the surface front (and below the front on the upper surface) are stationary, hydrostatic gravity waves forced by non-geostrophic and nonhydrostatic accelerations in the frontal zone. Since these waves are hydrostatic, they appear only above the front, and their vertical wavelength is given by $L_z = 2\pi v/N$. These waves are simply the equivalent of the wave that appears over a mountain when the mountain scale is large enough for the waves to be hydrostatic. Here, however, the forcing is much more monochromatic than for mountains.

In this discussion, we have not mentioned so far any process that may determine the horizontal wavelength of the waves above the front. Figure 3 shows a unique horizontal wavelength for these waves; thus the scale-selection mechanism that determines this wavelength must be *very selective*. We can find no natural mechanism in the flow above the front or in the frontal zone itself that can be so selective, so we must turn to processes occurring below the frontal surface for such a mechanism.

5. Standing waves under the front

Figure 8 shows a smaller region of the zone near the surface intersection of the front from the inner model of the experiment with two levels of nesting. In these figures, the horizontal resolution is 830 m and the vertical resolution is 110 m. The figure showing potential temperature will help in defining just where the frontal zone is located.

In these figures, the waves above the front are visible. With the increased vertical resolution on the intro-

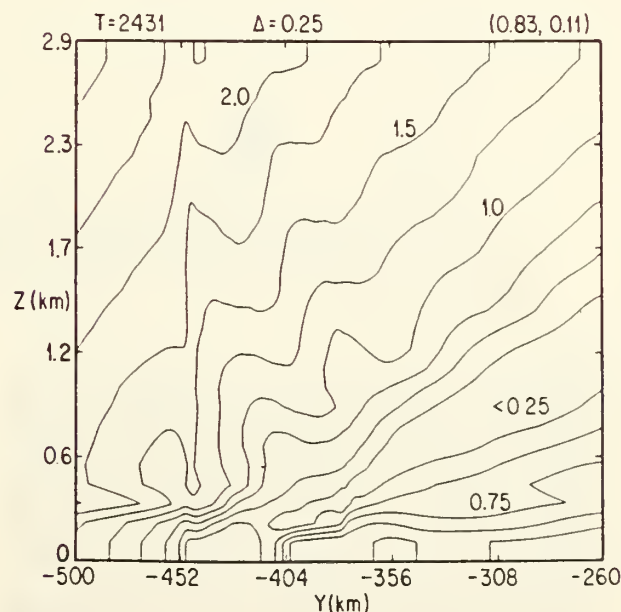


FIG. 5. Vertical wavelength (km) of the stationary wave. Frontal surface lies in the region of values less than 0.25. Otherwise same as Fig. 2.

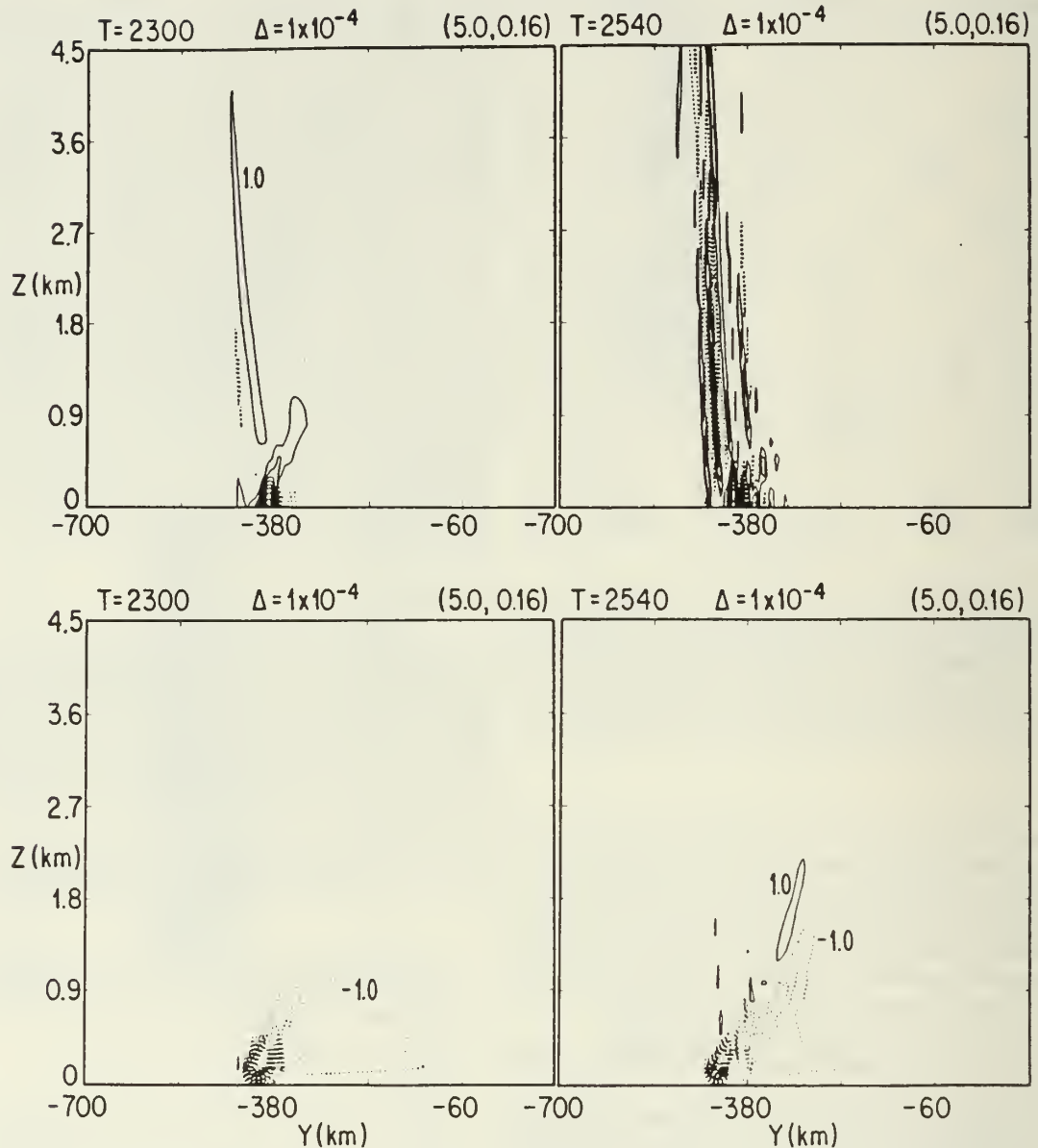


FIG. 6. The nongeostrophic acceleration (dw_{ox}/dt) at two times, upper figure, and the nonhydrostatic acceleration ($dw/dt + 2\Omega u \cos\theta$), at the same times, lower figures. The Δ denotes the contour interval in m s^{-2} . Parentheses denote resolution of the model used as in Fig. 2. Contour labels are $\times 10^{-4} \text{ m s}^{-2}$.

duction of the inner model, there is a readjustment of the intensity of the front at the surface and at its nose. This readjustment results in the generation of a strong wave with fairly small horizontal scale at the nose that is clearly visible in the lower right-hand panel of Fig. 8. We regard this wave as an artifact of the numerical procedure, i.e., spawning a higher resolution model results in initialization effects.

Just below and to the cold-air side of the frontal surface, a circulation or wave feature that increases with time is apparent. The upper left-hand panel shows the ageostrophic across-front flow and can be used, along with the vertical velocity in the panel below, to

delineate the circulation feature. In addition, the dashed line in the upper-left figure connects minima and maxima in the waves in the geostrophic across-front flow and illustrates an apparent connection between the waves above the front and the circulations or waves developing below the front. In particular, the horizontal scale of the wave below the front appears very similar to that in the waves above the front. The waves below the front are also clearly visible in Fig. 3. Note that the phase lines of these waves are either vertical or horizontal, and in Fig. 3 successive waves to the right of the surface intersection of the front contain an additional half wavelength in the vertical.

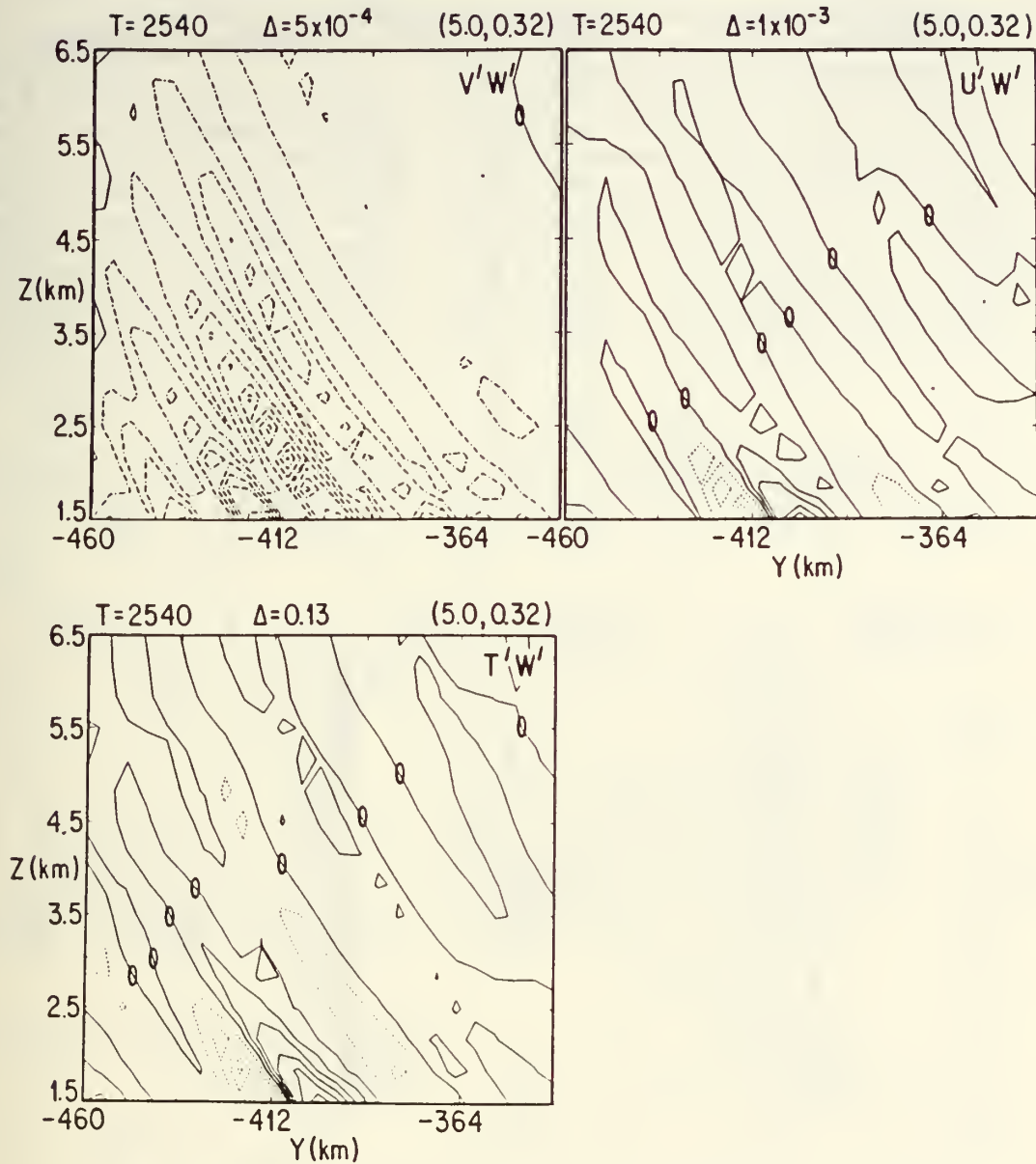


FIG. 7. Correlation fields of $v'w'$, $u'w'$ and $T'w'$ at time $T = 2540$ min for the stationary waves over the front. The perturbations were computed by subtracting the linear trend between the horizontal limits of the figures at the same level. Dotted (or dash-dot) lines are negative values, and zero lines are shown. The Δ denotes the contour interval ($\text{m}^2 \text{s}^{-2}$ for the upper figure and $\text{K m}^{-1} \text{s}^{-1}$ for the lower figure). Parentheses show resolution of the model as in Fig. 2.

We hypothesize that the increasing circulation features below the front are standing waves forced by the ageostrophic motions in the frontal zone and contained between the lower boundary, which is a reflection surface, and the frontal surface, which should act as a critical level, since there is a flow reversal across the frontal surface. Note that *stationary* waves below the front are possible, since the total flow in that region is from the cold air toward the frontal surface (Fig. 4). Thus a class of waves with phase propagation toward the cold air can be stationary. The vertical wavelength

of those waves is given by Eq. (4) and is shown in Fig. 5. Note that this wavelength does vary with height in the region, but is nearly independent of y . Furthermore, the wavelength of the stationary wave is zero near the center of the frontal zone (since the across-front velocity is zero there). Thus the refractive index of the waves, which is proportional to the inverse of this wavelength, is infinite, suggesting that the frontal surface is indeed a reflector for the stationary waves. In fact, it has been shown in Lindzen and Tung (1976) that, for waves whose Doppler-shifted phase velocity is zero, the re-

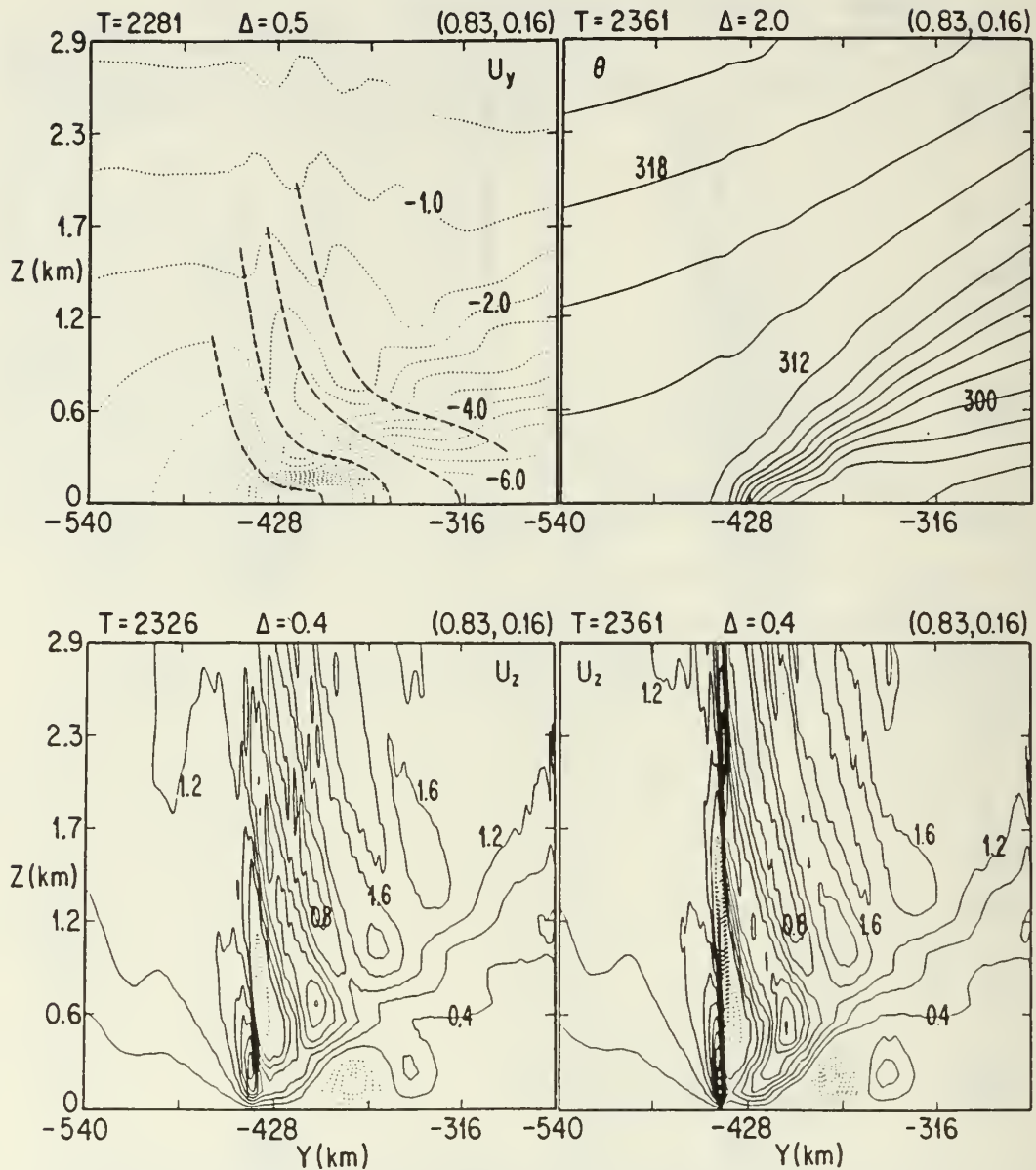


FIG. 8. Cross sections of the ageostrophic across-front flow, θ and w . Δ is the contour interval, m s^{-1} for v' , cm s^{-1} for w , and K for θ . Otherwise same as Fig. 2.

flectivity of a stable layer is one. Furthermore, the space between the two reflecting surfaces is small; thus, the group velocity of the stationary waves (about 10 cm s^{-1}) in this region is sufficient to allow several reflections in the course of a few hours. Thus the presence of stationary standing waves is possible.

Clark and Peltier (1984) have shown how waves forced upon a critical level can, under certain conditions, result in considerable wave motion amplification. In their calculations, the resonating cavity had one open node and one closed node, resulting in maximum am-

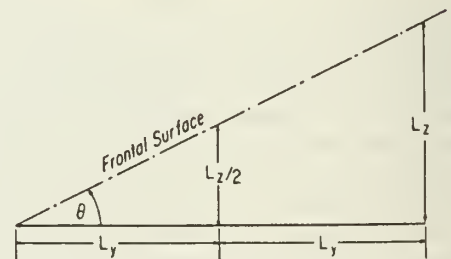


FIG. 9. Schematic showing the locations of the standing waves under the front.

tude at $\frac{1}{2}L_z$, $1\frac{1}{2}L_z$, etc. In our case, we have two
used nodes and should expect amplification at $L_z/2$,
etc., in a similar fashion.

A standing wave will form wherever the distance
between the frontal surface and the ground is an integer
multiple of $L_z/2$. Of course, L_z is the vertical wave-
length of the stationary wave as shown in Fig. 5. Since
front is sloped, and since L_z is roughly constant
with y , these waves should be nearly equally spaced a
distance L_y . This is illustrated schematically in Fig. 9.
For $L_z = 0.75$ km (an average value under the front
in Fig. 5), L_y will be about 50 km for the frontal slope
of 1/140 in these experiments. This is just about the

separation between the nose of the front and the center
of the circulation shown in the lower-left panel of Fig.
8. Also, it is just about the separation between the other
adjacent waves under the front shown in Fig. 3.

As before, we can demonstrate that the waves under
the front are consistent with standing gravity waves by
examining the various fluxes. Figure 10 shows $v'w'$,
 $u'w'$ and $T'w'$ computed in the same way that these
quantities were computed in Fig. 7. For a standing
wave, there can be no net vertical flux of momentum
by $v'w'$. In Fig. 10, this is clearly the case below 0.5
km, the height to which the waves illustrated in Fig. 8
appear to extend. Note that there are approximately

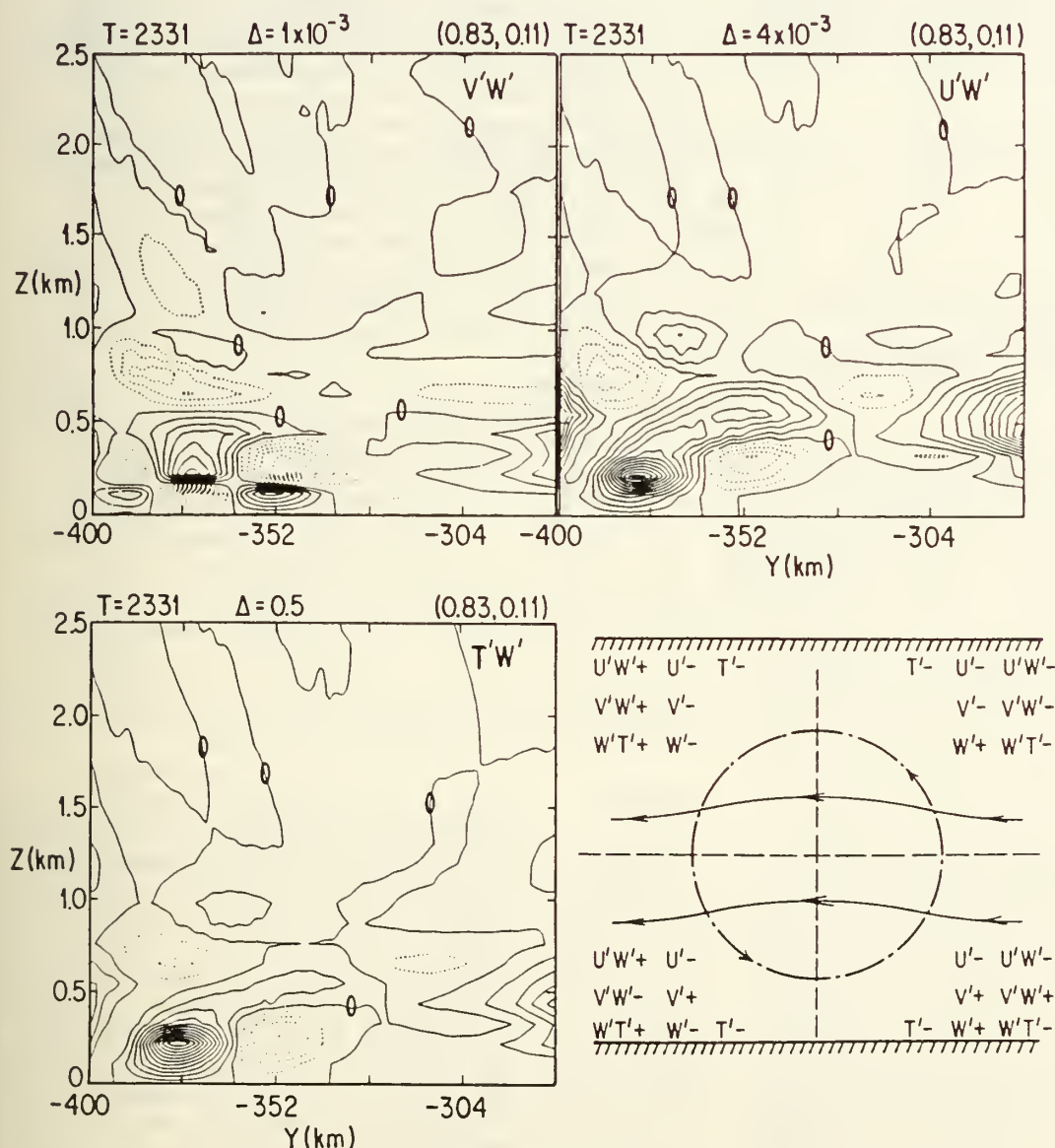


FIG. 10. As in Fig. 7, but for the stationary waves under the front. Schematic illustrates the fluxes expected in the various quadrants of the standing wave.

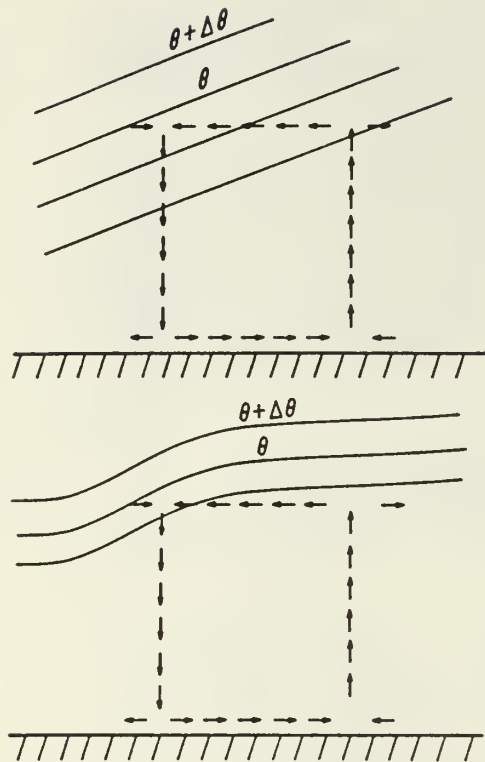


FIG. 11. Schematic showing the effect of the standing waves on the frontal surface.

equal regions of positive and negative values; thus the horizontal integrals of these quantities are zero, and so there are no mean fluxes of across-front momentum produced by the wave. This is also true of heat and along-front momentum, as it should be in these standing gravity waves.

The schematic in the lower-left corner of Fig. 10 is intended to show that the patterns of the three fluxes shown are consistent with the standing wave. The dash-dot line is the perturbation streamfunction for a standing wave (the phase lines are vertical), and the thin solid lines are total streamfunction (or isentropes for adiabatic flow). The perturbation quantities in each quadrant are shown along with the implied fluxes. Compare this diagram with the computed fluxes.

The motions produced by the standing waves change the slope of the frontal surface somewhat. Without these waves, the isentropes would slant uniformly upward to the right, as shown in the upper panel of Fig. 11. The motions produced in the standing wave, however, imply a perturbation circulation shown schematically by the arrows. These motions will tend to steepen the isentropes over the area of descent, due to the convergence above the downdraft, and decrease their slope over the region of ascent, where there is divergence. This is illustrated in the lower part of Fig. 11. Thus the frontal slope will become corrugated by

this process on a scale equivalent to that of the standing waves: about 50 km in our simulations. Note the evidence of these corrugations in the potential temperature, shown in Fig. 8, upper-right panel. This now produces a new horizontal scale to the motions in the frontal surface, in particular those responsible for the generation of the gravity waves, including those above the front. Thus we believe it is this scale that is produced by the standing waves which determines the horizontal scale of the waves above the front.

Although we have explained many of the features of the waves in our simulations, there is still more that needs to be examined. The effect of the standing waves on the distribution of potential temperature is actually forcing small-scale frontogenesis at the base of the frontal surface, as illustrated in our schematic (Fig. 11, lower panel). Note that a similar process does not happen at the ground under the updraft because the large-scale frontogenesis process has swept the temperature gradient away from the area where the standing wave develops. The steepening of the isentropes above the downdraft implies a narrowing and corresponding increase in the strength of the downdrafts, while the updraft widens and diminishes in intensity, since the isentropes steepen in the downdraft and flatten out over the updraft. We might regard this process as simply wave breaking.

Figure 12 shows the same region as in Fig. 8 but at later times. Note the continual increase in the downdraft and its narrowing. In these figures, the updraft actually appears to be absent, with the contour interval used, although it is still there. In addition, the steepness of the isentropes over the downdraft is even clearer. By the last panel of Fig. 12, a second standing wave nearer the nose of the front is beginning to appear. This wave began to form after the higher resolution of the inner nested model was introduced and is consistent with the small values of L_z at the "nose" of the front. It is probable that, had the resolution been sufficient, this wave would have begun to develop earlier.

At $T = 2441$, the nonhydrostatic, nongeostrophic motions in the standing wave have begun to produce their own wave fields above the strong downdraft. Again these are simply stationary waves forming above the source, but now the horizontal scale is determined by the scale of downdraft of the breaking wave. In this case, the horizontal scale is about 5 km.

The experiments were continued, but at higher resolution, with a third model nested inside the second. These results are illustrated in Fig. 13. The resolutions now are 35 m in the vertical and 280 m in the horizontal. Note that waves developing above the breaking wave continue and that the standing wave near $y' = -400$ is also beginning to break and set up waves above it. Note also that the wave right at the nose, which we discussed earlier, has begun to decrease. It is this decrease, as well as the sudden onset at the time

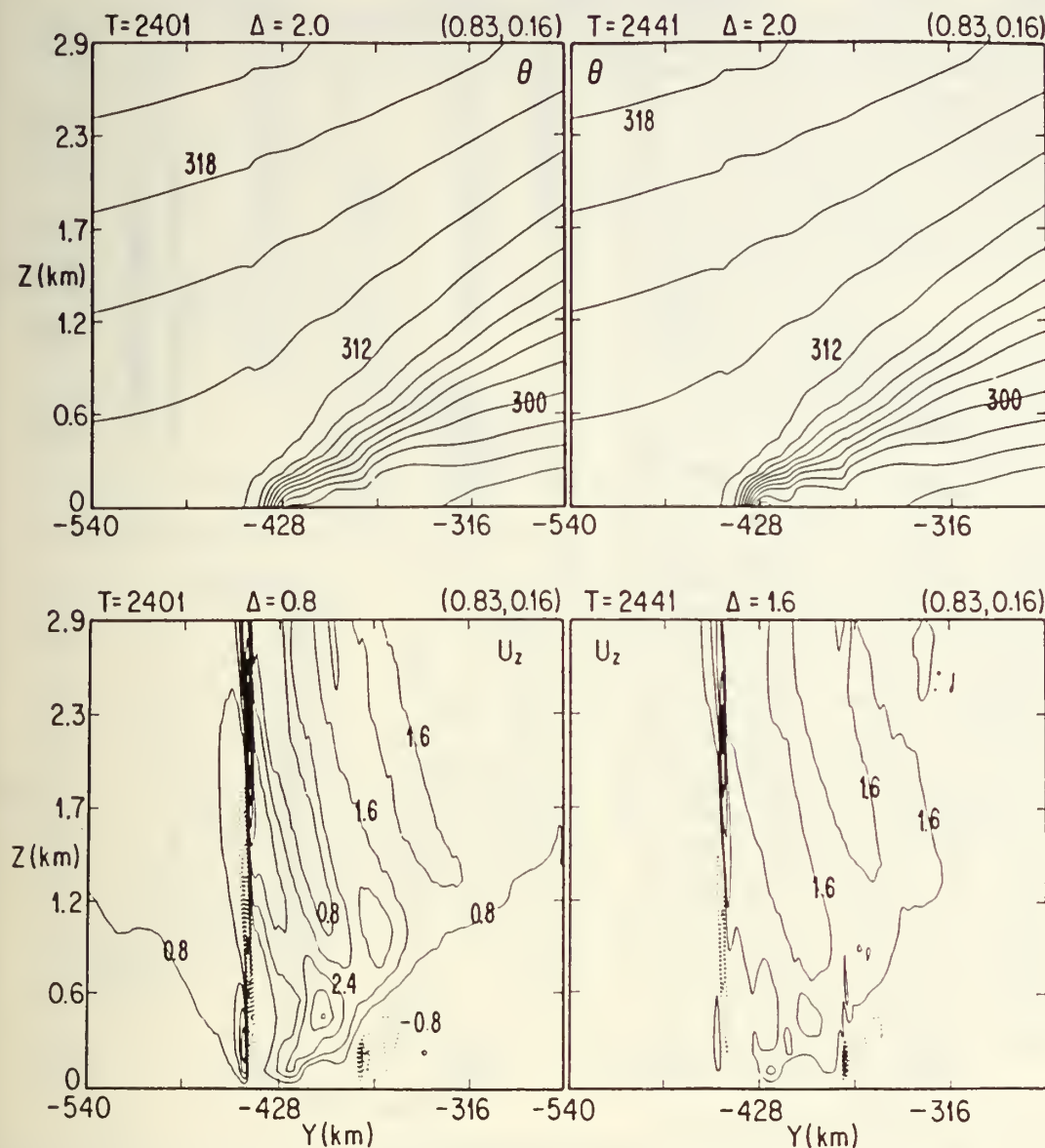


FIG. 12. As in Fig. 8, but for later times—and the upper right-hand panel shows θ .

increased resolution, that suggests to us that this was mostly a result of increasing the resolution. As the breaking of the standing waves continues in a high-resolution model, there is a strong production of rather small-scale waves that eventually appear throughout the zone underneath the front and, in fact, above the front as well. These waves are illustrated in Fig. 14. The band of no apparent wave activity in the vertical motion plot is simply due to the high static stability in the frontal zone, which suppresses the vertical motion. The waves themselves extend completely through this region, as is evident in the potential temperature field shown below (i.e., the stable region acts as a node for the dominant forced normal modes).

6. Conclusions

We have discussed the waves generated by a collapsing front in a numerical simulation. Some aspects of this particular simulation were addressed in a companion paper (Gall et al. 1987). In this paper, we have noted that there appear to be at least three classes of waves visible in the simulation.

With respect to the surface front, these included stationary waves over the front, standing waves underneath the frontal surface, and waves ahead of the front in the warm air that may or may not be moving. In this paper, the waves appearing both directly above and below the front are discussed.

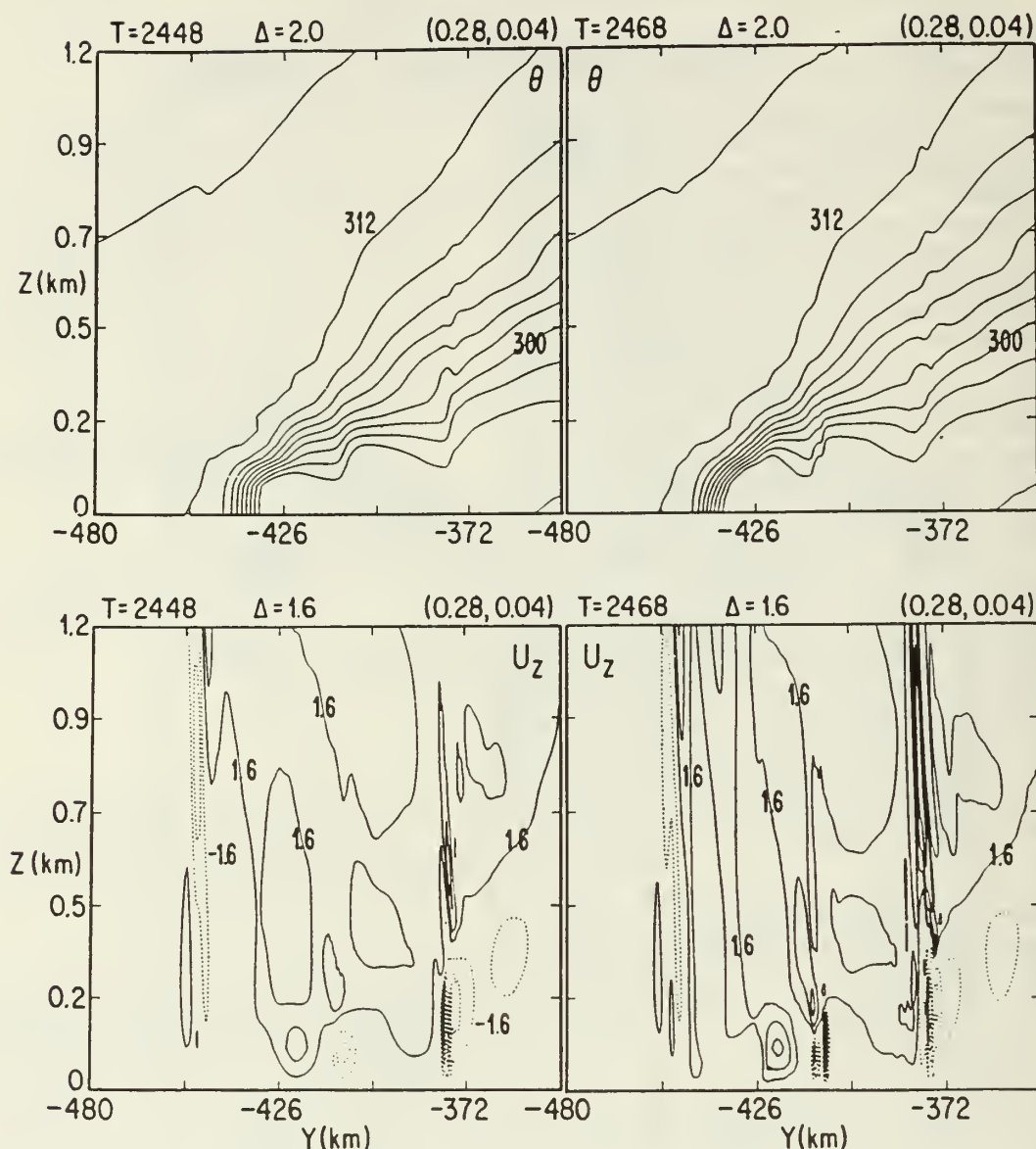


FIG. 13. As in Fig. 12, but for the very high resolution model.

Those appearing above the front are equivalent dynamically to the stationary wave that appears over mountains that are large enough for the flow in the waves to be hydrostatic. The waves are generated by nonhydrostatic and nongeostrophic accelerations in the frontal zone. Their vertical wavelength is consistent with horizontally stationary hydrostatic waves in this region. The horizontal scale of these waves appears to be selected by waves forming underneath the front. The waves above the front remain vertically propagating throughout the experiment, although the development of standing waves in this region would most likely occur after sufficient time for the group to prop-

agate the depth of the domain several times. For waves with a vertical wavelength of 2 km (vertical phase speed $\sim 0.1 \text{ m s}^{-1}$), this would take a couple of days.

The stationary waves under the front form standing waves in a couple of hours, since the separation between the frontal surface (which we postulate is a reflecting surface as well as the source of the waves) and the ground is less than 1 km. Since these waves are standing waves, they can occur only where the depth of the front is an integer multiple of $L_z/2$. This and the slope of the frontal surface specify the horizontal wavelength of the waves in this region. We further suggest that the standing waves, by forcing undulations in the frontal

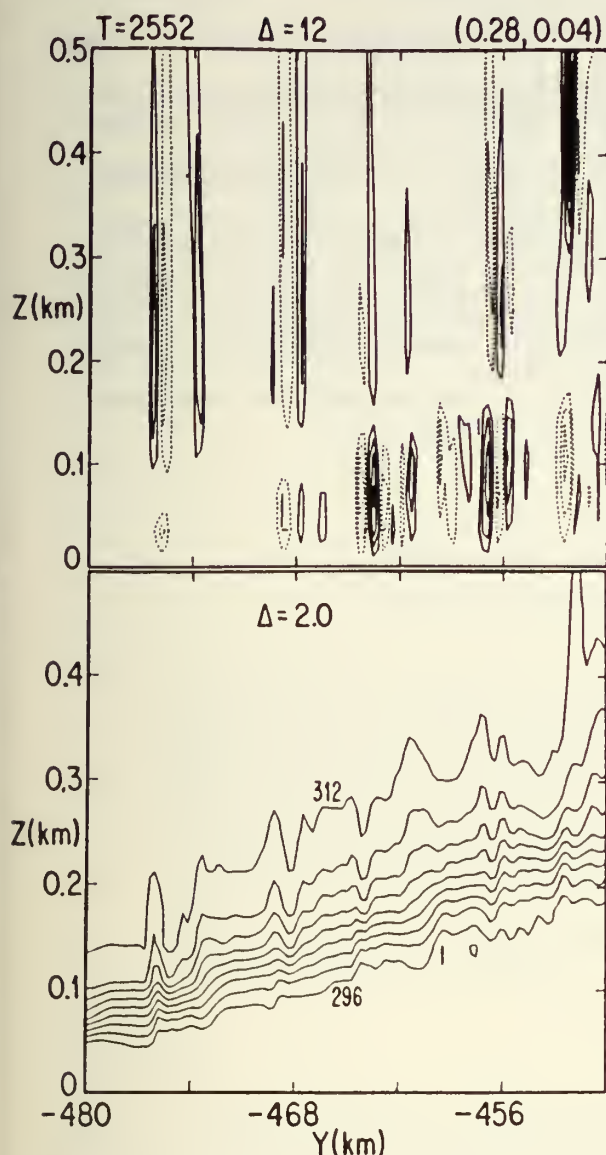


FIG. 14. Vertical velocity w (cm s^{-1}) upper figure and θ (K) lower figure in a small region of the front in the high resolution model. Otherwise as in Fig. 2.

surface, provide the horizontal scale for the waves above the front.

The standing waves under the front are shown to undergo a breaking process and, in doing so, to send up a new set of horizontally stationary waves above the region where the waves are breaking. In addition, as the wave-breaking process continues, strong, short-wavelength, traveling gravity waves are produced in the frontal region.

One could argue that the large along-front shears that develop in the frontal zone may, in some way, prevent the development of the waves described here

if the flow were permitted to be three-dimensional. We submit that, on the contrary, this instability may in fact increase the generation of gravity waves. Since shear waves will appear only where the Richardson number is small, these waves when they appear will be only in a narrow region along the frontal zone, not over a very deep region, such as the waves shown in Fig. 2. Furthermore, as the unstable shear waves develop, they will help to destroy geostrophic or hydrostatic balances in the frontal zone, and this in turn should increase gravity wave production.

We suggest that the stationary waves above the front, as well as the standing waves and the waves produced by the breaking of these standing waves below the front, may account for at least some of the banding noted in satellite pictures of fronts. The waves described here are forced to be two-dimensional, but since the processes we described are in reality essentially two-dimensional, then long linear lines of gravity waves are suggested. Gravity waves should always be produced during frontogenesis, and in many cases the stationary and standing waves we described here should be present. Furthermore, those waves will be produced regardless of whether or not precipitation is occurring. Thus waves such as those described here could account for banding in those portions of the front where there is little precipitation. Those waves should also be produced in those portions of the front where precipitation is occurring, and one could speculate on the role of these waves in effecting precipitation patterns.

Finally, early in the paper we mentioned an additional set of waves that appear in the warm air ahead of the surface front. These waves will be the topic of another paper. Here we just note that they too might contribute to banding in the clouds ahead of the front. Taken together, these sets of waves could produce a complex zone of banded clouds ahead of and in the immediate vicinity of the front.

Acknowledgments. Most of the research reported here was performed while one of the authors, Robert Gall, held the NAVAIR George Haltiner Research Chair in Meteorology at The Naval Postgraduate School in Monterey, California. Additional support was provided by NSF Grant ATM-8405276 at the Naval Postgraduate School and NSF Grants ATM-8407714 and ATM-8613514 at The University of Arizona. Computer calculations were performed at the National Center for Atmospheric Research. The final manuscript was edited by Margaret Sanderson Rae.

REFERENCES

- Bennetts, D. A., and R. J. Hoskins, 1979: Conditional symmetric instability—A possible explanation for frontal rainbands. *Quart. J. Roy. Meteor. Soc.*, **105**, 945–962.
- Clark, T., 1977: A small-scale dynamic model using a terrain-following coordinate system. *J. Comput. Phys.*, **24**, 186–215.

- , and W. R. Farley, 1984: Severe downslope windstorm calculations in two and three spatial dimensions using an elastic interactive grid nesting: A possible mechanism for gustiness. *J. Atmos. Sci.*, **41**, 329–350.
- , and W. R. Peltier, 1984: Critical level reflection and resonant growth of non-linear mountain waves. *J. Atmos. Sci.*, **41**, 3122–3134.
- Emanuel, K. A., 1983a: The Lagrangian parcel dynamics of most symmetric instability. *J. Atmos. Sci.*, **40**, 2368–2376.
- , 1983b: On assessing weak conditional symmetric instability from atmospheric soundings. *Mon. Wea. Rev.*, **111**, 2016–2033.
- Gall, R., R. T. Williams and T. Clark, 1987: On the minimum scale of fronts. *J. Atmos. Sci.*, **44**, 2562–2574.
- Hoskins, R. J., 1974: The role of potential vorticity in symmetric stability and instability. *Quart. J. Roy. Meteor. Soc.*, **100**, 480–482.
- , and F. Bretherton, 1972: Atmospheric frontogenesis models: Mathematical formulation and solution. *J. Atmos. Sci.*, **29**, 11–37.
- Houze, R., and P. Hobbs, 1982: Organization and structure of precipitating cloud systems. *Advances in Geophysics*, Academic Press, 225–305.
- Ley, B., and W. R. Peltier, 1978: Wave generation and frontal collapse. *J. Atmos. Sci.*, **35**, 3–17.
- Lindzen, R. S., and K.-K. Tung, 1976: Banded convective activity and ducted gravity waves. *Mon. Wea. Rev.*, **104**, 1602–1617.
- Smolarkiewicz, P., 1983: A simple positive definite advection scheme with small implicit diffusion. *Mon. Wea. Rev.*, **111**, 479–486.
- , 1984: A fully multidimensional positive definite advection transport algorithm with small implicit diffusion. *J. Comput. Phys.*, **54**, 325–362.
- Williams, R. T., 1972: Quasi-geostrophic versus non-geostrophic frontogenesis. *J. Atmos. Sci.*, **29**, 3–10.

On the Minimum Scale of Surface Fronts

R. L. GALL

Institute of Atmospheric Physics, The University of Arizona, Tucson, AZ 85721

R. T. WILLIAMS

Dept. of Meteorology, Naval Postgraduate School, Monterey, CA 93940

T. L. CLARK

National Center for Atmospheric Research, Boulder, CO 80307*

(Manuscript received 30 July 1986, in final form 12 March 1987)

ABSTRACT

A series of numerical experiments of a surface front forced by stretching deformation using Clark's nonhydrostatic model at very high resolution is presented. These simulations are compared to those reported by Williams who used hydrostatic models at lower resolution. The main purpose was to determine whether this front would collapse (in the absence of friction) to a scale similar to that reported by Shapiro et al. (most of the temperature gradient contained in 200 m). The question is whether there is a natural physical process in the frontal dynamics which limits the frontal collapse in the absence of diffusion processes.

For this front we could not find a natural limiting process, although the mechanism discussed by Orlanski et al. appears to be operating. The minimum scale is determined by the vertical resolution. At the vertical and horizontal resolutions we tried, the vertical resolution determined the scale because the slope of the front is so shallow.

Some of the structure found by Cullen and Purser by extending the semigeostrophic models beyond the initial development of a discontinuity is apparent in our solutions.

1. Introduction

There is a rapidly accumulating body of evidence which suggests that the horizontal scale of many fronts can be very narrow. For example, Shapiro et al. (1985) have recently reported on the passage of a front over the instrumented tower near Boulder, Colorado, where most of the temperature gradient passed the tower in about ten seconds. Using the motion of the front across the surface network surrounding the tower, an upper bound on the horizontal scale of the front can be inferred to be about 200 m. Studies by Carbone (1982) using Doppler radar data further support the notion that the horizontal scale of many fronts can be very narrow. Carbone's case, however, included condensation, while the cases treated by Shapiro were dry. One need not resort to very sophisticated techniques to demonstrate that frontal scales are often quite narrow (Shapiro et al., 1985). Weather forecasters for years have noted that even very simple thermographs show temperature falls of 10°C or more in, say, ten-minute periods during strong cold-front passages. Assuming

that the front is traveling at 20 m s⁻¹ (probably a high estimate), then most of the temperature gradient is confined to a zone that is *at most* 15 km wide. While this is considerably larger than the scale reported by Shapiro et al., it is still much narrower than resolvable in standard observing networks.

If we are willing to accept that frontal scales can be this size, or smaller, then there are a number of outstanding theoretical problems. It is true that even the simplest theoretical models, such as those derived from the semigeostrophic equations (Hoskins, 1971; Hoskins and Bretherton, 1972), can predict that infinite horizontal temperature gradients will develop in finite time at the earth's surface (and other boundaries, such as an upper boundary if it exists in the model). However, one can easily argue that diffusion processes such as those always operating in the atmosphere, or those produced by any shear instability that must certainly develop as the gradients within the front become large, will eventually prevent the collapse of the front into a discontinuity. Williams (1974) has shown that, in a numerical model with constant diffusion coefficients, the frontogenesis process will stop at relatively large (as compared to the results of Shapiro et al.) horizontal scale. The horizontal diffusion coefficients used in that model were rather arbitrary, although they are thought

* The National Center for Atmospheric Research is sponsored by the National Science Foundation.

to be reasonable. The vertical coefficients, on the other hand, were reasonable for the planetary boundary layer. This being so, then either the diffusion processes in the front observed by Shapiro et al. are quite weak or very strong frontogenetical forcing not present in the semi-geostrophic equations must switch on as the scale of the front decreases.

Recently Orlanski et al. (1985) have argued that as the frontal scale becomes very narrow, more fundamental mechanisms within the front, other than friction, may begin to operate to limit further collapse of the front. They argue that when the gradients in the front become very large, nongeostrophic accelerations may lead to a reduction of the generation of vorticity at the front. Since a continued increase in vorticity is necessary for the front to go to a discontinuity, this will effectively limit the strength of the front. It is not clear what minimum scale is implied by their arguments, although some of their numerical results suggest that the minimum scale could still be fairly broad.

The above arguments do not exhaust the list of possible mechanisms that may limit the minimum scale of a front. When the frontal gradients become quite large, other relatively small-scale flows may develop that are not accounted for in the quasi- or semi-geostrophic theories. In some fronts, especially those producing considerable precipitation, a symmetric instability may develop (see Bennets and Hoskins, 1979; Emanuel, 1983a,b), and fluxes of momentum and heat produced by these waves could affect frontal development. The same could be said of gravity waves generated during frontal collapse (Ley and Peltier, 1978).

The purpose of the work reported here is to explore, for one type of front, the mechanisms, if any, that will limit the final strength of the front in the absence of diffusion. We will also look for mechanisms that may develop to enhance the frontogenesis. In particular, we will be considering the front forced by pure stretching deformation, considered by Williams (1972, 1974) and Hoskins and Bretherton (1972). This type of front is probably most similar to the one studied by Shapiro et al. (1985; note the temperature gradient along their front was near zero) and is probably the simplest front. In this study, the forcing (the deformation field) is invariant with time. If the deformation were to vary with time, it could, of course, provide a means for limiting the scale of the front.

Since we are interested in studying the front when the scale becomes very small, the possibility of non-hydrostatic effects becoming important exists. Thus, we will study the frontogenesis using a nonhydrostatic numerical model. We will be using the model described by Clark (1977). That model has the ability to handle up to three levels of nesting; thus, it can model the large-scale flows forcing the overall frontogenesis as well as small-scale flows in the immediate vicinity of the front. Using three levels of nesting, we are able to achieve a high-resolution simulation near the front with

a vertical resolution of 35 meters and a horizontal resolution of 280 meters.

Recent work by Cullen and Purser (1984) suggests that if we relax the conservation requirements in a very limited region near the front, the semi-geostrophic conservation laws (momentum and potential temperature) can be applied beyond the initial development of a discontinuity at the surface. This formulation allows the discontinuity to extend into fluid away from the boundary. The distance which the discontinuity extends into the flow can be calculated. Thus, we will use results from our model to determine whether these predictions are reasonable.

Finally, some studies have suggested that the minus three power law that describes the spectral distributions of kinetic energy at wavenumbers above the cyclone scale is a result of the existence of fronts. For example, Andrews and Hoskins (1978) showed that the semi-geostrophic solutions would imply a $-8/3$ spectrum just at the time infinite vorticity first develops. By following the development of baroclinic waves in a GCM, Gall et al. (1979) found a tendency for the -3 spectrum to be a function of the extent to which the baroclinic waves developed. If the development of the waves stopped before the surface fronts reached the maximum intensity permitted by resolution in the model, then the spectrum of kinetic energy was much steeper than -3 . This is as it should be if the energy spectrum is determined by fronts.

Williams (1967), in a numerical study of frontogenesis forced by shearing deformation, found that the spectrum may become even more shallow than the $-8/3$ slope predicted by Andrews and Hoskins. Andrews and Hoskins' result applies only at the moment the vorticity goes to infinity at a point on the surface. If the frontogenesis could proceed beyond this point, perhaps in the manner described by Cullen and Purser, the spectrum could be more shallow. For example, if the distribution of variables near the front approaches a sawtooth distribution, the slope of the spectrum would be -2 .

In addition to exploring the mechanisms that determine the minimum scale of the front, we will also comment on the development of the kinetic energy spectrum produced by the frontogenesis in a model where very fine resolution is used to define the front.

2. The model

a. Equations

The model used in these experiments is described in detail in other publications (Clark, 1977; Clark and Farley, 1984). We will only briefly outline the model here.

The model is nonhydrostatic and anelastic; the basic equations are

$$\rho_0 \frac{du}{dt} - \rho_0 v f = -\frac{\partial P'}{\partial x} \quad (1)$$

$$\rho_0 \frac{dv}{dt} + \rho_0 u f = -\frac{\partial P'}{\partial y} \quad (2)$$

$$\rho_0 \frac{dw}{dt} = -\frac{\partial P'}{\partial z} - \rho' g \quad (3)$$

$$\rho_0 \frac{d\theta}{dt} = 0 \quad (4)$$

$$\frac{\partial \rho_0 u}{\partial x} + \frac{\partial \rho_0 v}{\partial y} + \frac{\partial \rho_0 w}{\partial z} = 0, \quad (5)$$

where ρ_0 is the background density that is a function of z ; u , v and w are components of the velocity vector in the usual notation; and P' and ρ' are deviations from their background values. Our simulations will neglect diffusion, and the terms usually included in (1)–(4) to account for its effects are zero. In our simulations, we will assume two-dimensional flow. Variation of perturbation quantities along the front (in the x -direction) is neglected.

Because the model is nonhydrostatic, pressure is solved by combining (1)–(3) into a divergence equation and setting

$$\frac{d}{dt} \left(\frac{\partial \rho_0 u}{\partial x} + \frac{\partial \rho_0 v}{\partial y} + \frac{\partial \rho_0 w}{\partial z} \right) = 0 \quad (6)$$

in accord with (5). An elliptic equation results, which can then be solved for P' .

b. Finite difference approximations

The difference approximations to (1)–(6) are discussed extensively in Clark (1977). All spatial differences in the momentum and pressure equations are centered, as are the time differences for most of the calculations. Periodically the calculations are restarted using a Euler backward step to prevent time splitting.

The thermodynamic equation is approximated by a scheme discussed at length in Smolarkiewicz (1983, 1984). In essence, this scheme uses an upstream spatial difference and a forward difference in time, followed by at least one additional step to correct the strong diffusion characteristic of the upstream difference scheme. A single correction step was employed in the present calculation. Smolarkiewicz has shown that this difference scheme is second order in time and space. The scheme has many advantages in regions where there are very large gradients, as will occur in the frontal problems presented here. It also has the advantage, unlike centered difference schemes, that positive definite fields will stay positive definite.

The numerical model has the option of including some smoothing within a few grid intervals of the horizontal boundaries to reduce reflections. This option is used in our simulations. Since our frontal models

are more or less symmetric about the half level [they will not be truly symmetric, as in the simulations by Williams (1972), because of the anelastic approximation], we expect fronts on both the upper and lower boundaries. Although there is no analogue for a rigid boundary at 9 km in the atmosphere, one is used here and must be considered part of the problem under consideration. Hence any reflections of wave energy off the upper and lower boundaries must also be considered part of the problem. We do not attempt to reduce the amplitude of the wave energy as it approaches the upper boundary, using the filters available in the model, as described by Clark (1977). Except for some implicit smoothing inherent in the difference schemes and the smoothing near the horizontal boundaries, the model runs here are truly inviscid.

c. Nesting

In order to achieve as high a resolution as possible, a nesting procedure is used that allows higher resolution models inside coarse models. This nesting procedure is described by Clark and Farley (1984). It is two-way, in that the coarse mesh supplies boundary conditions to the fine mesh, and the fine-mesh solutions are then used to update the coarse mesh.

The position of an inner nested model is arbitrary; the boundaries of the inner model need not coincide with any boundary of the outer model (including upper and lower boundaries). Inner models must, though, be totally contained within the outer model with which they interact. The ratios of the coarse- to fine-grid intervals must be integers, and the time step must be the same for all nested models.

d. Initial conditions

The primary motivation for this research is to examine whether scales similar to those observed by Shapiro et al. (1985) can develop in a very simple frontal model. We assume that there is very little temperature gradient along the front, so that the forcing of the front must be primarily by stretching deformation rather than by shearing deformation (Hoskins and Bretherton, 1972; Williams, 1967). We will use the very simple model of a front where the stretching deformation is constant, there is no variation along the front, the static stability is initially constant over the domain, and the horizontal temperature gradient is initially vertically constant. This type of frontogenesis has been considered by a number of authors (e.g., Williams, 1972; Williams and Plotkin, 1968; Hoskins and Bretherton, 1972). For our simulations, we will use the same initial conditions as Williams (1972):

$$\theta(y, z, 0) = \frac{\partial \bar{\theta}_1}{\partial z} (z - H/2) - a(2/\pi) \arctan(\sinh \alpha y) \quad (8)$$

where

$$\alpha = f\pi H^{-1} (g\theta_0^{-1} \partial \bar{\theta}_1 / \partial z)^{-1/2}$$

and where we use

$$f = 10^{-4} \text{ s}^{-1}$$

$$H = 9 \text{ km}$$

$$\partial\theta_1/\partial z = 4 \text{ K km}^{-1}.$$

The component of the flow parallel to the front, $u(y, z, 0)$, is computed from a finite difference version of the thermal wind equation using the same differencing as used in the model itself and with

$$u(y, 0, 0) = -\frac{2}{\pi} \frac{ga\alpha H}{f\theta_0 z} \text{sech}(\alpha y) \quad (9)$$

where $g\theta_0^{-1} = 0.0327 \text{ m s}^{-2} (\text{K})^{-1}$ is used. These conditions will provide an initial state similar, but not identical, to those presented by Williams. The vertically variable density of the base state (ρ_0) allowed in the anelastic model means the flow in our model will not be symmetric about the half level, as in Williams' model.

In addition to the above flow, the streamfunction of the deformation flow given by

$$\psi_d = -Dxy \quad (10)$$

is included and assumed constant in time. It is, of course, this flow that forces the frontogenesis. The deformation flow is added to the model equations simply by adding terms to the governing equations involving the deformation velocities as defined by (10). These terms are, of course, independent of time. As in Williams (1972), we choose $D = 10^{-5} \text{ s}^{-1}$.

Finally in order to prevent production of large amplitude gravity waves early in the experiment, the initial ageostrophic flow in the vertical plane parallel to the temperature gradient is computed from

$$\frac{g}{\theta_0 f^2} \frac{\partial \bar{\theta}_1}{\partial z} \frac{\partial^2 \psi}{\partial y^2} + \frac{\partial^2 \psi}{\partial z^2} - \frac{1}{\rho_0} \frac{\partial \rho_0}{\partial z} \frac{\partial \psi}{\partial z} = \frac{2Dg\rho_0}{\theta_0 f^2} \frac{\partial \theta}{\partial y}, \quad (11)$$

where ψ is the streamfunction of the ageostrophic flow. The development of this quasi-geostrophic circulation equation is similar to that found in Williams (1972), but here the effects of $\rho_0(z)$ are included. The initial v and w fields are calculated from

$$v = \frac{\partial \psi}{\partial z}, \quad w = -\frac{\partial \psi}{\partial y}, \quad (12)$$

after (11) is solved for ψ . Boundary conditions for (11) are $\psi = 0$ on all boundaries.

e. The experiments

In all the calculations reported here, the horizontal domain of the outer model is 3600 km. The calculations are accomplished by first integrating the equations on a grid with a horizontal resolution of 20 km and a vertical resolution of 320 m. This model, which runs

very fast, is integrated beyond the point where temperature gradient at the surface would first become infinite with the semigeostrophic equations. We will show later how this time is determined. After this initial integration, a second model, with a horizontal resolution of 10 km, was initialized at 1340 min using the flow from the 20 km model. This is followed by other model runs at higher resolution using the flow from models with lower resolution as initial conditions. Finally, two nesting experiments were performed. One used two domains, where the lower boundary of the nested domain lay on the surface in the region of the front. The other used three domains in a similar fashion, simply adding a third domain inside the previous second domain.

Figure 1 is a schematic that illustrates when various models were run and for how long. The solid bars show when the models are integrated relative to the time of the initial conditions specified by (8), (9), (10) and (12). Arrows show from which model the initial conditions of the higher resolution models are derived. At the right, Δy and Δz indicate, respectively, the horizontal and vertical resolutions of the model in kilometers.

The experiments shown in the top of the figure are single models that do not employ nesting. The lower bars show an experiment using two models nested one inside the other and one with three. Figure 2 illustrates where the nested models are located within the outer domains by showing actual results from the model with three levels of nesting. The results from the innermost model are shown in Fig. 5. In the case of the two-nested models, the inner model is the same as the first inner model in the experiment with three-nested models. In all experiments, the domain of the outer model is the same.

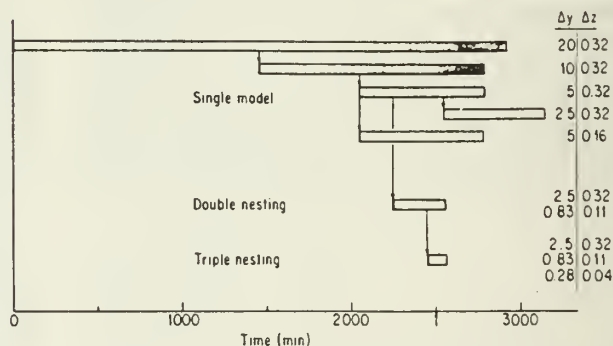


FIG. 1. Schematic indicating times when models of various resolutions were run. At $T = 0$, the flow is given by the initial conditions described in the text. Resolution used in a particular model is indicated on the right, and the model used as a source for the initial conditions of higher resolution models is given by the arrows. Single models had no interior nested models, while double and triple nesting had one and two interior models, respectively. The arrow at 2500 min indicates the time we expect a discontinuity would first form at the surface in a semigeostrophic model.

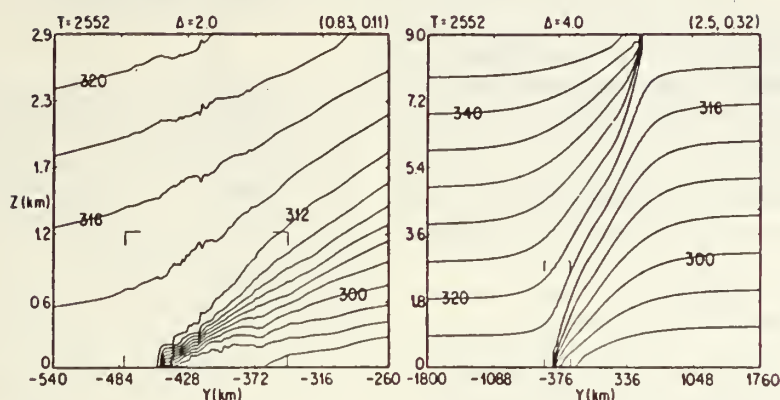


FIG. 2. Cross sections of potential temperature. T is the time (min) of the cross sections measured from the beginning of the experiments as in Fig. 1, Δ is the contour interval in $^{\circ}\text{K}$, and the number in parentheses gives the resolution of the model in km (Δy , Δz). These results are from the triply nested model where the tick marks indicate the location of the next inner model. Results from the innermost model are given in the lower right-hand panel of Fig. 5.

In this frontogenesis experiment, similar fronts form on both upper and lower boundaries. In the discussion that follows, we will concentrate on the front near the lower surface; thus the nested models are applied to that front only.

3. Results

a. Collapse of the front

For the stretching deformation forcing of frontogenesis, such as is considered here, the frontal evolution down to a scale of about 50 km is now well known. For example, numerical solutions to the problem considered here are described by Williams (1972). Analytic solutions for the semigeostrophic case are presented by Hoskins (1971). The stretching deformation flow forces a direct circulation in the plane parallel to the temperature gradient, and this circulation, in turn, forces the maximum temperature gradient to form on both upper and lower boundaries. At the lower surface, it forms on the warm-air side of the axis of dilation of the deformation flow; and on the upper boundary, it forms on the cold-air side. This vertical tilt in the frontal zone depends on the strength of the temperature gradient. The surface front forms at the point where the sum of the deformation velocity and the horizontal component of the direct circulation is zero.

Hoskins and Bretherton (1972) have shown that for the semigeostrophic approximation to the governing equations, the temperature gradient becomes infinite in a finite period of time at the boundaries. For the front considered here, these infinite gradients would first appear about 1.75 days after the initial conditions.

Orlanski et al. (1985), however, argue that if the semigeostrophic approximation is not made, there are dynamical processes (other than diffusion) that will limit the ultimate strength of the front, and infinite

temperature gradients will not be reached. They argue that the large convergence that is occurring in the frontal zone, thereby producing the large vorticity in this region, would in unbounded growth lead to an imbalance between ζf and $\nabla^2 P$ in the divergence equation. However, it is not clear which way this imbalance would go. During frontogenesis, the imbalance between the fields of mass and momentum can increase due to the acceleration of the velocity component across the front. The horizontal gradient, G_y , of this imbalance

$$G_y = \frac{\partial}{\partial y} \left(-fu - \frac{1}{\rho_0} \frac{\partial P'}{\partial y} \right), \quad (13)$$

if it is nonzero, can lead to a reduction in convergence in the frontal zone and concurrent reduction in the stretching production of vorticity. In any event, a non-zero value implies a tendency of divergence. In the semigeostrophic equations, ζf and $\nabla^2 P$ always balance one another, and it can be shown that unbounded growth of the vorticity in frontal regions is inevitable with proper forcing. Thus the presence of a geostrophic imbalance in the frontal regions could act as a process which limits the frontogenesis, contrary to the predictions of semigeostrophic theory. This is an important point for, as Orlanski et al. (1985) point out, some fronts do exist for some time. They must be in a state of quasi-balance, and it seems unlikely that diffusion can be responsible if the fronts are fairly broad, since then diffusive processes might be relatively weak as compared to processes that are forcing the front. On the other hand, the results of Shapiro et al. (1985) imply that some fronts can be extremely sharp, which intimates that the limiting processes suggested by Orlanski et al. are not operating.

Our solutions can demonstrate whether there are natural processes that limit the frontogenesis for the

type of front we are considering. Figure 3 shows the separation of two isentropes at the lower surface as a function of time for various experiments with different horizontal and vertical resolutions. These isentropes are separated by 19 K and include most of the temperature gradient across the front. For low horizontal and vertical resolution ($\Delta y = 2.5$ km and $\Delta z = 320$ m), the spacing decreases almost linearly until about 2300 min from the start of the experiment, after which time the rate of reduction of the separation diminishes and eventually goes to zero. In each of the experiments with a vertical resolution of 320 m, the final separation after long time periods is still 30 km, illustrating that for this vertical resolution, the final strength of the front is independent of the horizontal resolution, at least for those resolutions considered.

Increasing the vertical resolution by a factor of 2, however, results in a final separation of about 15 km; decreasing Δz by a factor of 3 from 320 m leads to a 10-km separation, and decreasing Δz again by a factor of 3 results in a final separation of about 3 km. Thus, while for a given vertical resolution the final strength of the front appears independent of the horizontal resolution, perhaps suggesting there is a mechanism limiting the frontogenesis, the results with higher vertical resolution suggest otherwise.

The reason why the vertical resolution affects the extent of the frontogenesis in these experiments rather than the horizontal resolution is because the frontal slope of 1/140 is almost horizontal, as are most atmospheric fronts. Thus, as the front collapses, it begins to "feel" the minimum vertical resolution while it is still well resolved in the horizontal. Once there is insufficient vertical resolution to resolve the front, the frontogenesis ceases. Figure 4 verifies that it is the vertical resolution that is determining the final scale of the front, since the minimum spacing between the isentropes is a linear function of the vertical grid spacing.

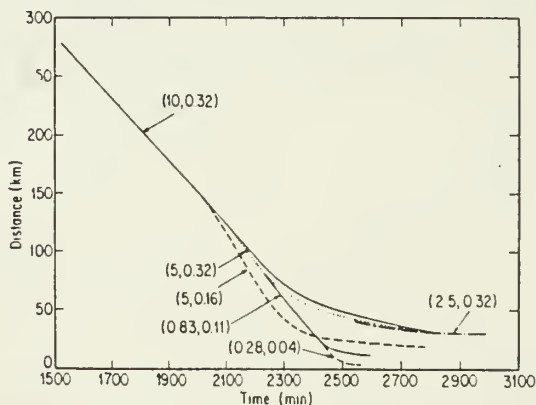


FIG. 3. Horizontal separation of two isentropes bounding most of the temperature gradient in the frontal region at the surface in the various models as a function of time. These isentropes differed by 19 K. Numbers in parentheses give the resolution in km (Δy , Δz). For nested models, the resolution of the innermost model is indicated.

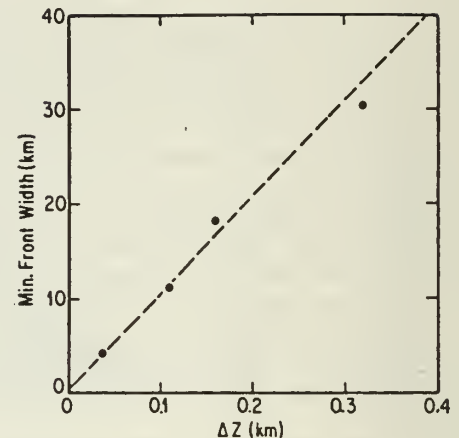


FIG. 4. Minimum frontal width from Fig. 3 as a function of vertical grid spacing.

Therefore, for the experiments illustrated here, we could find no natural limiting process for the frontogenesis, at least down to a point where most of the temperature gradient was contained in a zone only 3 km wide. We should emphasize here that this result neglects diffusion processes or surface drag and any instability that could result from variations along the front.

It is quite possible that the lack of surface stress is the physical reason the very sharp gradients observed by Shapiro et al. did not develop in our experiments. The front in these simulations lines up along the line where the total across-front velocity goes to zero. With zero surface stress, this line is very nearly horizontal. With the introduction of surface stress, where the across-front velocity is reduced to zero at the surface, the line of zero total across-front velocity would become very steep near the ground. This being the case, the frontal surface might become steep as well, and since the isentropes that make up the frontal surface tend to parallel it, at least for some distance, the isentropes near the ground may also become nearly vertical. The resulting convective overturning could then lead to the destruction of geostrophic balance within the frontal region, leading, in turn, to the development of a gravity current. This is only speculation and needs to be verified by future experiments that include surface stress.

Figure 3 can be used to identify when infinite temperature gradients across the front would first develop if the frontogenesis were to proceed as in the semigeostrophic models. In the semigeostrophic models, the frontal scale decreases linearly with time, and we note long periods in Fig. 3 with a linear decrease in scale. Extrapolating these linear trends to zero scale gives an estimate when the semigeostrophic equations would give infinite temperature gradients at the surface. From Fig. 3, this time is approximately 2500 min from the start of the experiment.

b. Frontal structure

Figure 5 illustrates the effect of increasing horizontal and vertical resolution on the structure of the front near the surface. In all cases, the maximum temperature gradient is greatest nearest the surface and decreases upward along isentropes that extend from the surface position of the front. Of course, in the middle of the domain (near 4.5 km) virtually no frontogenesis has occurred. These points are explained by classical frontogenesis theory (Hoskins and Bretherton, 1972). With increasing vertical resolution, there is a tendency for a ribbon of very high temperature gradient to extend upward from the surface and along the slope of the front. This feature is most obvious in the run with a vertical resolution of 35 m (lower right-hand panel). Note that while the horizontal temperature gradient is largest at the surface, it is not diminished by much until above about 400 m. Cullen and Purser (1984), by extending the semigeostrophic models beyond the point where a discontinuity first develops at the surface, suggested that the discontinuity may extend away from the surface toward the center of the fluid after the time of the initial discontinuity. This type of behavior is suggested by Fig. 5. The reader is encouraged to compare the high-resolution result shown in Fig. 5 with

Fig. 12 of Cullen and Purser (1984). In their figure, the heavy solid line denotes the line of (in their case) infinite temperature gradient. Above this line, the isentropes spread out, much as in our simulation.

We can obtain an estimate of just how far the discontinuity can extend into the fluid. Let the minimum value on a horizontal plane of

$$d = \left[\frac{\Delta\theta}{|\partial\theta/\partial y|} \right]_{\min} \quad (14)$$

be a measure of the width of the front. If this is transformed to geostrophic momentum coordinates (Eliassen, 1962; Hoskins and Bretherton, 1972) with

$$Y = y - u_g/f, \quad (15)$$

then semigeostrophic theory gives

$$d = \Delta\theta \left[\frac{1 + f^{-1} \partial u_g / \partial Y}{|\partial\theta/\partial y|} \right]_{\min}, \quad (16)$$

where $\Delta\theta$ is the overall potential temperature change across the front. In geostrophic momentum coordinates, the frontal evolution is governed by the quasi-geostrophic equations.

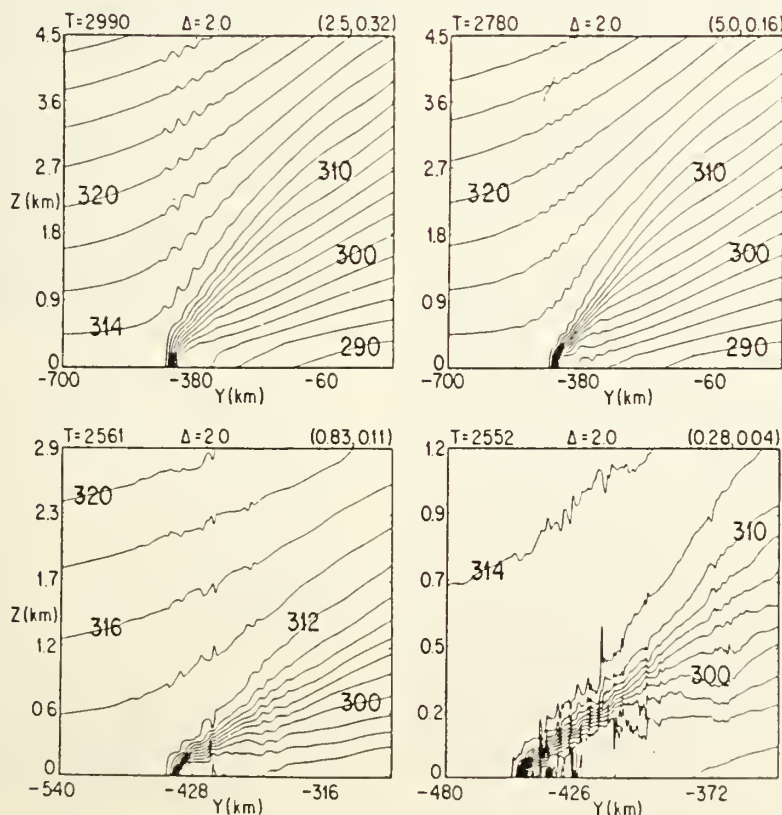


FIG. 5. As in Fig. 2 except for cross sections of potential temperature from the inner model of models of various resolution.

Our simulations were set up to be as close to those reported by Williams as possible. Analytical solutions to the quasi-geostrophic approximation to those simulations are given in Williams and Plotkin (1968) and can be used to estimate d from (16) for our problem. Inserting the solutions for θ and u at infinite time from Williams and Plotkin into (16) gives

$$d = \left[\frac{1 - \frac{gH\Delta\theta \sinh(\pi Y/L_R) \sin\pi\xi}{\theta_0 f^2 L_R^2 \sinh^2(\pi Y/L_R) \cos\pi\xi}}{\frac{2}{L_R} \frac{\cosh(\pi Y/L_R) \cos\pi\xi}{\cosh(2\pi Y/L_R) + \cos 2\pi\xi}} \right]_{\min} \quad (17)$$

where $\xi = (z - H/2)/H$, and H is the depth of our domain, 9 km. It is well known that d in (16) goes to zero at the surface in a finite period of time, and generally this point is accepted to be the time when semi-geostrophic theory ceases to be valid. Indeed, this is the point when infinite vorticity would first develop at the surface. If, however, we accept Cullen and Purser and allow the semi-geostrophic solutions to extend beyond the point where d first goes to zero, then negative values of d will occur wherever $\partial u_g / \partial Y$ exceeds f . Hence, a region of negative d [given by (16)] will be present at the boundary, reaching a minimum at the position of the front on the boundary. These negative values will extend upward to some height, above which d will be positive. If we take the horizontal plane where d just goes to zero, but is not negative, to give the highest level where a discontinuity would exist, then we can use (17) to give the height to which the strong front will extend after infinite time. Inserting the values used in our experiment: $g/\theta_0 = 0.033$, $H = 9000$ m, $L_R = 10^6$ m, $f = 10^{-4}$ s $^{-1}$, then this level would be at 1 km above the surface.

In Fig. 5, in the model with the highest vertical and horizontal resolution, the band of maximum temperature gradient extends up to about 400 m. However, because of the cost of this experiment, integration was terminated after only an hour beyond our projected time of a discontinuity first forming at the surface. Since the above estimate of the maximum penetration of the large temperature gradient into the fluid is for very large time, the height of 400 m is not surprising. The upper right-hand panel shows the simulation with a vertical grid spacing of 160 m at a much later time (five hours after the discontinuity first forms at the surface), and it is clear that the ribbon of high temperature gradient extends further into the fluid (perhaps up to 800 m). We ran other simulations further in time, but with a vertical resolution of 320 m. This resolution is not sufficient to resolve structure less than 1 km deep; therefore, no hint of a band of high-temperature gradient extending upward from the surface is evident.

Equation (17) can also be used to predict the surface location of the front using semi-geostrophic theory. This is simply given by the minimum of d which in physical space, y , occurs at -523 km. Since the anelastic equa-

tions are used in our simulations, the exact symmetry about the plane $z = H/2$ present in the Boussinesq equations for this problem is lost, resulting in a stronger upper boundary front as measured, say, by the strength of the along-front wind. This upper front is also farther from the axis of dilation than the front at the surface. Nevertheless, the asymmetry is not great; therefore, we do expect a reasonable comparison with semi-geostrophic theory. The upper front in our experiments is located at $y = 550$ km, while the lower front is near $y = -450$ km. The results from our simulation bracket the semi-geostrophic solution.

The considerable roughness of the temperature field, evident in Fig. 5, is a result of the production of gravity waves during the frontogenesis. These waves will also be quite evident in other figures to be described later. The details of the structure and generation of these waves will be the subject of a companion paper.

c. Vorticity in the frontal zone

Orlanski et al. (1985) argued that a natural process that limits frontogenesis occurs when ageostrophic accelerations within the frontal zone reduce the convergence necessary to maintain the unbounded growth of vertical vorticity. Without this growth, the frontogenesis would necessarily cease. Figure 6 shows the accelerations of the across-front ageostrophic velocity near the front, with the surface position of the front indicated by the arrow. Positive values indicate accelerations toward positive y ; thus these accelerations are clearly acting to reduce the convergence within the front.

Figure 7 shows the effect of these accelerations. The upper two panels show the along-front wind, the horizontal gradient of which is proportional to the vertical component of vorticity, while the lower panels show the front normal component, the horizontal gradient of which is proportional to divergence. The heavy dark lines are for reference, and are the same for each re-

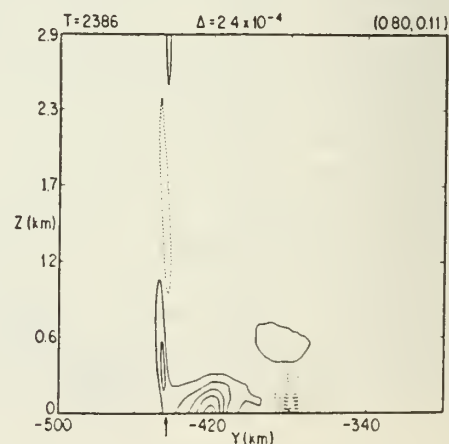


FIG. 6. Cross section of the ageostrophic acceleration. Contour interval (Δ) is m s^{-2} , and the arrow locates the surface position of the nose of the front. Dotted contours are negative.

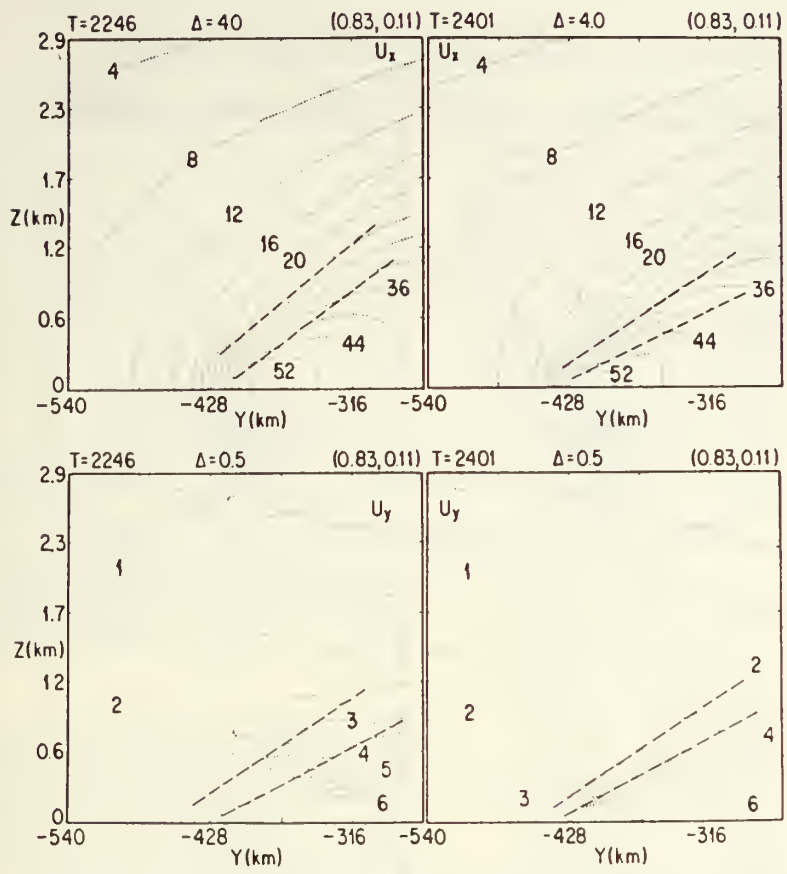


FIG. 7. Cross sections of along-front wind (U) and across-front wind (V). Δ gives the contour interval in m s^{-1} . Time and resolution are indicated as in Fig. 2. The heavy dashed lines are for reference and are at the same location in the upper and lower panels for the respective times.

spective time. They roughly indicate the region of maximum shear in the along-front wind component and the lower edge of the strong shear. Note that, at the earlier time, the region of maximum vorticity and convergence more or less coincide, while at the later time (which is still at least an hour from the time we project maximum surface frontogenesis to occur), the region of maximum convergence has moved to the lower edge of the zone of strong along-front wind shear. This is pretty much as predicted by Orlanski et al. However, this has little effect on the rate of frontogenesis. Figure 8 shows the vertical component of vorticity at several times spanning the interval shown in Fig. 7. By following certain contours (note that the contour interval doubles between the upper and lower panels), the reader should verify a steady increase in vorticity along the center line of the front, especially near the surface. The most rapid increase in vorticity occurs at the surface, as we would expect.

Figure 9 shows the variations of the maximum vorticity at the surface at various horizontal and vertical resolutions. The surface vorticity increases until about

$T = 2500$ min for all but the model with the highest resolutions. At later times, there is evidence for a slow but steady increase. At the maximum resolution, at the time of maximum surface frontogenesis, there is a very rapid growth in vertical vorticity to levels much higher than at any lower resolution. Beyond this time, the development of wave activity associated with the frontogenesis makes it difficult to determine that part of the pattern that is associated with the front itself.

Even though the natural process discussed by Orlanski does appear to be operating, namely, that near the time when the front is tending toward a discontinuity, the region of strongest convergence no longer coincides with the strongest vertical vorticity, the build-up in vorticity proceeds, and it is the vertical resolution that limits the frontogenesis. The apparent discrepancy between the location of the source of the vorticity (in the convergence zone) and the location of the maximum vorticity can be explained by noting that maximum vorticity will concentrate along the line where the total velocity perpendicular to the front is zero. The source need not exactly coincide with this line.

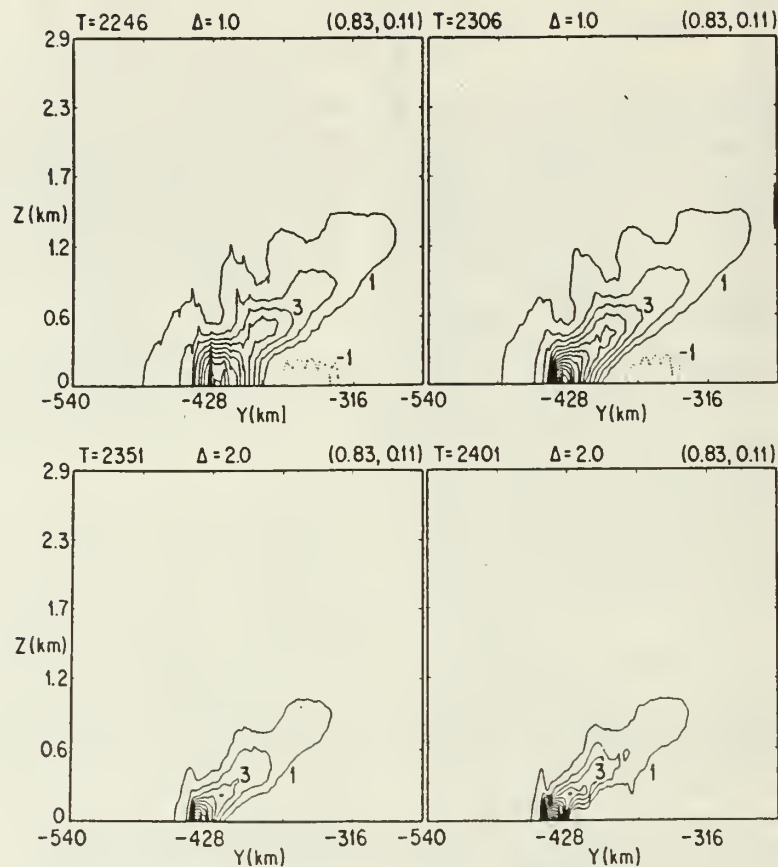


FIG. 8. Cross sections of the vertical component of relative vorticity. Contour interval (Δ) is $\times 10^{-4} \text{ s}^{-1}$; otherwise as in Fig. 2.

d. The energy spectra

There has been some speculation over the years that the famous -3 power law found in atmospheric spectra of kinetic energy (and in general circulation models) for zonal wavenumbers (on the globe) greater than about 10 or so may be due to fronts. There are, of course, other explanations (e.g., Charney, 1971); however, frontogenesis is an obvious cascade process whereby energy is introduced into shorter scales by the larger scales. Andrews and Hoskins (1972) have, in fact, shown that at the time when the discontinuity first forms at the surface, the kinetic energy spectrum is $-\frac{8}{3}$ which is, of course, quite close to -3 . Williams (1967), on the other hand, points out that, as the frontogenesis continues, as it would if the scenario proposed by Cullen and Purser (1984) were valid and the frontogenesis actually proceeds beyond the point of a discontinuity at the surface, then the distribution of velocity near the surface will approach a sawtooth distribution which has a -2 spectrum.

Near the center of the domain, no frontogenesis takes place; thus, in that region, the final spectrum will equal the original spectrum which for the problem here is

very steep (slope < -10). If we examine the spectrum at various levels from the surface up to the midlevel, we might expect spectra with slopes from -2 down to a very steep value as we go upward. The average over the entire domain will lie somewhere between these extremes.

The experiments we are considering here allow us to demonstrate whether or not the spectra at the surface go beyond $-\frac{8}{3}$ and approach -2 and what the vertical average will be for our experiment. Figure 10 shows the spectra computed over the width of the domain at a level of 0.2 km and for various times expressed in hours before our extrapolated onset of a discontinuity at the surface. This figure is similar to the one shown by Andrews and Hoskins (1978) for a semigeostrophic front and shows a long region of nearly constant slope up to a wavenumber of 20 in our domain, which corresponds to a horizontal scale of 180 km. Between wavenumbers 20 and 50 the slope is somewhat steeper, and, at even higher wavenumbers, peaks associated with waves forced by the front are evident.

The time variations of the slope of these spectra at low wavenumbers is shown in Fig. 11 for near the surface (0.2 km), at an intermediate level (1.8 km), and

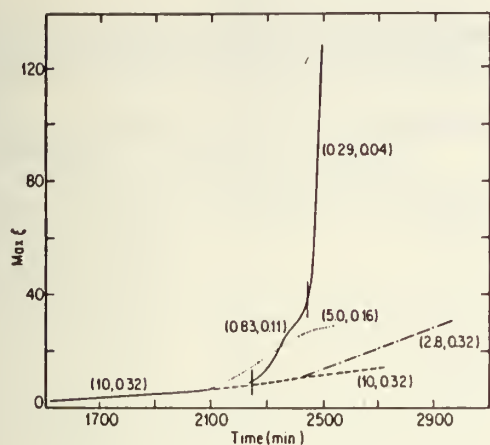


FIG. 9. Maximum vertical component of relative vorticity at the surface. The vertical lines on the solid curve show when the resolution of the model was changed. Resolution is indicated in km in parentheses, as in Fig. 2.

the vertical average. As expected, the spectrum near the surface has the shallowest slope and is close to -2 , although it clearly does not reach this value. The various symbols in the figure illustrate the slope computed for models with various resolutions. This information is included to show that, for the low wavenumbers, these results are independent of the resolution we used.

At midlevels, the slope approaches a limit slope more negative than -3 . The vertically averaged spectra have a slope that is clearly greater than -3 and, in fact, is rather close to -2 . Note, however, that at 2500 min (our time where the surface discontinuity first forms), the slope of the average is $-8/3$, although this is probably a coincidence. The surface spectrum at this time is already greater than $-8/3$.

These results are not intended to prove that fronts are responsible for the -3 spectrum. Rather they are intended to show the spectrum that might be expected with the type of front we are studying here.

4. Conclusions

Even using models with a vertical resolution of 35 m and a horizontal resolution of 280 m, the minimum scale achieved in a nonhydrostatic model for the stretching deformation forced front studied by Williams (1972) and others, never becomes less than several kilometers. Here we measure the frontal scale as the distance over which most of the horizontal temperature gradient is concentrated. The minimum scale reached in our experiments is at least an order of magnitude larger than the horizontal scale reported by Shapiro et al. (1985).

The scale of the front in this experiment is limited by the vertical resolution which is felt before the horizontal resolution, since the front is so nearly horizontal (slope $1/140$). We could find no natural mechanisms

in our nonhydrostatic two-dimensional model that eventually limit the front, such as the dynamical method suggested by Orlanski et al. (1985). The mechanism proposed by Orlanski et al. appears to be operating in our experiments, although it is too weak to stop the frontogenesis, at least down to the finest resolution we used.

In all our solutions, we could find no extraordinary frontogenetical processes that develop as the frontal

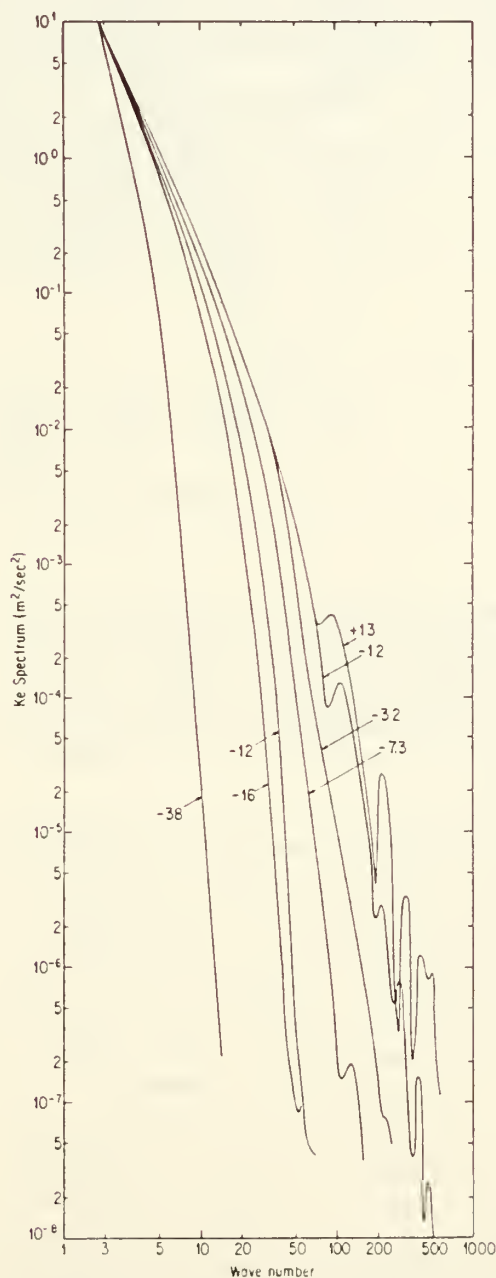


FIG. 10. Kinetic energy spectra. Numbers on the curves indicate the time in hours before the discontinuity would first form at the surface in a semigeostrophic model.

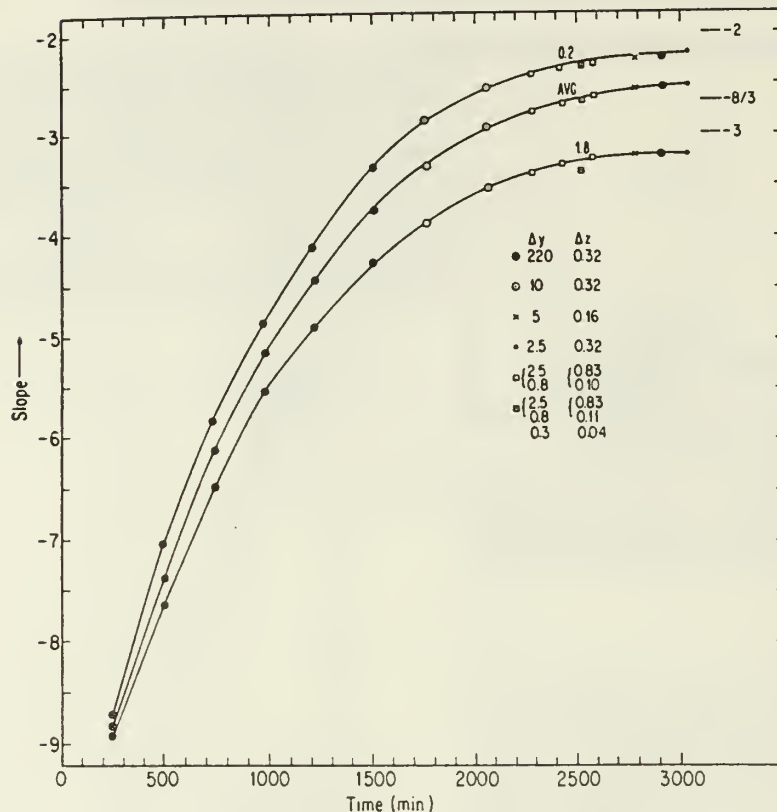


FIG. 11. Slope of the kinetic energy spectra between wavenumbers 3 and 10.

scale becomes very narrow, at least up to the point where the resolution stopped the frontogenesis. For the most part, semigeostrophic theory appears to apply in gross throughout our simulations. Thus it appears to us that the only mechanism that would limit this particular type of front would be diffusion or a termination of the forcing.

The proposal of Cullen and Purser (1984) that the semigeostrophic equations can be used to describe the frontogenesis beyond the point where a discontinuity first develops appears to give reasonable predictions of frontal structure. In particular, a ribbon of high-temperature gradient extending away from the surface appears in our solutions. Furthermore, the top of this ribbon remains, in our experiments, below the predictions of the maximum extent to which this ribbon is expected to extend as time tends to infinity.

Finally, we examined the energy spectra produced by the frontogenesis. Near the surface, this spectrum approaches a -2 slope, although it never reaches -2 . Away from the surface, the slope of the spectrum is considerably greater than at the surface. The slope of the vertically integrated energy spectrum is more negative than the slope of the spectrum at the surface, as expected, but is still considerably greater than the

$-8/3$ spectrum predicted by Andrews and Hoskins (1978) for the surface.

Considerable wave activity, apparently forced by the front, can be seen in many of the figures presented here. These waves, which are gravity waves, will be discussed at length in companion papers.

Acknowledgments. Most of the research reported here was performed while one of the authors, Robert Gall, held the NAVAIR George Haltiner Research Chair in Meteorology at the Naval Postgraduate School in Monterey, CA. Additional support was provided by NSF Grant ATM-8405276 at the Naval Postgraduate School and NSF Grants ATM-8407714 and ATM-8613514 at The University of Arizona. Computer calculations were performed at the National Center for Atmospheric Research. The final manuscript was edited by Margaret Sanderson Rae.

REFERENCES

- Andrews, D. G., and B. J. Hoskins, 1978: Energy spectra predicted by semigeostrophic theories of frontogenesis. *J. Atmos. Sci.*, **35**, 509–512.
- Bennets, D., and B. J. Hoskins, 1979: Conditional symmetric instability: A possible explanation of frontal rainbands. *Quart. J. Roy. Meteor. Soc.*, **105**, 945–962.

- Carbone, R. E., 1982: A severe frontal rainband. Part I: Stormwide hydrodynamic structure. *J. Atmos. Sci.*, **39**, 258–279.
- Charney, J., 1971: Geostrophic turbulence. *J. Atmos. Sci.*, **28**, 1087–1093.
- Clark, T., 1977: A small-scale dynamic model using a terrain-following coordinate system. *J. Comput. Phys.*, **24**, 186–215.
- , and W. R. Farley, 1984: Severe downslope windstorm calculations in two and three spatial dimensions using anelastic interactive grid nesting: A possible mechanism for gustiness. *J. Atmos. Sci.*, **41**, 329–350.
- Cullen, M., and R. Purser, 1984: An extended theory of semigeostrophic frontogenesis. *J. Atmos. Sci.*, **41**, 1477–1497.
- Eliassen, A., 1962: On the vertical circulation in frontal zones. *Geofys. Publ.*, **24**(4), 147–160.
- Emanuel, K. A., 1983a: The Lagrangian parcel dynamics of moist symmetric instability. *J. Atmos. Sci.*, **40**, 2368–2376.
- , 1983b: On assessing weak conditional symmetric instability from atmospheric soundings. *Mon. Wea. Rev.*, **111**, 2016–2033.
- Gall, R., R. Blakeslee and R. C. J. Somerville, 1979: Baroclinic instability and the selection of the zonal scale of the transient eddies of middle latitudes. *J. Atmos. Sci.*, **36**, 767–784.
- Hoskins, B., 1971: Atmospheric frontogenesis: Some solutions. *J. Atmos. Sci.*, **39**, 1999–2016.
- , and F. Bretherton, 1972: Atmospheric frontogenesis models: Mathematical formulation and solution. *J. Atmos. Sci.*, **29**, 11–37.
- Ley, B., and W. R. Peltier, 1978: Wave generation and frontal collapse. *J. Atmos. Sci.*, **35**, 3–17.
- Orlanski, I., B. Ross, L. Polinsky and R. Shaginaw, 1985: Advances in the theory of atmospheric fronts. *Advances in Geophysics*, Vol. 27, Academic Press, 223–252.
- Shapiro, M. A., T. Hampel, D. Rotzoll and F. Mosher, 1985: The frontal hydraulic head: A microscale (~1 km) triggering mechanism for convective weather systems. *Mon. Wea. Rev.*, **113**, 1166–1183.
- Smolarkiewicz, P., 1983: A simple positive definite advection scheme with small implicit diffusion. *Mon. Wea. Rev.*, **111**, 479–486.
- , 1984: A fully multidimensional positive definite advection transport algorithm with small implicit diffusion. *J. Comput. Phys.*, **54**, 325–362.
- Williams, R. T., 1967: Atmospheric frontogenesis: A numerical experiment. *J. Atmos. Sci.*, **24**, 627–641.
- , 1972: Quasi-geostrophic versus nongeostrophic frontogenesis. *J. Atmos. Sci.*, **29**, 3–10.
- , 1974: Numerical simulation of steady-state fronts. *J. Atmos. Sci.*, **31**, 1286–1296.
- , and J. Plotkin, 1968: Quasi-geostrophic frontogenesis. *J. Atmos. Sci.*, **25**, 201–206.

Lee Cyclogenesis. Part I: Analytic Studies

J. L. HAYES*, R. T. WILLIAMS AND M. A. RENNICK

Department of Meteorology, Naval Postgraduate School, Monterey, California 93943

(Manuscript received 3 March 1986, in final form 5 September 1986)

ABSTRACT

The growth of synoptic scale cyclones imbedded in a baroclinically unstable zonal flow over a long straight mountain range is investigated. Two different analytical models of the phenomenon are used.

The first model uses the linearized quasi-geostrophic equations. It allows a simple superposition of a steady state mountain forced solution and a transient Eady wave. There is no dynamic interaction between the two solutions, but the time evolution of the combined solution reproduces many characteristics of a disturbance passing over the Rocky Mountains.

The semigeostrophic equations are used in the second model. These equations allow a linear solution in transform space, but the transformation of the solution to physical space is nonlinear. This allows an interaction between the mountain forced and transient solutions. The minimum pressure developed by the semigeostrophic system is the same as that of the quasi-geostrophic system. However, the shape of the wave is distorted. This effect is caused by the divergent part of the mean flow over the mountain ridge.

1. Introduction

Observational studies (Petterssen, 1956; and more recently Reitan, 1974; Chung et al., 1976; Ziska and Smith, 1980) have shown that the lee sides of the major midlatitude topographic masses are preferred regions of cyclogenesis. In particular, the region to the south of the Alps has the highest frequency of new cyclone formation on earth. The study of lee cyclogenesis was one of the primary scientific objectives of the Alpine Experiment (ALPEX), carried out in this region in 1982. Lee cyclogenesis also occurs on the east side of the Rocky Mountains in the United States and Canada. Various numerical studies such as those by Egger (1974), Manabe and Terpstra (1974), Bleck (1977), Tibaldi et al. (1980), Mesinger and Strickler (1982) and Tosi et al. (1983) have concluded that inclusion of topography in numerical models is necessary to predict cyclogenesis in the "preferred" regions. However, the physical mechanisms that control lee cyclogenesis are not fully understood.

In this paper and the following one (which will be referred to as Part II), lee cyclogenesis will be investigated for a long meridional barrier perpendicular to the basic current. This arrangement will approximately represent conditions for Rocky Mountain lee cyclogenesis. It should be pointed out that the conditions for cyclogenesis in the lee of the Alps are quite different because the basic flow is roughly parallel to the mountain range. For the Rockies, the presence of a strong

jet stream during lee cyclogenesis has been thoroughly documented by Newton (1956), Klein (1957), Hovanec and Horn (1975) and Whittaker and Horn (1981). In the typical case a disturbance crosses the mountain range and grows rapidly over the lee slope.

Because of the association with a strong baroclinic current and the cyclone structure, it is generally agreed (e.g., see Pierrehumbert, 1985; Speranza et al., 1985) that lee cyclogenesis is the result of baroclinic energy conversion. The flow of a baroclinic current over a long ridge can give rise to a vertically sheared component along the ridge which would increase the magnitude of the horizontal temperature gradient in that region. This increased baroclinicity would favor baroclinic instability on the lee side of the range. A difficulty with this mechanism is that the disturbance may not remain in the zone of enhanced baroclinicity long enough to adjust its structure so that it will experience increased growth (Peng and Williams, 1986). Another possibility is that the high winds over the mountain area will cause an increased vertical tilt of the disturbance and therefore increased energy conversion. Speranza et al. (1985) examined the interaction of baroclinic waves with topography for a situation like the Alps where the mean flow is along the mountain range. They found no change in growth rate, but the solution structure was considerably modified. If the basic westerly flow were normal to the mountain range a cyclone would be deflected to the north until it reached the top of the ridge. This effect occurs because particles to the north of the low have relative motion down the slope which gives vertical stretching and a vorticity increase, and the opposite occurs for particles

* Present affiliation: Headquarters, Air Weather Service/DNX, Scott Air Force Base, Illinois.

to the south of the low. On the east side of the ridge, the process would reverse and the low would move to the south. This suggests that interaction between the cyclone and the topography will not produce lee cyclogenesis.

Farrell (1982, 1984) used the linearized quasi-geostrophic equations to demonstrate that continuous-mode solutions can, with proper initial conditions, exhibit large initial growth rates followed by the excitation of normal-mode solutions. He proposed that the continuous modes could be important in lee cyclogenesis. The difficulty with this effect is to find a tilting initial state which is relevant to flow over topography.

Smith (1984) has proposed a baroclinic lee wave mechanism for lee cyclogenesis in the Alps. This mechanism depends on a mean flow in which the vertical wind shear is opposite to the surface component across the mountain range. This fits the general conditions for lee cyclogenesis in the Alps that evolves into a major disturbance north of the Alps with southerly flow aloft and northwesterlies at the surface. This does not appear to apply to the Rockies because the vertical shear is usually in the same general direction as the surface wind. However, in his latest paper Smith (1986) shows that the effect could occur with the Rockies if the height variation along the crest is considered. In our studies this effect will be excluded since we will treat a mountain range with a uniform crest height except at the ends.

Another possibility is that cyclogenesis is actually the result of superposition. A steady flow over a synoptic-scale mountain forces a stationary high pressure ridge over the mountain and a pressure trough on the leeward side (e.g., see Smith, 1979). A growing synoptic disturbance of approximately the same scale as the mountains would be cancelled by superposition with the high pressure ridge as it moves over the topography. On the lee side, large growth rates would be observed as the cyclonic disturbance continues to grow and becomes superposed with the leeside trough. With a sufficiently high mountain, such leeside growth would appear as rapid deepening. In addition, the leeside superposition would induce a closed circulation at an earlier stage of the amplification process than would occur if the disturbance were over the mountain or flat terrain. As a result, the initial appearance of the closed surface pressure contour (which is defined as cyclogenesis in most climatological studies) would be increased by the presence of the mountain. This could explain the higher frequencies of cyclogenesis on the lee side of mountain ranges, since growing waves placed randomly would be more likely to have the first closed contour over the lee slope than elsewhere.

In section 2 we illustrate the superposition effect with an unstable Eady (1949) wave and the solution forced by an infinitely long mountain range. The quasi-geostrophic equations are used and when the motions are independent of y the equations become linear. Thus,

the mountain-forced solution and the unstable Eady solution are mathematically independent. The example chosen shows that the superposition of the two simple solutions can give a reasonable representation of lee cyclogenesis. These results are generalized in section 3 by using the semigeostrophic equations for the same physical situation, and by following the development of Bannon (1984). These solutions include the interaction between the mountain forced solution and the Eady solution through the Hoskins and Bretherton (1972) transformation. The effects of the mean wind changes over the mountain are included. The results are presented in section 4. They show that the minimum pressure in the wave moving over the mountain is not affected by the interaction with the mountain solution. However, the wave does speed up as it moves over the mountain, but it slows later. The vorticity in the wave decreases as it moves up the slope and increases as it moves down the slope.

2. Quasi-geostrophic motions independent of y

In this section lee cyclogenesis will be investigated with the quasi-geostrophic equations for an infinitely long mountain range. The geostrophic current normal to the mountain range, which is independent of time, is given by

$$U = U_s + \lambda z, \quad (2.1)$$

where U_s and λ are constants and $z = -\ln(p/p_0)$. The quasi-geostrophic potential vorticity equation with the Boussinesq approximation is written

$$\left[\frac{\partial}{\partial t} + U \frac{\partial}{\partial x} \right] \left[\frac{\partial^2 \phi}{\partial x^2} + \frac{f^2}{\Gamma} \frac{\partial^2 \phi}{\partial z^2} \right] = 0. \quad (2.2)$$

This equation employs the following additional conditions which were also used by Eady (1949):

- 1) $\partial f / \partial y = 0$,
- 2) $\partial \phi / \partial y = 0$,
- 3) static stability $= \Gamma = \text{constant}$.

Here ϕ is the geopotential with the portions related to (2.1) and Γ removed. The first law of thermodynamics is

$$\left(\frac{\partial}{\partial t} + U \frac{\partial}{\partial x} \right) \frac{\partial \phi}{\partial z} - \frac{\partial U}{\partial z} \frac{\partial \phi}{\partial x} + \Gamma \dot{z} = 0, \quad (2.3)$$

where \dot{z} is the vertical motion.

The motion is bounded by a rigid lid at $z = 1$ which represents the effect of the tropopause. Therefore the upper boundary condition is

$$\dot{z} = 0 \quad \text{at} \quad z = 1. \quad (2.4)$$

The lower boundary condition is given by

$$\dot{z} = \frac{U_s}{H} \frac{\partial h}{\partial x} \quad \text{at} \quad z = 0, \quad (2.5)$$

where $h(x)$ is the height of the topography and H is the scale height of the atmosphere. The boundary condition (2.5) has been linearized by applying it at $z = 0$ rather than at $z = h$.

Equation (2.2) and the boundary conditions (2.4) and (2.5) are linear when employed in (2.3) so that the various fields can be written in Fourier components as follows:

$$\phi = \tilde{\phi} e^{ikx}, \quad z = \tilde{w} e^{ikx}, \quad h = \tilde{h} e^{ikx}. \quad (2.6)$$

This Fourier decomposition imposes periodic boundary conditions in x . The governing equation (2.2) now becomes

$$\frac{\partial^2 \tilde{\phi}}{\partial z^2} - \frac{k^2 \Gamma}{f^2} \tilde{\phi} = 0, \quad (2.7)$$

and the boundary conditions are

$$\left[\frac{\partial}{\partial t} + ik(U_s + \lambda) \right] \frac{\partial \tilde{\phi}}{\partial z} - ik\lambda \tilde{\phi} = 0 \quad \text{at } z = 1, \quad (2.8)$$

$$\left(\frac{\partial}{\partial t} + ikU_s \right) \frac{\partial \tilde{\phi}}{\partial z} - ik\lambda \tilde{\phi} = \frac{-ikU_s \tilde{h} \Gamma}{H} \quad \text{at } z = 0. \quad (2.9)$$

The general solution to (2.7) subject to (2.8) and (2.9) is the sum of a transient solution ϕ_T , which satisfies the homogeneous version of (2.9), and the steady state mountain forced solution, ϕ_M . The transient solutions include the pair of discrete modes which were found by Eady (1949) and the continuous spectrum modes which were derived by Pedlosky (1964) (see also Farrel (1982, 1984)). The mountain forced solution is given by

$$\tilde{\phi}_M = -\frac{\Gamma U_s f \tilde{h}}{H(k\Gamma^{1/2} \alpha U_s - \lambda f \gamma)} \left[\alpha \sinh\left(\frac{k\Gamma^{1/2} z}{f}\right) + \gamma \cosh\left(\frac{k\Gamma^{1/2} z}{f}\right) \right], \quad (2.10)$$

where

$$r = \frac{k\Gamma^{1/2}}{f} \left(\frac{U_s}{\lambda} + 1 \right),$$

$$\alpha = 1 - r \tanh\left(\frac{k\Gamma^{1/2}}{f}\right),$$

$$\gamma = r - \tanh\left(\frac{k\Gamma^{1/2}}{f}\right).$$

The ageostrophic zonal wind can be computed from ϕ_M by using the quasi-geostrophic vorticity equation

$$\left[\frac{\partial}{\partial t} + (U_s + \lambda z) \frac{\partial}{\partial x} \right] \zeta = -f \frac{\partial u}{\partial x} \quad (2.11)$$

where ζ is the geostrophic vorticity, $1/f(\partial^2 \phi_M / \partial x^2)$.

As an example, let the mountain profile be described by

$$h(x) = z_* \left(A_0 + \sum_n A_n \cos \frac{2\pi n x}{L} \right), \quad (2.12)$$

where

$$A_0 = \frac{1}{4}, \quad A_n = \frac{\sin(n\pi/2)}{n\pi(1 - n^2/4)}. \quad (2.13)$$

Here z_* is the mountain height, and L is the width of the domain. This is the same east-west profile which is used in the numerical integrations that will be presented in Part II. Figure 1 shows this mountain profile as well as the sea level pressure and velocity perturbations associated with the steady mountain solution ϕ_M [Eq. (2.10)]. Note that (2.10) is not applied for $n = 0$ in the representation (2.12) because this case merely adds a constant to ϕ_M . The mountain forced solution consists of a ridge centered over the mountain peak and broad troughs over the flat terrain away from the mountain. Air parcels are deflected towards the north on the upstream side of the mountain, and towards the south on the downstream side. As a parcel moves up (down) the mountain slope, its absolute vorticity must decrease (increase) in order to conserve potential vorticity, requiring a divergent (convergent) secondary circulation. This is reflected in the ageostrophic zonal wind which increases on the upslope and decreases on the downslope. The result is a slight retardation of the mean zonal wind at the bases of the mountain and a stronger enhancement of the zonal wind over the mountain peak. The surface potential temperature is just proportional to the terrain height.

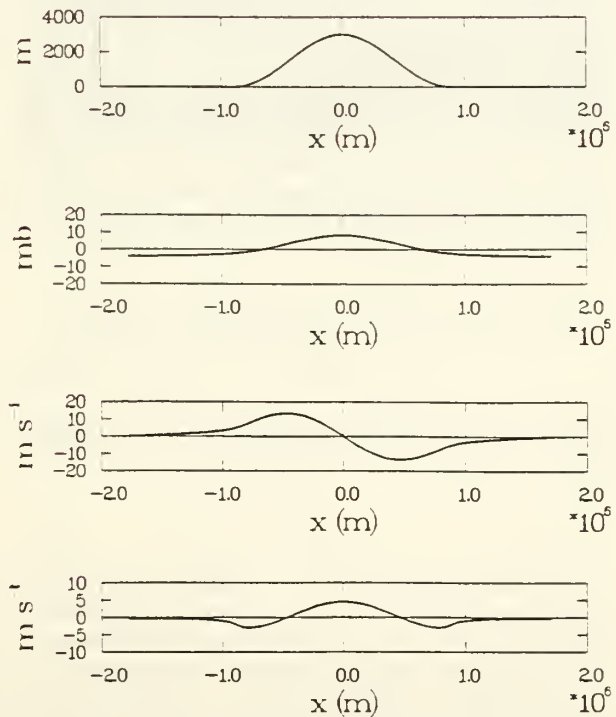


FIG. 1. Mountain forced solution using the Eady model with $U_s = 10 \text{ m s}^{-1}$, $\lambda = 20 \text{ m s}^{-1}$. (a) Mountain cross section, (b) surface pressure perturbation, (c) meridional wind, (d) ageostrophic zonal wind.

Note that ϕ_M is symmetric and v_M is antisymmetric about the mountain crest (see Fig. 1), as a result of the periodic boundary conditions. If the condition $v \rightarrow 0$ as $x \rightarrow -\infty$ were used, these symmetry properties would disappear and the flow would have a net deflection on crossing the ridge (e.g., see Merkin, 1975; Blumen and Gross, 1986). This deflection does not occur if the mountain is two-dimensional (Merkin and Kálanay-Rivas, 1976) or if the upper boundary is removed (Smith, 1979). The symmetry properties of the temperature and the ageostrophic zonal wind are unaffected by the upstream conditions on v (Blumen and Gross, 1986). This suggests that the use of periodic boundary conditions should not have an important effect on the realism of the mountain solutions. Also the periodic boundary conditions are appropriate for comparisons with the numerical solutions which will be given in Part II.

The solution shown in Fig. 1 is for the case with $f = 10^{-4} \text{ s}^{-1}$, Γ is $10^4 \text{ m}^2 \text{ s}^{-2}$, $L = 3537 \text{ km}$ (zonal wavenumber 8 at 45° latitude), $z_* = 3000 \text{ m}$, $H = 8000 \text{ m}$, $U_s = 10 \text{ m s}^{-1}$ and $\lambda = 20 \text{ m s}^{-1}$. As can be seen from (2.10), the magnitude of the mountain forced solution increases linearly with z_*/H . Its dependence on U_s and λ is less straightforward. The values of the pressure and ageostrophic wind perturbations, evaluated at the mountain peak are shown in Fig. 2 as functions of U_s and λ . In general, the magnitude of the solution increases for large surface winds and small vertical shear. For $\lambda > U_s$, the pressure perturbation is somewhat more sensitive to U_s than to λ , while the opposite is true for $\lambda < U_s$. The zonal wind perturbation, on the other hand, depends most strongly on U_s throughout the parameter range.

In order to represent a developing wave passing over topography, one of the unstable transient discrete mode solutions to (2.3), ϕ_T , is combined with ϕ_M . The discrete mode solutions are given by $\phi_T = Ae^{i(kx - ct)}$, where A is an arbitrary complex constant specifying the initial amplitude and phase of the transient wave and the phase speed is given by

$$c = U_s + \lambda/2 \pm \lambda \left\{ \frac{1}{4} - \frac{f}{k\Gamma^{1/2}} \left[\coth\left(\frac{k\Gamma^{1/2}}{f}\right) - \frac{f}{k\Gamma^{1/2}} \right] \right\}^{1/2}. \quad (2.14)$$

The phase speed is complex (and the wave unstable) for

$$k < \frac{2.4f}{\Gamma^{1/2}}. \quad (2.15)$$

The time evolution of an unstable transient wave and its superposition with the mountain forced solution are shown in Fig. 3. The solid lines show the transient (thin) and combined (heavy) pressure perturbations at several different times. The positions of the transient and combined troughs are indicated by the thin and heavy dashed lines, respectively. At $t = 0$, the transient

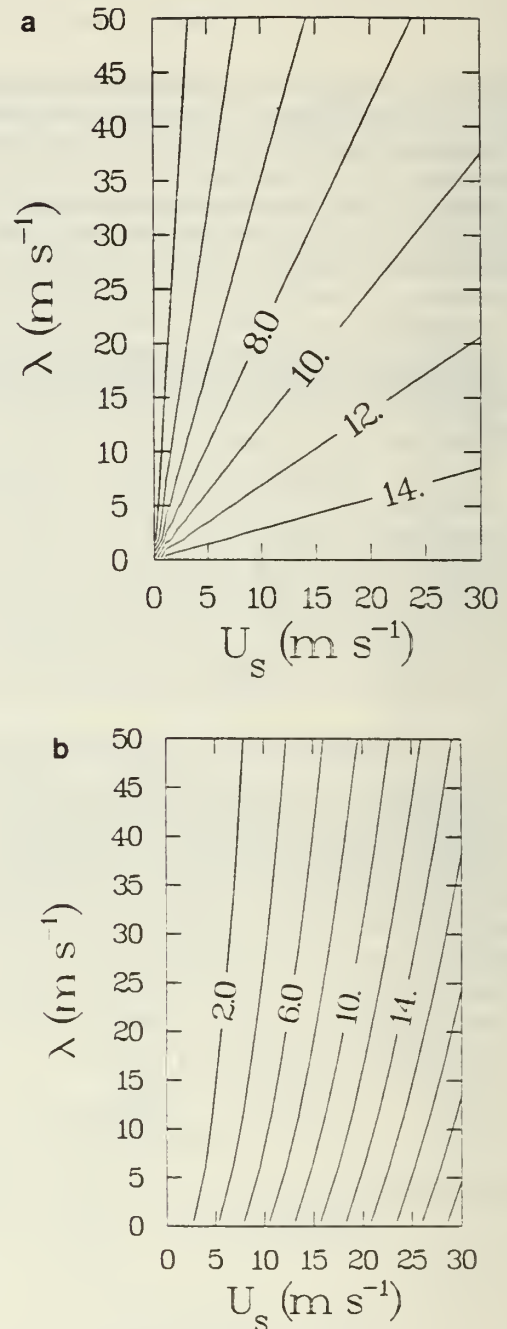


FIG. 2. Magnitude of mountain forced Eady solution at $z = 0$ as a function of basic state shear (λ) and surface wind (U_s). (a) Surface pressure perturbation (mb), (b) ageostrophic zonal wind (m s^{-1}).

wave is positioned with its trough about halfway up the windward slope of the mountain. At this location it is partially cancelled by the mountain forced ridge, so that the minimum pressure of the combined solution is located about 400 km to the west, at the base of the mountain. The cancellation between p_M and p_T is such that the combined mountain pressure distribution downstream of the mountain peak is almost uniform.

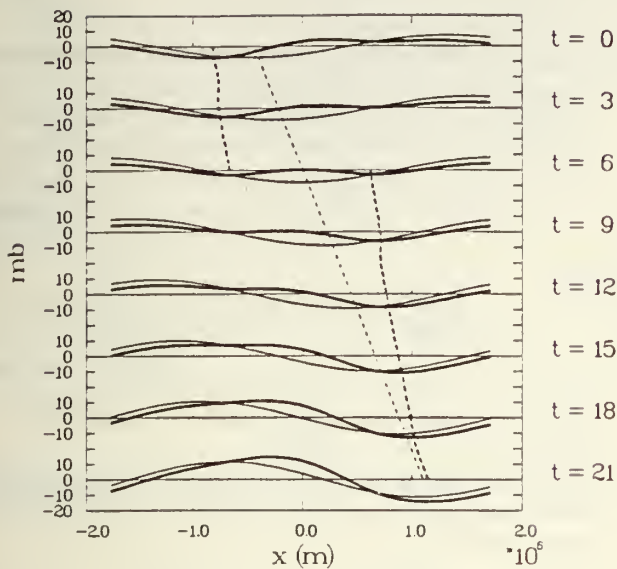


FIG. 3. Complete solution using the Eady model with $U_1 = 10 \text{ m s}^{-1}$, $\lambda = 20 \text{ m s}^{-1}$ and a wavenumber 8 disturbance. Solid lines are surface pressure perturbations; dashed lines show the position of the trough. Thin lines represent the transient solution; heavy lines represent the superposition of the forced and transient solutions.

As the transient trough moves up the mountain slope, its amplitude grows exponentially with a growth rate of $0.52d^{-1}$. This growth is masked, however, by the mountain forced ridge, so that the trough in the combined solution weakens and falls further behind the transient trough. By $t = 9 \text{ h}$, the combined trough is barely recognizable, and is located about 800 km to the west of the transient trough. At the same time, the influence of the growing wave is felt in the lee of the mountain, combining with the mountain forced solution to produce a weak trough at about $t = 3 \text{ h}$. This trough deepens as it remains nearly stationary at the foot of the mountain and then begins to propagate eastward as the transient trough approaches. By $t = 9 \text{ h}$ this is the principal trough. From 9 to 21 h this trough continues to deepen rapidly as it moves eastward, approaching the phase speed of the transient wave. When the combined solution is viewed in isolation, it appears as if a well-developed cyclonic disturbance slows down and dissipates as it approaches the mountain. Another disturbance forms in the lee of the mountain and amplifies rapidly as it moves slowly away from the mountain.

This behavior is very similar to observations preceding and during Rocky Mountain lee cyclogenesis. In a typical case (Palmen and Newton, 1969), a well-developed Pacific cyclone slows and weakens as it approaches the west coast of North America. As in the example above, an initially strong high pressure ridge centered over the Rockies appears to weaken considerably during the next 12–18 h. However, cyclogenesis follows along the lee slopes as rapid deepening and

slow eastward movement are observed during the first 6–12 hours after formation. As the cyclone moves away from the lee slope, the intensification is less rapid and the eastward phase speed increases. In the words of Palmen and Newton, the disturbance “behaves in a manner similar to a cyclone over flat terrain”.

A plot (Fig. 4) of minimum sea-level pressure perturbation and its location versus time for the combined and free solutions, shows the major stages of this sequence quite well. From $t = 0$ to $t = 6 \text{ h}$, the wave in the combined solution appears to weaken rapidly, suggesting a weakening surface cyclonic disturbance. Notice that during this period, the free solution continues to grow. After $t = 6 \text{ h}$, the pressure in the combined solution falls at a much faster rate than that of the free solution, suggesting rapid intensification. While the transient wave moves with constant phase speed at all times, the trough of the combined solution moves more slowly as it approaches the mountain and again as it reforms in the lee of the mountain. Its speed increases as it moves away from the mountain, approaching the speed of the transient wave by $t = 21 \text{ h}$.

The evolution of the system for the case of a stable transient wave is shown in Fig. 5. For this case the transient wave (thin lines) moves across the mountain with constant amplitude (solid line) and phase speed (dashed line). The behavior of the combined solution (heavy lines) is more similar to the unstable case. The combined trough fills as it approaches the mountain (0–6 h) and then deepens rapidly as it moves down the lee slope of the mountain (6–15 h). By hour 15 the trough is over relatively flat terrain and its amplitude deepens at a much slower rate. Unlike the unstable wave of the previous example, this disturbance moves up the mountain slope at a somewhat faster speed than

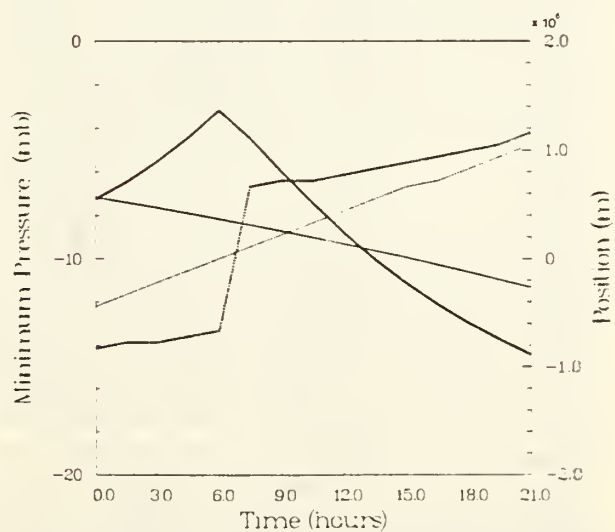


FIG. 4. Minimum pressure (solid lines) and trough location (dashed lines) of transient (thin lines) and combined (heavy lines) Eady solution vs time for $U_1 = 10 \text{ m s}^{-1}$, $\lambda = 20 \text{ m s}^{-1}$, wavenumber 8.

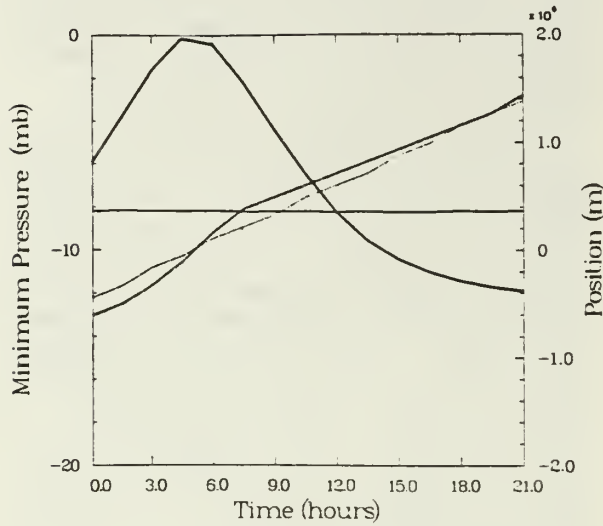


FIG. 5. As in Fig. 4 except for wavenumber 16.

that of the transient wave alone, but (as in the previous case) during the period of rapid development it moves down the mountain more slowly than the transient wave.

3. Semigeostrophic theory

In the previous section it was shown that the superposition of a growing baroclinic wave and a topographically forced high pressure area strongly resembled observed lee cyclogenesis. However, since the quasi-geostrophic equations are linear due to the lack of meridional variation, there is no dynamic interaction between the mountain forced flow and the wave. In order to consider the possibility that lee cyclogenesis is enhanced by such interactions, it is necessary to employ more general equations or to treat disturbances with meridional structure. The semigeostrophic equations described by Hoskins (1975) include the ageostrophic advections which are excluded in the quasi-geostrophic equations. That those advections may be important can be seen from Fig. 4, which shows that the magnitude of the ageostrophic zonal wind over the mountain top is roughly half that of the geostrophic component. These ageostrophic advections are removed by a coordinate transformation which leads to the quasi-geostrophic equations. However, the transformation back to physical space is nonlinear, so that the semigeostrophic equations will include dynamic interaction between the wave and the topographically forced flow. The general development is similar to that of Bannon (1984), who used the semigeostrophic equation to study the interaction between a front and an infinitely long mountain range. In his study, there was no vertical shear in the basic current and the frontogenesis was driven by horizontal deformation. Bannon also

used an unbounded atmosphere, while in this study, a lid is placed at the nondimensional height $z = 1$.

For a Boussinesq fluid, the potential vorticity equation can be written in Cartesian coordinates as follows:

$$\frac{dQ}{dt} = 0 \quad (3.1)$$

where

$$Q = \frac{\partial u}{\partial z} \frac{\partial \theta}{\partial y} - \frac{\partial v}{\partial z} \frac{\partial \theta}{\partial x} + \left(f + \frac{\partial v}{\partial x} - \frac{\partial u}{\partial y} \right) \frac{\partial \theta}{\partial z}, \quad (3.2)$$

when the hydrostatic approximation is used.

The semigeostrophic approximation is made by replacing (u, v) by (u_g, v_g) in (3.2).

As in the previous section, let $u_g = U = U_s + \lambda z$ where U_s and λ are constants. Equation (3.1) may then be rewritten as

$$\frac{dq}{dt} = 0 \quad (3.3)$$

where

$$q = -\frac{\partial v_g}{\partial z} \frac{\partial \theta}{\partial x} + \left(f + \frac{\partial v_g}{\partial x} \right) \frac{\partial \theta}{\partial z}. \quad (3.4)$$

Here, the first term on the right-hand side of (3.2) does not appear because it is constant. If the geostrophic angular momentum, $M = v_g + fx$, is introduced, the potential vorticity equation becomes

$$q = -\frac{\partial M}{\partial z} \frac{\partial \theta}{\partial x} + \frac{\partial M}{\partial x} \frac{\partial \theta}{\partial z} \equiv \frac{\partial(M, \theta)}{\partial(x, z)}. \quad (3.5)$$

The Hoskins geostrophic coordinate system is introduced with

$$X = x + \frac{v_g}{f}, \quad Z = z, \quad T = t. \quad (3.6)$$

The associated transformation formulas are

$$\frac{\partial}{\partial x} = \frac{\eta}{f} \frac{\partial}{\partial X} \quad (3.7)$$

$$\frac{\partial}{\partial z} = \frac{g}{f^2 \theta_0} \frac{\eta}{f} \frac{\partial \theta}{\partial x} \frac{\partial}{\partial X} + \frac{\partial}{\partial Z} \quad (3.8)$$

where

$$\eta = f + \frac{\partial v_g}{\partial x} = f \left/ \left(1 - \frac{1}{f} \frac{\partial v_g}{\partial x} \right) \right. \quad (3.9)$$

and θ_0 is a constant.

If Φ , the geopotential in transform space, is defined as

$$\Phi = \phi + \frac{v_g^2}{2} \quad (3.10)$$

where ϕ is the geopotential in physical space, it follows that

$$f v_g = \frac{\partial \Phi}{\partial X}, \quad \text{and} \quad \frac{g \theta}{\theta_0} = \frac{\partial \Phi}{\partial Z}. \quad (3.11)$$

A solution to (3.3) is $q = q_0 = \text{constant}$. If the initial transient part of v is sufficiently small, then by (3.4)

$$q_0 = f \frac{\partial \theta}{\partial z} = f \frac{\partial \bar{\theta}}{\partial z}, \quad (3.12)$$

where $\partial \bar{\theta} / \partial z$ is a constant static stability. The potential vorticity equation may be transformed into the geostrophic coordinate system as follows:

$$q = \frac{\partial(M, \theta)}{\partial(x, z)} = \frac{\partial(M, \theta)}{\partial(X, Z)} \frac{\partial(X, Z)}{\partial(x, z)} = \frac{\eta}{f} \frac{\partial(M, \theta)}{\partial(X, Z)}, \quad (3.13)$$

and since $M = fX$,

$$q = \eta \frac{\partial \theta}{\partial Z}. \quad (3.14)$$

Equating the two expressions for the potential vorticity (3.12) and (3.14), and using (3.9) we obtain

$$f \frac{\partial \bar{\theta}}{\partial Z} = \left[f / \left(1 - \frac{1}{f} \frac{\partial v_g}{\partial X} \right) \right] \frac{\partial \theta}{\partial Z}. \quad (3.15)$$

This can be rewritten using (3.11) as

$$\frac{\partial^2 \Phi}{\partial X^2} + f^2 \left\{ \frac{\theta_0}{g \partial \bar{\theta} / \partial z} \frac{\partial^2 \Phi}{\partial Z^2} - 1 \right\} = 0. \quad (3.16)$$

Now, it is convenient to remove the basic stratification by writing

$$\Phi(X, Z, T) = \bar{\Phi}(Z) + \Phi'(X, Z, T) \quad (3.17)$$

where

$$\frac{\partial \bar{\Phi}}{\partial Z} = \frac{g \bar{\theta}}{\theta_0}.$$

Substituting this into (3.16) results in the following

$$\frac{\partial^2 \Phi'}{\partial X^2} + \frac{f_0^2 \theta_0}{g \partial \bar{\theta} / \partial z} \frac{\partial^2 \Phi'}{\partial Z^2} = 0 \quad (3.18)$$

which states that the disturbance potential vorticity is zero. This corresponds to the quasi-geostrophic vorticity equation (2.2) in physical space. The time evolution comes from the first law of thermodynamics applied to the boundaries at $Z = 1$ and $Z = Z_s$. The semigeostrophic first law of thermodynamics (Hoskins and Bretherton, 1972) can be written for this case

$$\frac{\partial \theta}{\partial T} + (U_s + \lambda Z) \frac{\partial \theta}{\partial X} - \frac{f \theta_0}{g H} \lambda v + \dot{Z} \frac{\partial \theta}{\partial Z} = 0, \quad (3.19)$$

with the use of $\partial \theta / \partial y' = -(f \theta_0 / g H) \partial U_g / \partial Z = -f \theta_0 \times \lambda / g H$.

At the upper boundary,

$$\dot{Z} = 0 \quad \text{at} \quad Z = 1. \quad (3.20)$$

Following Bannon (1984), the lower boundary condition is partially linearized by applying it at $Z = 0$ rather than Z_s , and by replacing $\partial \theta / \partial Z$ by the constant $\partial \bar{\theta} / \partial Z$. Gross (1986) has evaluated this error for steady shear flow over a finite amplitude mountain. He found that the error increases with mountain height and shear,

but that it is still small. The error for time dependent motions was not evaluated. The forced vertical motion is given by

$$\dot{Z} = \frac{1}{H} \left(\frac{\partial h}{\partial T} + U_s \frac{\partial h}{\partial X} \right) \quad \text{at} \quad Z = 0. \quad (3.21)$$

The time dependence, $\partial h / \partial T$, is retained because, due to the time dependent coordinate transformation (3.6), the mountain height is not constant with respect to time in the transform space. However, it will be shown that the explicit time dependence is negligible. Notice that the boundary condition contains the ageostrophic advection through the coordinate transformation.

If the wave expressions (2.6) are introduced into (3.18) it takes the same form as (2.7). The boundary conditions (3.20) and (3.21), when inserted into (3.19), become

$$\left[\frac{\partial}{\partial T} + ik(U_s + \lambda) \right] \frac{\partial \bar{\Phi}}{\partial Z} - ik\lambda \bar{\Phi} = 0 \quad \text{at} \quad Z = 1 \quad (3.22)$$

$$\left[\frac{\partial}{\partial T} + ikU_s \right] \frac{\partial \bar{\Phi}}{\partial Z} - ik\lambda \bar{\Phi} = - \left(\frac{\partial}{\partial T} + ikU_s \right) \bar{h} \quad \text{at} \quad Z = 0. \quad (3.23)$$

The time derivative on the right hand side of (3.23) can be evaluated using the transformation formulas to give

$$\frac{\partial \bar{h}}{\partial T} = \frac{ik}{f} \frac{\partial v_g}{\partial t} \bar{h}.$$

The acceleration of the geostrophic wind may be approximated by $R_0 f v_g$, so that the ratio of the two inhomogeneous terms of (3.23) is given by $R_0 v_g / U_s$. For the case under consideration ($U \sim 10 \text{ m s}^{-1}$, $f \sim 10^{-4} \text{ s}^{-1}$, $L \sim 10^6 \text{ m}$) $R_0 \sim 0.1$ and the explicit time dependence in (3.23) is negligible so long as $v_g \leq U_s$. (Note that this result depends on the horizontal scale of the mountain, L . For a smaller scale mountain R_0 becomes larger and the time dependent terms become important.) With this approximation, the boundary conditions become equivalent to (2.8) and (2.9) except that \bar{h} is time dependent. Thus the equations in transform space are the quasi-geostrophic equations which were developed in section 2.

The transient and mountain forced solutions, Φ_T and Φ_M are computed in transform space as in section 2. The only difference is that, due to the time dependence of the boundary condition, Φ_M is time dependent and must be computed iteratively. The ageostrophic zonal wind component is computed in transform space following Hoskins and Draghi (1977)

$$u = u^* - \frac{\dot{Z}}{f^2} \frac{\partial^2 \Phi}{\partial X \partial Z}, \quad (3.24)$$

where u^* satisfies the vorticity equation corresponding to (2.11) in transform space. The solution is transformed to physical space through the inverse coordinate transformation

$$x = X - \frac{1}{f} [V_M(X, Z, T) + V_T(X, Z, T)] \quad (3.25)$$

where V_M and V_T are the meridional velocity components computed from Φ_M and Φ_T , respectively. The details of the interactive solution are given in the Appendix.

4. Semigeostrophic results

The analysis of the semigeostrophic solution is somewhat more complicated than that of the Eady solution. This is due to the time dependence of the lower boundary in semigeostrophic (SG) space. This affects the mountain forced transform geopotential $\Phi_M(X)$ directly, causing both Φ_M and its associated meridional velocity $V_M(X)$ to be time dependent. Thus, both V_M and V_T are time dependent in the expressions for the geopotential (3.10) and the ageostrophic wind (3.24), and in the transformations to physical space (3.25).

In order to simplify this situation somewhat, we look first at the isolated mountain solution with no transient disturbance. This eliminates the time dependence and allows the computation of a steady state mountain forced solution. In SG space, this solution is the same as the Eady solution, but for a modified mountain profile. Since V_M vanishes at the mountain top, the magnitudes of the pressure and ageostrophic wind perturbations are unchanged by the transformation to physical space. The transformation does affect the shape of the perturbation, however.

The difference between the semigeostrophic solution and the Eady solution is indicated by Fig. 6, which shows the difference in magnitude between the two solutions for p_M (surface pressure from mountain solution) and u_M for different values of the geostrophic wind parameters, U_s and λ . As noted previously, these differences are due solely to the change in the effective lower boundary. The general behavior of the semigeostrophic solution is similar to that of the Eady solution (compare to Fig. 2), but their magnitudes are slightly different. Except for very small values of the surface wind combined with very large values of the vertical shear (for which the mountain forced solution is weak in any case) the high pressure ridge generated

the semigeostrophic solution is somewhat weaker than that of the Eady solution. For the case considered in section 2 ($U_s = 10 \text{ m s}^{-1}$, $\lambda = 20 \text{ m s}^{-1}$) this difference is about 0.5 mb. The relative weakness increases (both in an absolute sense and relative to the magnitude of the ridge) for large surface wind and weak vertical shear. The magnitude of the ageostrophic zonal wind computed from the semigeostrophic solution is approximately double that of the Eady solution for all values of the parameters. This enhancement of the ageostrophic flow over the mountain crest was also found by Merkin (1975) for a barotropic mean flow.

Figure 7 illustrates the difference between the mountain forced Eady solution (same as Fig. 1) and the semigeostrophic (SG) solution with no transient

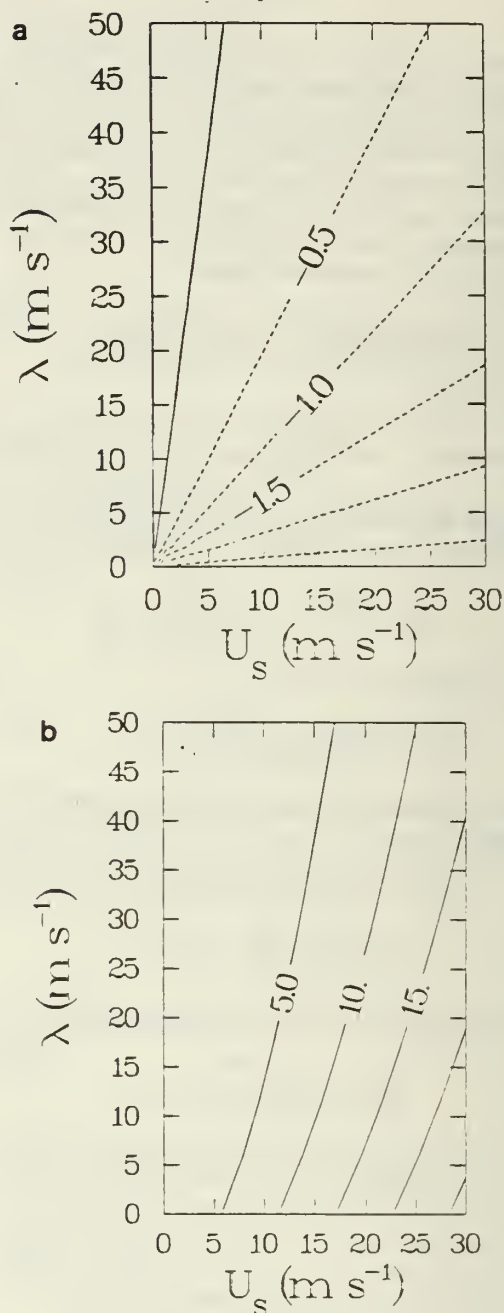


FIG. 6. As in Fig. 2 except showing the difference between the semigeostrophic and Eady solutions.

wave for the case $U_s = 10 \text{ m s}^{-1}$ and $\lambda = 20 \text{ m s}^{-1}$. In Fig. 7 the thin line represents the Eady solution while the heavy line is the SG solution. The height of the mountain surface is identical for the two solutions when viewed in physical space. Figure 7a shows both $h(x)$ (thin line) and $h(X)$ (heavy line) to illustrate the modification of the lower boundary required by the semigeostrophic coordinate transformation. This figure shows that for the mountain profile of (2.12) the semigeostrophic solution viewed in SG-space must be the same as the Eady solution corresponding to a mountain

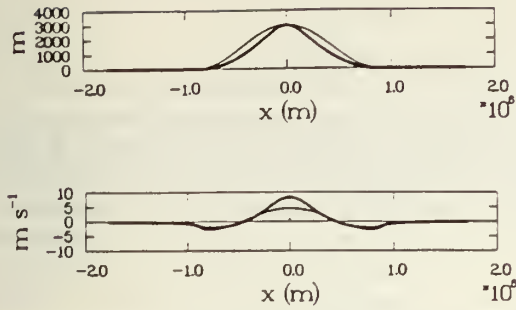


FIG. 7. Comparison of mountain forced Eady solution (thin lines) with semigeostrophic solution in the absence of a transient wave (heavy lines). (a) Mountain cross section (in transform space for semigeostrophic). (b) Ageostrophic zonal wind (both in physical space).

of the same height, but somewhat steeper profile. The SG solutions for the surface pressure and meridional wind (not shown) are almost identical to those of the Eady model (Fig. 1) except for a slight reduction in magnitude for the SG solution, as expected from Fig. 6. Not surprisingly, the ageostrophic zonal wind perturbation (Fig. 7b) shows the greatest difference between the two solutions. The acceleration of the zonal wind over the mountain top for the SG solution is about twice as strong as that for the Eady solution, whereas the deceleration up and downstream of the mountain is slightly weaker.

In order to understand the way in which the SG transformation affects the structure of a wave, it is helpful to consider the case of a transient wave with very small amplitude compared to the mountain forced solution. For this case, the meridional velocity required for the transformations (3.10), (3.24) and (3.25) is just the (time independent) mountain forced velocity. The effect of the mountain on the phase of the transient disturbance may be seen by substituting V_M for V in (3.25) and differentiating with respect to X .

$$\frac{\partial X}{\partial X} = 1 - \frac{1}{f} \frac{\partial V_M}{\partial X} \quad (3.26)$$

This result indicates that the horizontal dimension of the solution will be stretched in physical space (compared to SG space) when $\partial V_M / \partial X < 0$ and compressed when $\partial V_M / \partial X > 0$.

In physical terms, the stretching of the horizontal dimension corresponds to a phase acceleration of the solution, and the compression represents a deceleration. These effects are caused by the inclusion of advection by the ageostrophic wind in the SG equations. Inspection of Figs. 1c and 7d verifies that the physical solution is stretched where U_M is westerly (primarily over the mountain top) and compressed where U_M is easterly.

This phase acceleration may be seen in Fig. 8, which compares the transient Eady and transient SG solutions in physical space. The initial conditions are such that the two troughs are colocated upstream of the moun-

tain at the point where $\partial V_M / \partial X = 0$. As the SG trough (heavy line) moves through the region of westerly ageostrophic zonal wind ($t = 0-9$ h) it is accelerated with respect to the Eady trough (thin line). From $t = 9-18$ h the SG trough is in the region of easterly ageostrophic zonal wind and moves more slowly than does the Eady trough. The distortion of the wave shows a broadening of the trough as the wave moves up the slope and a sharpening as it moves down the leeside. This corresponds to a relative decrease of vorticity on the upwind side where there is divergence and a vorticity increase on the leeside where there is convergence.

The case which is physically relevant to lee cyclogenesis is that including a transient disturbance with magnitude on the order of the mountain forced solution. This is conceptually similar to the small amplitude example shown in Fig. 8. However, in this case V_T cannot be neglected in the transformation equations, thereby coupling the mountain forced and transient solutions, even in SG space.

The evolution of a growing SG wave and its relationship to the corresponding Eady wave are shown in Fig. 9. The thin lines in this figure represent the complete Eady solution, identical to Fig. 3. The heavy lines show the developing SG wave. The two solutions are quite similar, although close inspection reveals several differences. The structure of the two waves is somewhat different, with the SG wave having a broader upstream ridge and narrower lee trough than the Eady wave. Also, the lee trough develops somewhat more rapidly in the SG case as it moves down the mountain slope ($t \sim 6-15$ h). Downstream of the mountain the growth of the SG wave is inhibited so that by $t = 21$ h the two waves have virtually identical magnitude.

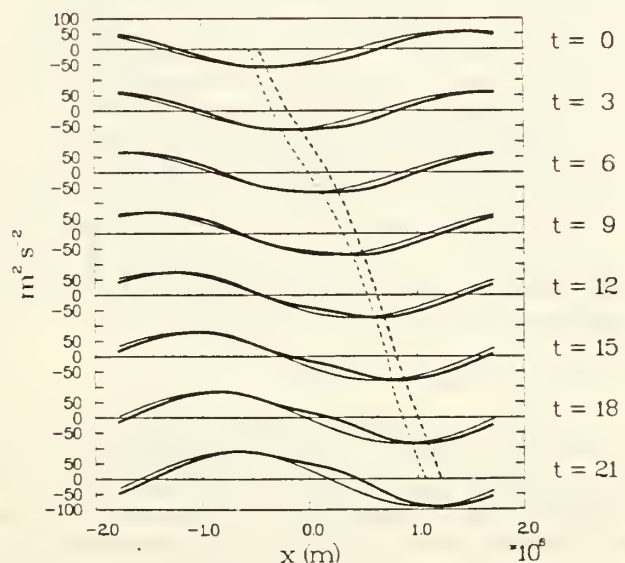


FIG. 8. Comparison of small amplitude transient solutions of Eady model (thin lines) and semigeostrophic model (heavy lines). Solid lines are magnitude of geopotential perturbation; dashed lines show trough position.

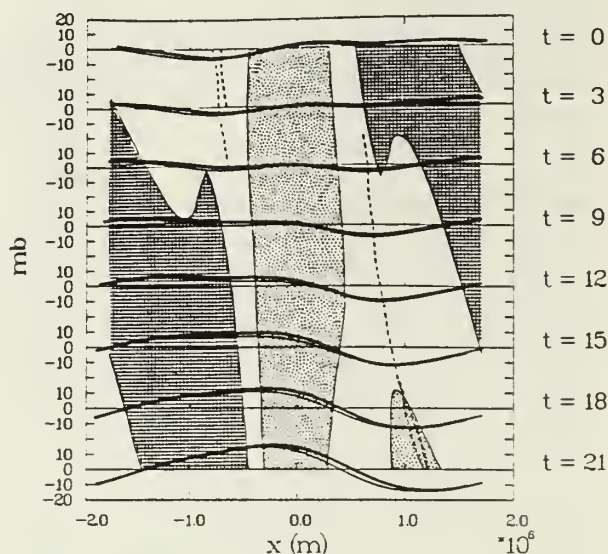


FIG. 9. Comparison of complete solutions for Eady model (thin lines) and semigeostrophic model (heavy lines). Solid lines are pressure perturbations; dashed lines show trough position. Stippling shows region with $U_a > 2 \text{ m s}^{-1}$; hatching shows regions with $U_a < -2 \text{ m s}^{-1}$.

To aid in the interpretation of these differences, the magnitude and sign of the ageostrophic zonal wind is also shown in Fig. 9. Regions in which U_a exceeds 2 m s^{-1} (20% of U_s) are indicated by stippling. Regions in which U_a is less than -2 m s^{-1} are indicated by hatching. For $t < 15 \text{ h}$ the wave trough is in the region of weak ageostrophic wind. This explains why the phase speeds of the two waves are virtually identical. For $t > 15 \text{ h}$, enhanced advection by the ageostrophic wind causes the SG wave to move ahead of the Eady wave. The distortion of the wave structure can also be understood in terms of the ageostrophic wind. In a broad region more than about 500 km upstream of the mountain peak advection is partially suppressed, while within 500 km on each side of the peak advection is enhanced. The result is the broadening of the upstream ridge and narrowing of the lee trough.

5. Summary and conclusions

In section 2 the quasi-geostrophic equations are used to study a baroclinic wave that crosses an infinitely long mountain range which is perpendicular to the baroclinic basic current. The lower boundary condition is linearized so that the solution can be separated into a time dependent Eady (1949) wave solution and a steady state mountain solution. The latter gives a high pressure area over the mountain ridge; the pressure difference between the ridge and the valley increases with the mean surface wind and decreases with the vertical wind shear. The solution of a baroclinic wave crossing the mountain is simulated by superposing the growing Eady solution upon the steady mountain so-

lution. The developing wave is partially cancelled as it moves up the mountain by the orographically forced high pressure ridge. As the wave moves down the lee slope it intensifies as it moves into the stationary lee trough. A similar result is found with a neutral wave solution. This simple example clearly resembles lee cyclogenesis although there is no dynamic interaction between the wave and the mountain.

The same physical problem is treated in section 3 with the semigeostrophic equations following Bannon (1984). When the Hoskins and Bretherton (1972) transformation is used the quasi-geostrophic equations are obtained in transform space. These equations are linear in transform space, but the transformation back to physical space is nonlinear. Because of the nonlinear transformation, an iterative procedure is developed to solve the equations. The results, which are given in section 4, show that although the moving wave is affected by the topography, its minimum pressure is not changed when compared with the quasi-geostrophic solution. However, the shape of the wave is distorted, and the wave moves more rapidly over the top of the mountain and it slows as it moves into the lee. The distortion of the disturbance corresponds to a relative vorticity decrease as the disturbance moves up the slope and an increase as it moves down. These effects are caused by the divergent part of the mean flow over the mountain ridge. After the disturbance moves away from the mountain there is no net orographic effect.

This simple study shows that the superposition of moving baroclinic waves upon a mountain forced high pressure area can lead to rapid growth of cyclones on the lee side of the mountain range. Clearly, the lee side superposition would induce a closed circulation at an earlier stage of the amplification process than would occur if the disturbance were over the mountain or flat terrain. As a result, the initial appearance of the closed surface pressure contour (which is defined as cyclogenesis in most climatological studies) would be increased by the presence of the mountain. The semigeostrophic solutions show that the cyclones are distorted by the divergent mean flow over the mountain range, but there is no significant effect on the wave growth. In Part II these results will be extended to more realistic solutions from a primitive equation numerical model. Both the basic state and the disturbance will be y -dependent and the mountain range will have a finite length. These numerical solutions will allow for both superposition effects and the possibility of enhanced baroclinic instability due to the interaction of the disturbance with the topography and the mountain forced mean flow.

Acknowledgments. The authors wish to thank Professor W. Blumen for his helpful comments on the manuscript. This research was supported by the Division of Atmospheric Sciences, National Science Foundation under Grant NSF ATM 8405276 and by the Naval Air Systems Command through the Naval Environmental Prediction Research Facility. The

manuscript was carefully typed by Penny Jones, and the numerical computations were performed by the W. R. Church Computer Center. The first author would like to thank his wife, Sharon, for her patience, understanding and support during the period of this research.

APPENDIX

Interactive Solution

The general solution to the semigeostrophic system of equations (3.18)–(3.21) may be written as the sum of a transient and mountain forced solution

$$\Phi(X, Z, T) = \Phi_T(X, Z, T) + \Phi_M(X, Z, T).$$

$\Phi_T = Ae^{ik(X-cT)}$ is the solution to the homogeneous form of the equations, where A is determined by the initial conditions and c is given by (2.14).

The mountain forced solution may be written as a sum of Fourier components $\Phi_M = \sum \tilde{\Phi}_{Mn} e^{inkX}$ where each coefficient satisfies an equation analogous to 2.10,

$$\tilde{\Phi}_{Mn} = -\frac{\Gamma U_s f \tilde{h}_n(T)}{H(k\Gamma^{1/2} \alpha U_s - \lambda f \gamma)} \left[\alpha \sinh\left(\frac{k\Gamma^{1/2} Z}{f}\right) + \gamma \cosh\left(\frac{k\Gamma^{1/2} Z}{f}\right) \right]. \quad (\text{A1})$$

Here the $\tilde{h}_n(T)$ describe the mountain surface in SG space,

$$h(X, T) = \sum \tilde{h}_n(T) e^{inkX}.$$

If the mountain surface in physical space is given by

$$\eta(x) = \sum \tilde{\eta}_n e^{inkx},$$

then (using 3.25) the \tilde{h}_n are given by

$$\sum \tilde{h}_n(T) \exp(inkX) = \sum \tilde{\eta}_n \exp[ink(X - V/f)] \quad (\text{A2})$$

where

$$V = \frac{1}{f} \frac{\partial}{\partial X} (\Phi_T + \Phi_M) = \frac{ik}{f} (Ae^{ik(X-cT)} + \sum \tilde{\Phi}_{Mn} e^{inkX}). \quad (\text{A3})$$

Equations (A1)–(A3) are solved iteratively using an initial estimate $V^{(0)} = 0$, $\tilde{h}_n^{(0)} = \tilde{\eta}_n$. The i th solution, $\tilde{\Phi}_{Mn}^{(i)}$, is found from (A1) using $\tilde{h}_n^{(i)}$, and $V^{(i)}$ from (A3). Then the $\tilde{h}_n^{(i+1)}$ are computed from (A2) using a fast Fourier transform. For the mountain profile used in this study, the solution converges to within 1% of the mountain height in 4–8 iterations.

REFERENCES

- Bannon, P., 1984: A semigeostrophic model of frontogenesis over topography. *Beitr. Phys. Atmos.*, **57**, 393–408.
- Bleck, R., 1977: Numerical simulation of lee cyclogenesis in the Gulf of Genoa. *Mon. Wea. Rev.*, **105**, 428–445.
- Blumen, W., and B. D. Gross, 1986: Semigeostrophic disturbances in a stratified shear flow over a finite-amplitude ridge. *J. Atmos. Sci.*, (in press).
- Chung, C. S., K. Hage and E. Reinelt, 1976: On lee cyclogenesis and airflow in the Canadian Rocky Mountains and the East Asian Mountains. *Mon. Wea. Rev.*, **104**, 878–891.
- Eady, E., 1949: Long waves and cyclone waves. *Tellus*, **3**, 33–53.
- Egger, J., 1974: Numerical experiments on lee cyclogenesis. *Mon. Wea. Rev.*, **102**, 847–860.
- Farrell, B. F., 1982: The initial growth of disturbances in a baroclinic flow. *J. Atmos. Sci.*, **39**, 1163–1186.
- , 1984: Modal and nonmodal baroclinic waves. *J. Atmos. Sci.*, **41**, 668–673.
- Gross, B. D., 1986: Semigeostrophic disturbance over finite-amplitude topography in a rotating stratified shear flow. M.S. thesis, University of Colorado.
- Hoskins, B. J., 1975: The geostrophic momentum approximation and the semigeostrophic equations. *J. Atmos. Sci.*, **32**, 233–242.
- , and F. Bretherton, 1972: Atmospheric frontogenesis models: Mathematical formulation and solution. *J. Atmos. Sci.*, **29**, 11–37.
- , and I. Draghici, 1977: The forcing of ageostrophic motion according to the semigeostrophic equations and in an isentropic coordinate model. *J. Atmos. Sci.*, **34**, 1858–1867.
- Hovane, R. D., and L. H. Horn, 1975: Static stability and the 300 mb isotach field in the Colorado cyclogenetic area. *Mon. Wea. Rev.*, **103**, 18–36.
- Klein, W., 1957: The frequency of cyclones and anticyclones in relation to the mean circulation. *J. Meteor.*, **15**, 98–102.
- Manabe, S., and T. Terpstra, 1974: The effects of mountains on the general circulation of the atmosphere as identified by numerical experiments. *J. Atmos. Sci.*, **31**, 3–42.
- Merkine, L.-O., 1975: Steady finite-amplitude baroclinic flow over long topography in a rotating stratified atmosphere. *J. Atmos. Sci.*, **32**, 1881–1893.
- , and E. Kalnay-Rivas, 1976: Rotating stratified flow over finite isolated topography. *J. Atmos. Sci.*, **33**, 908–922.
- Mesinger, F., and R. F. Strickler, 1982: Effect of mountains on Genoa cyclogenesis. *J. Meteor. Soc. Japan*, **60**, 326–337.
- Newton, C. W., 1956: Mechanisms of circulation change during a lee cyclogenesis. *J. Meteor.*, **13**, 528–539.
- Palmen, E., and C. W. Newton, 1969: *Atmospheric Circulation Systems*. Academic Press, 603 pp.
- Pedlosky, J., 1964: The stability of currents in the atmosphere and ocean: Part I. *J. Atmos. Sci.*, **21**, 201–219.
- Peng, M. S., and R. T. Williams, 1986: Spatial instability of the barotropic jet with slow streamwise variation. Submitted to *J. Atmos. Sci.*
- Pettersen, S., 1956: *Weather Analysis and Forecasting*, Vol. I. McGraw Hill, 428 pp.
- Pierrehumbert, R. T., 1985: A theoretical model of orographically modified cyclogenesis. *J. Atmos. Sci.*, **42**, 1244–1258.
- Reitan, C., 1974: Frequencies of cyclones and cyclogenesis for North America, 1951–1970. *Mon. Wea. Rev.*, **102**, 861–868.
- Smith, R. B., 1979: The influence of mountains on the atmosphere. *Advances in Geophysics*, Vol. 21, Academic Press, 87–230.
- , 1984: A theory of lee cyclogenesis. *J. Atmos. Sci.*, **41**, 1159–1168.
- , 1986: Further development of a theory of lee cyclogenesis. Submitted to *J. Atmos. Sci.*
- Speranza, A., A. Buzzi, A. Trevisan and P. Malguzzi, 1985: A theory of lee cyclogenesis in the lee of the Alps. Part I: Modifications of baroclinic instability by localized topography. *J. Atmos. Sci.*, **42**, 1521–1535.
- Tibaldi, S. A., A. Buzzi and P. Malguzzi, 1980: Orographically induced cyclogenesis: Analysis of numerical experiments. *Mon. Wea. Rev.*, **108**, 1302–1314.
- Tosi, E., M. Fantini and A. Trevisan, 1983: Numerical experiments on orographic cyclogenesis: Relationship between the development of the lee cyclone and the basic flow characteristics. *Mon. Wea. Rev.*, **111**, 799–814.
- Whittaker, L. M., and L. H. Horn, 1981: Geographical and seasonal distribution of North American cyclogenesis, 1958–1977. *Mon. Wea. Rev.*, **109**, 2312–2322.
- Ziska, K. M., and P. J. Smith, 1980: The climatology of cyclones and anticyclones over North America and surrounding ocean environs for January and July, 1950–1977. *Mon. Wea. Rev.*, **108**, 387–401.

Lee Cyclogenesis: Part II: Numerical Studies

J. L. Hayes*

R. T. Williams

M. A. Rennick

**Department of Meteorology
Naval Postgraduate School
Monterey, CA 93943-5000**

*Present affiliation: Detachment 30, 2nd Weather Squadron, Vandenburg Air Force Base, CA 93437.

Abstract

The effect of topography on the evolution of a disturbance in a baroclinically unstable mean flow is studied using a three-dimensional primitive equation model. A procedure is developed to compare control integrations with no topography with integrations which contain topography. It is found that lee cyclogenesis is caused primarily by the superposition of a growing baroclinic wave with a steady, orographically forced wave of the same scale. Some additional lee growth is found that may be orographically enhanced, or it may be related to certain small problems in the experimental setup. As the disturbances move over the ridge they are deflected to the north on the upwind side before returning to their original latitudes on the lee side. The numerical results in this paper are in general agreement with our analytic study (Hayes, Williams, and Rennick, 1987).

1. Introduction

In our previous paper (Hayes, et al., 1987), referred to as Part I, we studied a baroclinic wave that crossed an infinitely long mountain range perpendicular to the baroclinic basic current. Two analytic models were used for the study. The first model employed the quasi-geostrophic equations with a linearized lower boundary condition. A transient Eady (1949) wave was superposed on the steady state mountain forced solution. There was no dynamic interaction between the two solutions (since the governing equations were linear), but the time evolution of the combined solution reproduced many characteristics of a disturbance passing over the Rocky Mountains. As the growing Eady wave moved up the mountain it was partially cancelled by the orographically forced high pressure area, and as it moved down the lee slope it intensified when it moved into the stationary lee trough. The second model used the semi-geostrophic equations following Bannon (1984) to study the same physical problem. When the Hoskins and Bretherton (1972) transformation was used the quasi-geostrophic equations were obtained in transform space, but the transform back to physical space was nonlinear. The results showed that, although the moving wave was affected by the topography, the minimum pressure was not changed when compared with the quasi-geostrophic solution. However, the shape of the wave was distorted, and the wave moved more rapidly over the top of the mountain slowing as it moved into the lee. The distortion of the disturbance corresponded to a relative vorticity decrease as the disturbance moved up the slope and an increase as it moved down. These effects were caused by the divergent part of the mean flow over the mountain ridge. After the disturbance moved away from the mountains there was no net orographic effect.

The objective of the current study is to generalize the conclusions from Part I by using more accurate equations and more realistic mean flows and topography. The primitive equations in sigma coordinates (Phillips, 1957) are employed on a sector of the globe with a wall at the Equator. The mean flow is a mid-latitude jet with vertical and horizontal shear. The mountain range has the same cross-section as the range in Part I, but it is of finite latitudinal extent. Numerical solutions are obtained with and without topography, and a technique is developed to compare them. The initial disturbance amplitude is varied so that linear and nonlinear effects can be evaluated and compared with results from Part I.

In Part I four possible mechanisms for lee cyclogenesis were discussed. The enhanced baroclinic instability mechanism (1) involved the destabilization of the mean flow by the topography. The continuous mode mechanism (2), which was proposed by Farrell (1982, 1984), requires an initial disturbance that will grow rapidly for a short time through the continuous modes. The superposition mechanism (3) involves the combination

of a moving disturbance and a topographically forced high pressure area. The lee wave mechanism (4), that was formulated by Smith (1984, 1986) requires a vertical wind shear that is opposite to the surface wind across the topography. In Part I mechanisms (1) and (3) were considered. The semi-geostrophic solutions included the effects of the topographically modified mean flow, but there was no net effect on the lee cyclogenesis. However, it was shown that the superposition effect [mechanism (3)] could explain some features of Rocky Mountain lee cyclogenesis. The baroclinic lee-wave mechanism (4) will not be considered in this study because our mountain ridge does not have significant north-south variation in the ridge height (see Smith, 1986). The numerical experiments we present will be designed to compare the enhanced instability mechanism (1) with the superposition mechanism (3). Hayes (1985) investigated the continuous spectrum baroclinic instability [mechanism (2)] with an initial state which had the vertical structure of the mountain forced wave. A linearized spectral model was integrated with this initial state, and no growth was found until much later when the discrete mode growth became important. A similar experiment with a nonlinear finite difference model led to the same conclusion. However, an initial disturbance with backward tilt with height would grow rapidly, at least initially.

The numerical solutions with topography will be compared with control solutions that use a flat lower boundary. Our main objective is to evaluate the relative importance of superposition and enhanced instability on disturbance growth. However, we are also interested in topographic modifications in the movement of the disturbance cyclone. Based on the semigeostrophic solutions in Part I, we expect that the cyclone will move more rapidly over the mountain ridge than the control cyclone. We also expect other effects that were not in Part I because the cyclones in the present study have a finite latitudinal extent. If a basic westerly flow is normal to a north-south mountain range, a cyclone would be deflected to the north until it reached the top of the ridge. This effect occurs because particles to the north of the low have relative motion down the slope which gives vertical stretching and a vorticity increase. The opposite occurs for particles to the south of the low. On the east side of the ridge, the process would reverse and the low would move to the south. Buzzi *et al.* (1987) have isolated this mechanism with a linear analysis of unstable baroclinic waves passing over a mountain range which is perpendicular to the basic baroclinic flow. This mechanism was also analyzed by Speranza *et al.* (1985) for a cyclone moving along an east-west ridge.

The numerical model that will be used in this study is described in Section 2. The initial conditions and topography are specified in Section 3. The experimental procedure and the numerical solutions are presented in Section 4, and detailed comparisons among the solutions are given in Section 5. The summary and conclusions are in Section 6.

2. The Numerical Model

This section describes the numerical model that will be used for the numerical simulations. This study employs a version of the UCLA general circulation model designed specifically to provide an accurate representation of air flow over topography. The basic horizontal differencing scheme was developed by Arakawa and Lamb (1981) to conserve the domain-averaged square of the potential vorticity, and it approximately conserves the potential vorticity of individual parcels. Arakawa and Lamb (1981) have shown that, for a given coarse grid, simulations of the airflow over steep topography are significantly improved when this scheme is used. In our study, airflow over a long, narrow mountain is treated, and it is believed that the UCLA model will provide a good simulation of the flow

The model consists of the primitive equations for an inviscid, adiabatic, and hydrostatic atmosphere; moisture and its effects are not included. The prognostic variables are the horizontal components (u, v) of the wind velocity, potential temperature (θ), and pressure ($\pi = p_s - p_t$). The model's vertical coordinate is σ , which is defined as

$$\sigma = \frac{p - p_t}{p_s - p_t} \quad (2.1)$$

where p_s is surface pressure and p_t is the pressure at the top of the model atmosphere. Although $p_t = 200$ mb in this study, it is not expected that this will cause a problem since Charney and Drazin (1961) have shown that the wave-lengths shorter than the planetary scale are trapped in the vertical. The domain is a 45° sector of the Northern Hemisphere with a wall at the equator and a cyclic continuity at the east and west boundaries. The variables are staggered horizontally according to Arakawa's Scheme C with a grid spacing of approximately 2.8° longitude by 2.75° latitude. The variables are staggered vertically in six layers spaced equally in σ . Spatial derivatives are approximated using a fourth-order finite difference scheme. The vertical differencing scheme, developed by Arakawa and Suarez (1983), has excellent integral properties and it eliminates the systematic error in the hydrostatic equation that was present in previous models.

The model integration proceeds in a series of one Euler-backward time step followed by five centered time steps. Convergence of the meridians toward the poles would normally require the use of an extremely short time step to maintain computational stability. To avoid this requirement, the technique of smoothing zonal derivatives (Arakawa and Lamb, 1977) is used with a six minute time step.

3. Initial Conditions and Topography

In this section analytic expressions for the mean flow and the topography are specified. The basic current is selected to be baroclinically unstable as was the case in Part I, but horizontal shear is also included so that the wind profiles can better represent atmospheric conditions. The baroclinic portion of the mean zonal wind is given by

$$\bar{u}_T[\phi, p(\sigma, \phi)] = U_T \operatorname{sech}^2 [\gamma(\phi - \phi_0)] (\ln(p_0/p) / \ln(p_0/p_t)), \quad (3.1)$$

where $U_T = 40 \text{ ms}^{-1}$, $\phi_0 = 45^\circ \text{ N}$, $p_0 = 1013.25 \text{ mb}$, $p_t = 200 \text{ mb}$, and γ is the halfwidth of the jet. The maximum wind at each level occurs at 45° N , and the wind speed varies linearly with the logarithm of pressure. This expression approximates profiles given by Palmen and Newton (1969) from case studies of lee cyclogenesis. By setting the halfwidth of the jet, γ , equal to 8° latitude, a horizontal profile that agrees quite well with the observed wind prior to cyclogenesis is obtained. However, this profile meets the necessary condition for barotropic instability in regions to the north and south of the jet stream. Consequently, a profile in which $\gamma = 16^\circ$, that does not meet this criterion, is included in this study to isolate the baroclinic effects. A meridional cross-section of the initial mean state velocity field is shown in Fig. 1.

A mean surface current, necessary for strong topographic effects, is included with the same latitudinal structure as the baroclinic part:

$$\bar{u}_s(\phi) = U_s \operatorname{sech}^2 [\gamma(\phi - \phi_0)] \quad (3.2)$$

where γ and ϕ_0 are defined above and $U_s = 5 \text{ ms}^{-1}$. The upper-level wind given by (3.1) is modified by adding the surface current and applying the gradient correction to account for the earth's sphericity:

$$\bar{u}[\phi, p(\sigma, \phi)] = \Omega a \cos \phi \{ [1 + 2(\bar{u}_T + \bar{u}_s) / \Omega a \cos \phi]^{1/2} - 1 \} \quad (3.3)$$

where a is the radius of the earth, Ω is the earth's rotation rate, and u_T and u_s are given by (3.1) and (3.2) respectively. This equation is obtained by neglecting the acceleration in the latitudinal equation of motion and by setting the geostrophic wind equal to $u_T + u_s$.

Upper-level temperature is specified by integrating the geostrophic thermal wind equation which gives:

$$T(\phi, p) = T(\phi_0, p) + (a/R) \int_{\phi_0}^{\phi} f(\partial \bar{u}_T / \partial \ln p) d\phi \quad (3.4)$$

where $T(\phi_0, p)$ is the temperature at 45° N and u_T is given by (3.1). The integral in (3.4) is evaluated using Simpson's rule. All of these expressions are in pressure coordinates, and they must be transferred to σ coordinates with (2.1).

Mean surface pressure is initialized from the mean surface wind using the geostrophic wind equation:

$$\bar{p}_s(\phi) = \exp\{\ln \bar{p}_s(\phi_0) - (a/R) \int_{\phi_0}^{\phi} f \bar{u}_s(\phi) / \bar{T}_s(\phi) d\phi\}, \quad (3.5)$$

where $p_s(\phi_0 = 45^\circ \text{N}) = 1013.25 \text{ mb}$, $u_s(\phi)$ is given by (3.2), and $T_s(\phi)$ represents the mean surface temperature. The integral in (3.5) is also evaluated using Simpson's rule. Since p_s is not known, $T_s(\phi)$ cannot be found from (3.4). Therefore $p_s(\phi)$ is computed iteratively as follows: an initial guess is made for T_s ; $p_s(\phi)$ is computed using (3.5); T_s is then obtained from (3.4) and a new $p_s(\phi)$ is derived from (3.5); this latter step is repeated until the adjustment of T_s is less than 0.01°K . The solution converges in approximately 10 iterations.

The initial barotropic disturbance consists of a weak wave that varies sinusoidally with longitude. The maximum amplitude of the disturbance occurs at 45°N . Fields are balanced geostrophically with a constant f and are given by

$$\Phi' = f_0 A \sin(n\lambda) \sin^2(2\phi), \quad (3.6a)$$

$$p' = p_0 \Phi' / RT_0, \quad (3.6b)$$

$$u' = -(1/f_0 a) \partial \Phi' / \partial \phi, \quad (3.6c)$$

$$v' = 1/(f_0 a \cos \phi) \partial \Phi' / \partial \lambda, \quad (3.6d)$$

$$T' = 0, \quad (3.6e)$$

where $T_0 = 273^\circ \text{K}$ and $p_0 = 1013.25 \text{ mb}$. Test integrations in which the initial wave number of the disturbance is varied show that the wave number 8 perturbation is most unstable, and therefore, it is the only one used in this study

The surface topography is designed to resemble the Rocky Mountains as a long, meridional barrier to westerly flow. It is given by

$$\hat{z}_m(\phi, \lambda) = \begin{cases} z_* (\phi) \cos^2 \left[\left(\frac{\lambda - \lambda_0}{4\Delta\lambda} \right) \frac{\pi}{2} \right], & |\lambda - \lambda_0| < 4\Delta\lambda \\ 0, & |\lambda - \lambda_0| > 4\Delta\lambda \end{cases} \quad (3.8a)$$

where $\Delta\lambda$ is the longitudinal grid spacing and λ_0 is the longitude at which the mountain is centered; $z_*(\phi)$ is given by

$$z_*(\phi) = \begin{cases} z_s & \phi_N > \phi > \phi_S \\ z_s \cos^2 \left| \left[\frac{\phi - \phi_N}{3\Delta\phi} \right] \frac{\pi}{2} \right|, & \phi_N + 3\Delta\phi > \phi > \phi_N \\ z_s \cos^2 \left| \left[\frac{\phi - \phi_S}{3\Delta\phi} \right] \frac{\pi}{2} \right|, & \phi_S - 3\Delta\phi < \phi < \phi_S \\ 0, & \text{elsewhere} \end{cases} \quad (3.8b)$$

where z_s is the mountain height, $\Delta\phi$ is the latitudinal grid spacing, ϕ_N is 61.75° N and ϕ_S is 31.25° N. The resulting mountain (Fig. 2) is 22.5° wide and extends from approximately 23° N to 70° N.

In some of the experiments, the terrain is initialized in the model by raising the mountain from zero to the values in (3.8) during the first 12 hours of the integrations. This technique is designed to minimize the generation of inertia-gravity waves during the initial part of the integration while the mean flow, which is analytically balanced without topography, adjusts to the presence of the mountain. Topography is incremented at each time step according to:

$$z_m(\lambda, \phi, \tau) = \begin{cases} \hat{z}_m(\lambda, \phi) \sin^2\left(\frac{\pi\tau}{24}\right), & \tau < 12 \text{ hours} \\ \hat{z}_m(\lambda, \phi), & \tau > 12 \text{ hours} \end{cases} \quad (3.9)$$

where \hat{z}_m is given by (3.8).

4. Basic Numerical Experiments

The main objective of this paper is to determine the extent to which lee cyclogenesis can be explained by superposition, rather than enhanced baroclinic instability induced by flow over a mountain. In order to isolate the effects of the mountain, experiments were carried out with and without topography. In addition, the following conditions were also varied:

1. width of the mean flow jet
2. initial disturbance amplitude
3. mountain height
4. length of mountain range.

The experimental procedure and a summary of the results are given in this section. A detailed comparison among the solutions is carried out in Section 5.

The numerical experiments were performed using the version of the UCLA model described in Section 2. Each experiment consisted of two integrations: a Control run, and an Interactive run. In the Control run, an initially weak disturbance was allowed to evolve into a mature cyclone over flat terrain. The time dependent solution for this run may be represented as

$$\psi_c(\tau) = \psi_F + \psi'_c(\tau) \quad (4.1)$$

where ψ_F represents the zonally symmetric, time independent westerly current described by (3.1) - (3.5), and $\psi'_c(0)$ is the weak barotropic disturbance given by (3.7). $\psi'_c(t)$ is the

instantaneous deviation of the total solution from the analytically balanced state. It is obtained at any time by subtracting the balanced state (ψ_F) from the total solution. Because the UCLA model is fully nonlinear, there are no implied constraints on the magnitude or mean value of $\psi'_C(t)$.

The interactive integration was performed in the presence of a mountain. The initial conditions for this run consisted of a baroclinic disturbance superimposed on a zonally asymmetric mean state in approximate balance with the orographic forcing. This mountain was raised to its full height during the first 12 hours of the integration according to (3.9). This procedure introduced inertia-gravity waves that were filtered out by averaging the solution from $t = 18$ to $t = 30$ h. Meridional cross sections of the resulting zonal wind field over the flat part of the terrain and over the mountain ridge are shown in Fig. 3. The zonal wind profile is quite similar to that shown in Fig. 1 for the flat terrain case. The main differences are the presence of low level easterlies in the subtropics and enhanced low level westerlies in the mountain latitudes. Both of these effects are stronger over the mountain ridge than away from the mountain.

The steadiness of this solution was tested by using it to initialize the model and integrating it for 24 hours. The resulting sea level pressure fields are shown in Fig. 4. The anticyclone was maintained over the mountain ridge throughout the integration. Also present, however, was a growing low pressure system that moves slowly down the lee slope of the mountain. Thus the mountain balanced solution cannot be considered to be strictly time independent but must be represented as $\psi_M(t)$. Therefore, the Interactive solution may be written as

$$\psi_I(t) = \psi_M(t) + \psi'_I(t) \quad (4.2)$$

The model was integrated for 24 hours, beginning at $t = t_0$. $\psi_M(t_0)$ was given by the initial mountain balanced state; $\psi'_I(t_0)$ was given by $\psi'_C(t_0)$, except that the phase of $\psi'_I(t_0)$ was adjusted so that the sea level pressure trough was just upstream of the mountain ridge. $\psi'_I(t)$ was constructed from the total solution by subtraction.

Results of Control Run A (16° jet) are shown in Fig. 5. An initially weak disturbance grows into a closed circulation after about 60 h (not shown) and a mature cyclone is observed at 96 h. The growth and motion of the disturbance are indicated in Fig. 6, which shows the magnitude and longitude of the surface low deviation disturbance vs time. The center of the low pressure system was defined to be the location of the maximum geostrophic vorticity along the trough line. The disturbance moved eastward at a constant speed of about 18° /day. Its magnitude increased roughly exponentially as predicted by linear theory with a doubling time of about 14 hours.

The results of Control Run B (the 8° jet) were similar, but the growth and speed in this case were slightly slower, with a disturbance doubling time of 24 h and phase speed of 14° /day (Fig. 7). Even though both jets had the same maximum speed, the broader 16° jet had more available potential energy (because of the larger temperature variance). Also, the stronger barotropic effects in the 8° jet may reduce the baroclinic growth rate, as has been shown by Grotjahn (1979).

Several experiments were performed to investigate the effects of mountains on the growth of the disturbances observed in the two Control runs. In Experiment I, the effect of the 1.5 km mountain on disturbance growth in the presence of the 16° jet was considered. Four integrations were carried out, in which the initial disturbance fields were taken from the Control run at $t_0 = 24, 36, 48,$ and 60 h, respectively. Thus the interaction of the mountain with both small and finite amplitude disturbances was examined.

The overall growth of the surface low pressure system with and without mountains is shown in Fig. 8. The sea level pressure of the disturbance for the Control run and for the Interaction runs with $t_0 = 24$ h and $t_0 = 60$ h are compared. Also shown are the longitudes of the low pressure centers. The initial magnitudes of the two systems do not match exactly because only the deviation fields were the same. They were superimposed on different background states (i.e., $\psi_F \neq \psi_M$). The initial location of the disturbance was always adjusted to be 15° west of the ridge. Evidence of lee cyclogenesis is clearly seen in this figure. Particularly for the small amplitude case, the disturbance filled as it approached the mountain ridge. In both cases, the central pressure of the disturbance fell rapidly upon reaching the lee slope of the mountain. For example, at 33 h the Interactive disturbance was located very near the ridge line. Its central pressure fell by 14 mb as it moved down the lee slope during the next 12 h. Over the same time period, there was no net change in disturbance central pressure in the Control run. Similar enhanced growth is seen in the finite amplitude case. Furthermore, the rate of eastward movement of the low pressure center was almost three times greater while it was within about 500 km of the mountain ridge than when it was over flat terrain.

In Part I it was suggested that lee cyclogenesis such as that shown in Fig. 8 was largely due to the superposition of a growing baroclinic wave on a mountain forced flow, rather than enhanced instability of the flow in the presence of mountains. In order to test this idea using the numerical model results, the development of the deviation pressure fields (ψ'_C and ψ'_I) are compared in Fig. 9. If the enhanced development seen in Fig. 8 were due solely to the effects of superposition, these two systems would be identical. This is not the case although the difference between the two systems is small. The growth rate for ψ'_I was only slightly greater than that for ψ'_C , as seen from the slopes of the solid lines. Of the 14 mb difference in the growth in the small amplitude disturbance between 33 and 45 h,

only 1.8 mb was due to enhanced growth of the deviation field. The remaining 91% of the apparent enhanced growth was due to superposition. The average disturbance phase speed over 24 h was slightly greater with mountains than without for the small amplitude case. However, the phase speed for ψ'_1 was about 2.5 times greater than that for ψ'_C as the disturbance neared the ridge, and it remained nearly motionless for 6 to 10 h on the lee slope before moving eastward again.

For the finite amplitude case, the effects of mountain interaction were more evident. Over the full 24 h integration, enhanced growth of the deviation field accounted for 40% of the total enhanced growth in the presence of the mountain. During the period of most intense growth (72-84 h), the deviation growth accounted for 65% of the total. The eastward movement of the disturbance was very similar to that of the small amplitude case.

These results suggest that the effect of the mountain on the stability of the mean flow, while detectable, was not critical to the occurrence of lee cyclogenesis in this case. Even for the finite amplitude case, lee cyclogenesis did not require the enhanced growth of ψ'_M compared to ψ'_C , although this was certainly a significant contribution to the overall result. The growth of ψ'_M with respect to ψ'_C , and its enhanced phase speed while crossing the mountain, are consistent with the semi-geostrophic theory presented in Part I. This effect will be discussed in Section 5.

In additional experiments, the height and meridional extent of the mountain range were varied as was the initial amplitude of the disturbance for each jet profile. The results are summarized in Table 1, which gives the average doubling time and eastward phase speed for ψ'_1 (ψ'_C for the Control runs) in each case. Also shown is the apparent enhanced growth of ψ'_M compared to ψ'_C during the 12 h period immediately following passage of the disturbance over the ridge, and the percentage of this growth which was actually due to enhanced growth of ψ'_1 .

It is apparent that the central disturbance pressure fell significantly more rapidly after crossing the ridge than during the corresponding time period of the Control run, for all cases except Va. In most cases, this was achieved through a combination of slightly enhanced instability and superposition. For the case of the broad jet (Experiments I and II) the average doubling time for ψ'_1 was always less than that for ψ'_C . The case for which enhanced instability in the lee of the mountains was most significant was Experiment Id, a finite amplitude initial perturbation in the presence of low mountains. This is not surprising, since nonlinear effects may be expected to be larger for the finite amplitude disturbance, while the mountain forced ridge, and therefore the importance of superposition, is weaker for the lower mountain.

Experiments III and IV were the same as I and II, except that they used the narrow jet (Control Run B). Each case had a longer doubling time than the corresponding cases of

Experiments I and II. This was due to the smaller amount of available potential energy in the jet. Otherwise the results of these experiments were consistent with those of the broader jet, except for Experiment IIIa. This was the case of a small amplitude disturbance moving over a low mountain. While the low pressure system developed more rapidly in the presence of the mountain, this was due solely to the superposition effect. Interaction between the mountain and the flow led to stabilization of the disturbance. This feature will be discussed further in the following section.

The final pair of experiments, Va and Vb, tested the effect of mountain length on the growth of a disturbance. In Experiment Va, the flat part of the mountain ridge extended only 25° latitude, while in Vb its extent was 57° . These mountains are shown in Fig. 4.2. Based on the results of Walker (1982), it may be anticipated that less development will take place in the presence of a shorter mountain ridge. Indeed, the doubling time for Va was longer than that for any other case using the broad jet, including the Control run. On the other hand, the doubling time for Vb is comparable to that of the other experiments. As in the other experiments, the difference between the control and Interactive disturbances could be explained largely by superposition, with about a 20% effect due to interaction.

5. Interactive Effects

The results presented in the previous section indicate that (for the parameter range investigated) enhanced instability of the zonal flow due to interaction with the mountain ridge is not required to produce lee cyclogenesis. Instead, the existence of lee cyclogenesis can be predicted by the application of the simple superposition mechanism suggested in Part I.

However, the same results indicate that, at least for some cases, interactive effects significantly modify the features of the lee cyclone. In this section, the impact of the interaction on the development of the cyclone is examined more closely. Particular attention is paid to the track of the cyclone and to the formation of secondary low pressure centers.

A detailed view of the deviation field ψ'_C and ψ'_I for the Control and Interactive runs of Experiment Ia is given by Fig. 11. The first nine panels show surface pressure deviations for the Control and Interactive runs at three hour intervals. The final panel shows tracks of the low pressure centers for the two runs.

This was the case of the small amplitude initial perturbation on the broad jet, moving over the 1.5 km mountain. Of all the cases, this one is the most nearly linear, and interactive effects were similar to those of superposition. That is, the center of the disturbance was about 50% deeper for ψ'_I than for ψ'_C ; the eastward phase speed of the disturbance slowed down as it approached the mountain and then moved rapidly to the lee

side. Closer inspection shows some effects that are strictly due to interaction. While ψ'_C remains more or less symmetric about a north-south line through the center of the low, ψ'_I develops distinct asymmetries. By hour 30 (6 hours into the integration), there was evidence of a split in the center of the low with one part drifting northward along the upwind slope of the ridge, while another formed in the lee of the ridge near the initial latitude of the disturbance. The latter branch became the dominant low by hour 33. The mechanism for this behavior was discussed in the introduction, and the tracks are similar to those found by Buzzi et al. (1987) even though they used a linearized two layer model. Also, the pressure gradient to the east of the disturbance center was significantly greater than that to the west as the disturbance moved down the lee slope. The average phase speed of ψ'_I was slightly greater than that of ψ'_C as seen from the final positions of the two disturbances.

According to Table 1, the largest interactive effects were seen in Experiment Id, which was the same as Ia except that it had a larger amplitude initial disturbance. Details of this experiment are shown in Fig. 12. Here, the track of the deviation low pressure system is clearly modified in the Interaction case. The system moves northward about 5° as it progresses slowly up the windward slope. This effect is more pronounced for this disturbance than it was for the weaker disturbance in experiment Ia. At hour 69 ($t_0 + 9$) the first indication of a lee trough and tightening of the pressure gradient to the east of the low appeared. This lee trough continued to develop, and by hour 75 ($t_0 + 15$) a closed low, with particularly sharp pressure gradients on its southeast flank had formed on the eastern slope of the ridge. During the six hour period following passage over the ridge line (hours 72-78) the magnitude of the interactive disturbance doubled, from 8 to 16 mb. During the same time period the magnitude of the control disturbance increased by only 40%, from 10 to 14 mb. These results indicate that while the total field exhibits enhanced growth regardless of the amplitude of the initial disturbance, the growth is more significant and only for large amplitude initial disturbances. This is similar to the result reported by Trevisan (1976).

The effect of mountain height on the development of ψ'_I is shown in Fig. 13 which compares Experiment IIa to the Control Run. Comparison with Fig. 11 shows very little difference in overall growth of the disturbance. The magnitude of the low pressure center in the high mountain case was just slightly lower than that for the low mountain case at hour 48, and its position was about 2° to the east. Despite these overall similarities, however, the details of the development show a number of significant differences. In the 3 km mountain case, there was evidence of lee trough formation after only three hours of integration ($t = 27$). Three hours later, there were two closed pressure systems, one almost stationary in the lee of the mountain, and the other moving northward and slowly

eastward along the upwind mountain slope. At hour 36, a weak trough formed near the ridge line at about 40 N. This feature remained approximately stationary throughout the rest of the integration and became a closed low at hour 45. This secondary cyclone was not seen at all in the Control run and was present as an extremely weak feature for the 1.5 km mountain. It was also observed by Walker (1982) and will be discussed further in relation to Experiment V.

The case of the small disturbance on a narrow jet passing over a low mountain was unique in that while superposition of the disturbance and the mountain forced solution led to apparent deepening in the lee of the mountain, interactive effects actually stabilized the growing wave. This is shown in Fig. 14. From the time the wave passed over the mountain ridge ($t \approx 39$) until the end of the integration at $t = 48$, the disturbance in the interactive run deepened by 0.7 mb. Thus, for this case, the "lee cyclogenesis" indicated by Table 1 was due entirely to superposition effects.

By reducing the latitudinal extent of the mountain ridge, the behavior of the disturbance was changed considerably. This was the only case for which no enhanced growth was observed. Examination of Fig. 15 shows that the lack of growth was due to a combination of factors. The track of the main disturbance took it well to the north of the ridge. Only the southern extension of the original trough actually passed over the ridge. As the disturbance moved around the northern slope of the mountain, its center deepened compared to that of the Control disturbance. By hour 54, a lee trough had formed. This trough continued to develop, maintaining a magnitude equal to or greater than that of the Control disturbance. However, it moved rather quickly toward the east, so that it did not remain in phase with the mountain forced lee trough, and therefore did not produce the overall growth seen in the other cases.

The final case to be considered is that of the long mountain ridge shown in Fig. 10. This case was very similar to IIb, as may be seen by comparing Figs. 13 and 16. In both cases ψ'_1 moved northward as it approached the mountain, and a trough developed in the lee of the ridge and grew to a slightly greater intensity than did the Control disturbance. The principal difference was that the disturbance center was forced to move over the northern part of the longer ridge, rather than around it.

6. Summary and Conclusions

In Part I we investigated lee cyclogenesis associated with a baroclinic current flowing over an infinitely long mountain range. Quasi-geostrophic and semi-geostrophic solutions were obtained that documented that lee cyclogenesis could occur as a result of the superposition of a moving disturbance upon a steady state mountain forced solution. However, none of the disturbances showed enhanced growth due to the interaction with

the topography, although the semi-geostrophic solutions experienced distortion and phase speed changes as they passed over the topography. In Part I the basic current and the disturbances had no variation along the mountain ridge.

In this paper we have removed some of the restriction that were present in Part I. A primitive equation model was used in place of the quasi- and semi-geostrophic models, and the basic flow and the disturbances were allowed to vary with latitude. In addition the mountain range, which was oriented north-south, had a finite length. The small amplitude, sinusoidal initial disturbance grew exponentially because the basic current was baroclinically unstable. A control perturbation field was obtained by subtracting the initial zonally averaged field from the control solution at various times. The interactive solutions were initialized by adding a perturbation control solution to the mountain forced solution.

The mountain forced solution was obtained by first integrating the model from an initial state that was independent of longitude as the mountain was raised from zero to its full height in 12 hours. Then the integration was continued, and the average from $t = 18$ hours to $t = 30$ hours was taken to be the mountain mean state. When the model was integrated from the mountain forced solution the field evolved slowly, which showed that the mountain-forced solution was not a steady state. Various experiments were carried out by changing the initial disturbance amplitude, the mountain height, the mountain length and half-width of the basic state jet. All of the initial disturbances were shifted so that the initial low center was 15° of longitude west of the ridge crest.

The relative importance of superposition and enhanced growth in lee cyclogenesis was determined by subtracting the time dependent mountain solution from the interactive solution and comparing the result with the perturbation control solution. The vast majority of the experiments showed that most of the lee growth could be explained by superposition. The main exception was a large amplitude initial state case in which superposition explained only 35% of the lee growth. Most of the experiments showed enhanced growth of 9-22%. However, two experiments had negative enhanced growth (that is, superposition gave a larger change than was observed).

These results show that there may be a dynamic enhancement of lee cyclogenesis of 10 to 20% that comes from the interaction between the cyclone, the topography and the mountain forced mean flow. However, there were enough uncertainties in the numerical experiments that we can not be sure that there was any dynamical enhancement in the process. One problem was that the mountain forced solution did not give a steady state. In fact a disturbance developed in the mountain only solution that could have spuriously interacted with the lee cyclone. Also, when the cyclone was added to the mountain solution, the resulting fields may not have been in balance, and this could have led to inertial-gravity wave oscillations.

Our results demonstrated that topography can affect the cyclone structure and its path. As the cyclones moved up the slope they were deflected to the north, and as they moved down the lee slope they moved back to their original latitude. This behavior was modeled by Buzzi *et al.* (1987) with a linearized, two-layer quasi-geostrophic model, and the basic mechanism was originally discussed by Newton (1956). It may be that weak Kelvin waves were excited by the interaction between the cyclone and the topography (Gill, 1977). These waves would tend to move north on the upwind slope and south on the lee slope. It was found that the interactive cyclones moved faster over the crest of the mountain than the control cyclones. This effect was also found in the semi-geostrophic solutions in Part I, and it was caused by the advection by the divergent part of the flow over the topography. The superposition process also led to a speeding up of the disturbance as it moved over the crest because the topographically forced high tended to "hold back" the low on the upwind side and "push it ahead" on the lee side.

Further research is needed to determine whether or not there is significant dynamic enhancement of lee cyclogenesis. It would be highly desirable to find a true steady-state mountain solution, which could then be analyzed directly for stability.

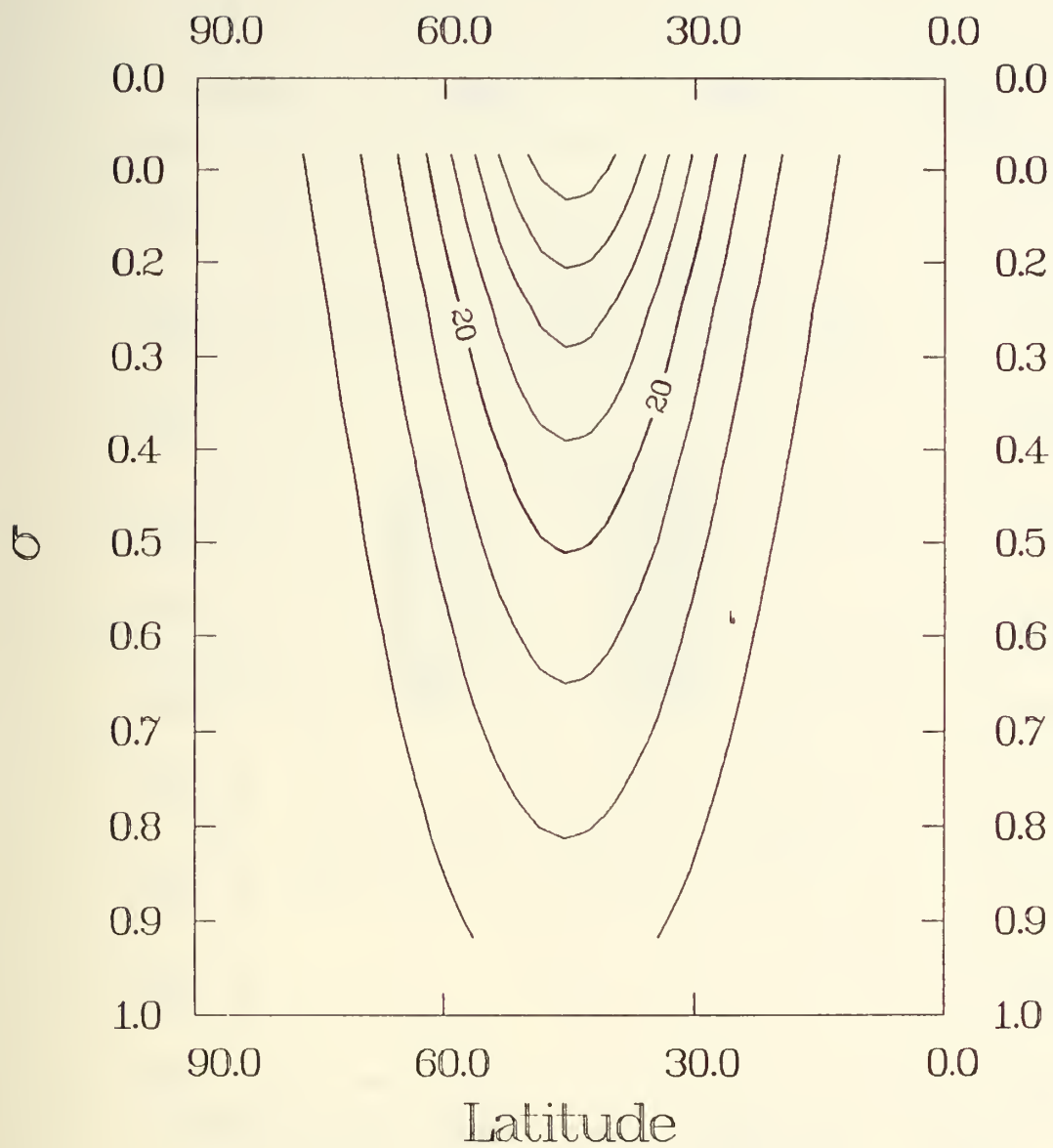
Acknowledgements:

This research was supported by the Division of Atmospheric Sciences, National Science Foundation under Grants NSF ATM 8405276 and NSF ATM 8610354. Part of the research was conducted for the Office of Naval Research and was funded by the Naval Postgraduate School. The manuscript was partially typed by Mrs. P. Jones and Ms. J. Murray, and the numerical calculations were carried out at the W. R. Church Computer Center.

References

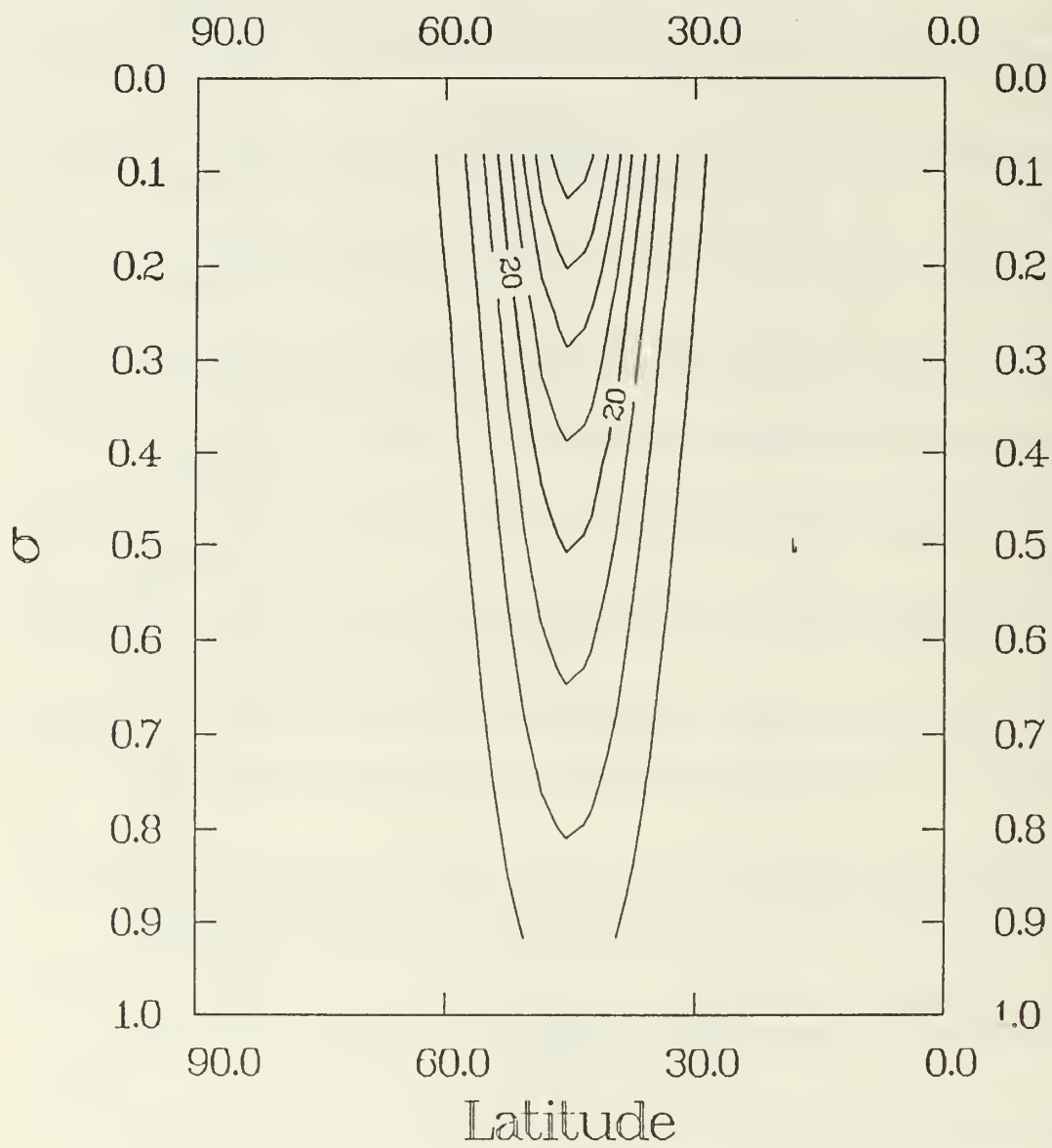
- Arawaka, A., and V. Lamb, 1977: Computational design of the basic dynamical processes of the UCLA general circulation model. *Methods in Computational Physics*, 17, 173-265, Academic Press, NY.
- _____, and _____, 1981: A potential enstrophy and energy conserving scheme for the shallow water equations. *Mon. Wea. Rev.*, 109, 18-36.
- _____, and M. Suarez, 1983: Vertical differencing of the primitive equations in sigma coordinates. *Mon. Wea. Rev.*, 111, 34-45.
- Bannon, P., 1984: A semigeostrophic model of frontogenesis over topography. *Beitr. Phys. Atmos.*, 57, 393-408.
- Buzzi, A., A. Speranza, S. Tibaldi and E. Tosi, 1987: A unified theory of orographic influence upon cyclogenesis. *Meteorol. Atmos. Phys.*, 36, 91-107.
- Charney, J. G., and P. G. Drazin, 1961: Propagation of planetary scale disturbances from the lower into the upper atmosphere. *J. Geophys. Res.*, 66, 83-109.

- Eady, E., 1949: Long waves and cyclone waves. *Tellus*, **3**, 33-53.
- Farrell, B. F., 1982: The initial growth of disturbances in a baroclinic flow. *J. Atmos. Sci.*, **39**, 1163-1686.
- _____, 1984: Modal and nonmodal baroclinic waves. *J. Atmos. Sci.*, **41**, 668-673.
- Gill, A., 1977: Coastally trapped waves in the atmosphere. *Quart. J. Roy. Met. Soc.*, **103**, 431-440.
- Grotjahn, R., 1979: Cyclone development along weak thermal fronts. *J. Atmos. Sci.*, **36**, 249-274.
- Hayes, J. L., 1985: A numerical and analytical investigation of lee cyclogenesis. Naval Postgraduate School, Doctoral Dissertaiton. 138 pp.
- _____, R. T. Williams and M. A. Rennick, 1987: Lee cyclogenesis, Part I: Analytic studies. *J. Atmos. Sci.*, **44**, 432-442.
- Hoskins, B. J. and F. Bretherton, 1972: Atmospheric frontogenesis models: Mathematical formulation and solution. *J. Atmos. Sci.*, **29**, 11-37.
- Newton, C. W., 1956: Mechanisms of circulation change during lee cyclogenesis. *J. Met.*, **13**, 528-539.
- Palmen, E., and C. W. Newton, 1969: *Atmospheric Circulation Systems*. Academic Press, 603 pp.
- Phillips, N. a., 1957: A coordinate system having some special advantages for numerical forecasting. *J. Meteor.*, **14**, 184-185.
- Smith, R. B., 1984: A theory of lee cyclogenesis. *J. Atmos. Sci.*, **41**, 1159-1168.
- _____, 1986: Further development of a theory of lee cyclogenesis. *J. Atmos. Sci.*, **43**, 1582-1602.
- Speranza, A., A. Buzzi, A. Trevisan and P. Malguzzi, 1985: A theory of lee cyclogenesis in the lee of the Alps. Part I: Modifications of baroclinic instability by localized topography. *J. Atmos. Sci.*, **42**, 1521-1535.
- Trevisan, A., 1976: Numerical experiments on the influence of topography on cyclone formation with an isentropic primitive equation model. *J. Atmos. Sci.*, **33**, 768-780.
- Walker, J. P., 1982: Numerical simulation of the influence of small scale mountain ranges on a baroclinic wave. Naval Postgraduate School Master's Thesis, 158 pp.



1 Meridional cross section of the zonal mean wind . Contour interval = 5ms⁻¹ ; 20 ms⁻¹ contour is emphasized: a) Control Run A; b) 'Control Run B.

1 a



12

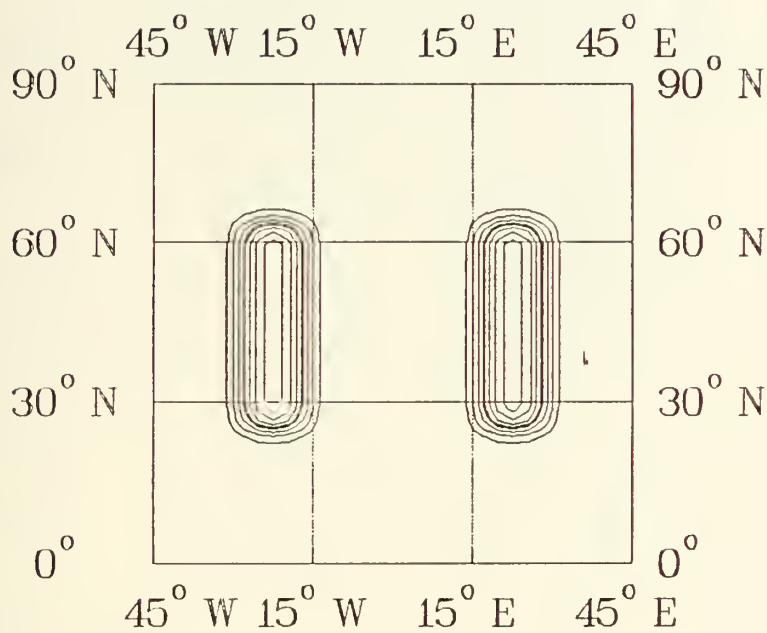
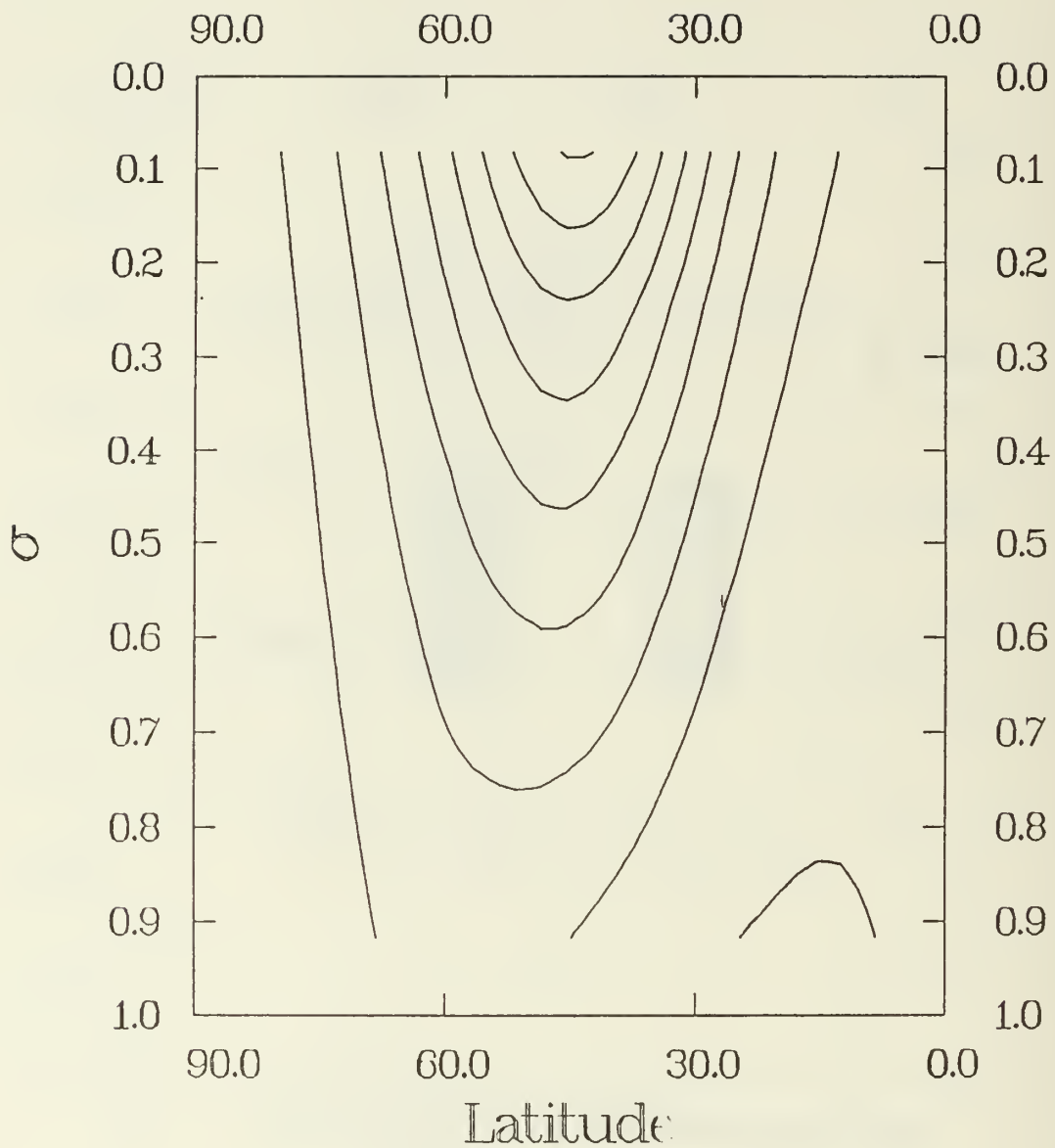
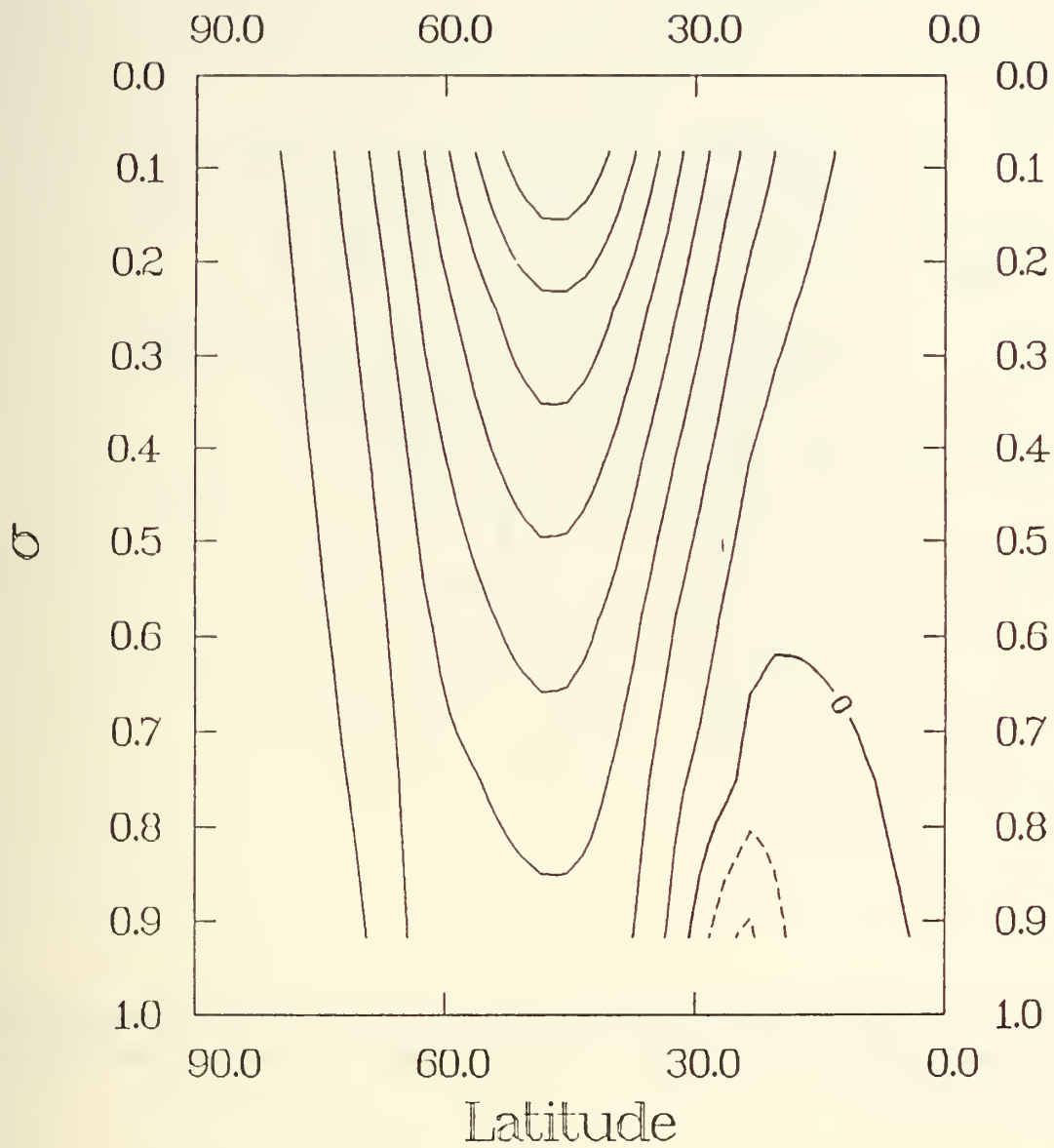


Fig. 2 Topographic surface for standard mountains.



3 Meridional cross section of the zonal wind for $\psi_M(0)$: a) away from the mountain; b) at the ridge. Contour interval = 5ms⁻¹; 0ms⁻¹ contour is emphasized. Negative values are dashed.

3 a



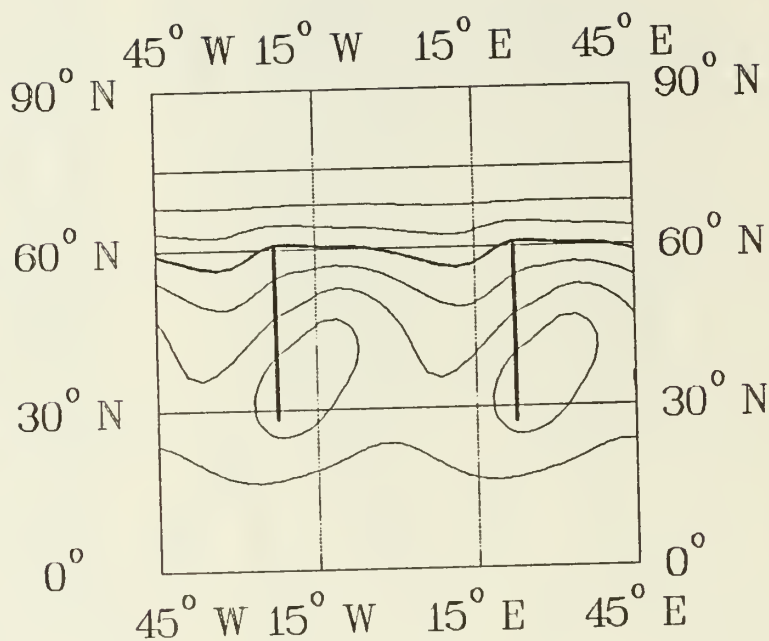
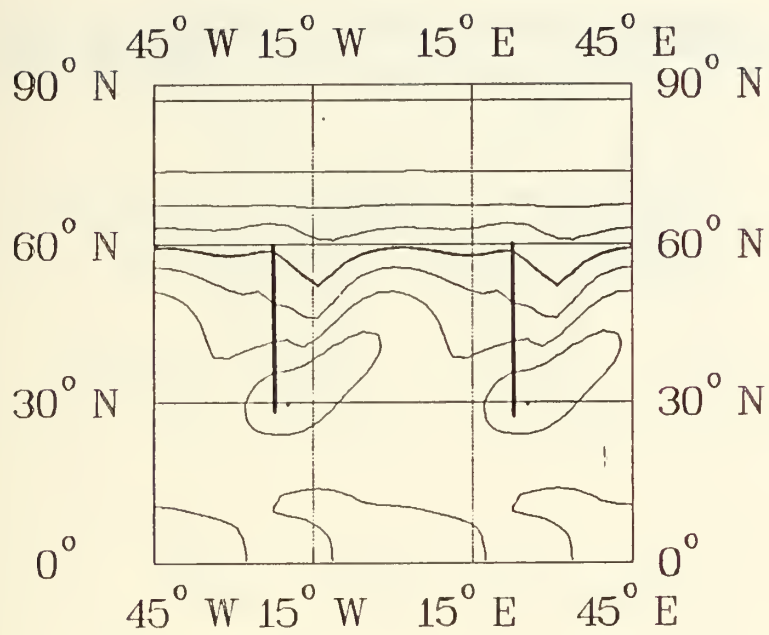
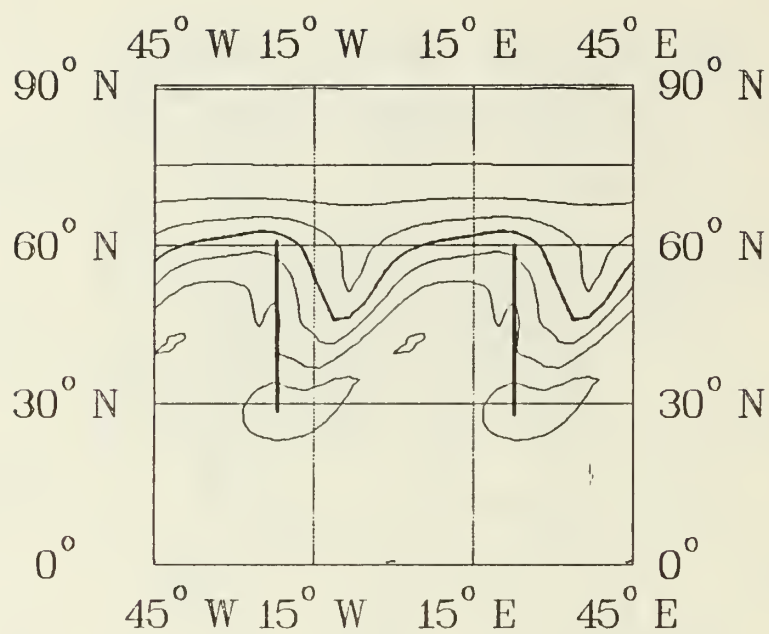


Fig. 4 Sea level pressure for $\psi_M(t)$ for standard 1.5 km mountains. Heavy vertical lines indicate the location of the mountain ridge: a) $t = 0$; b) $t = 12$ h; c) $t = 24$ h. Contour interval = 5mb; 1030 mb contour is emphasized.

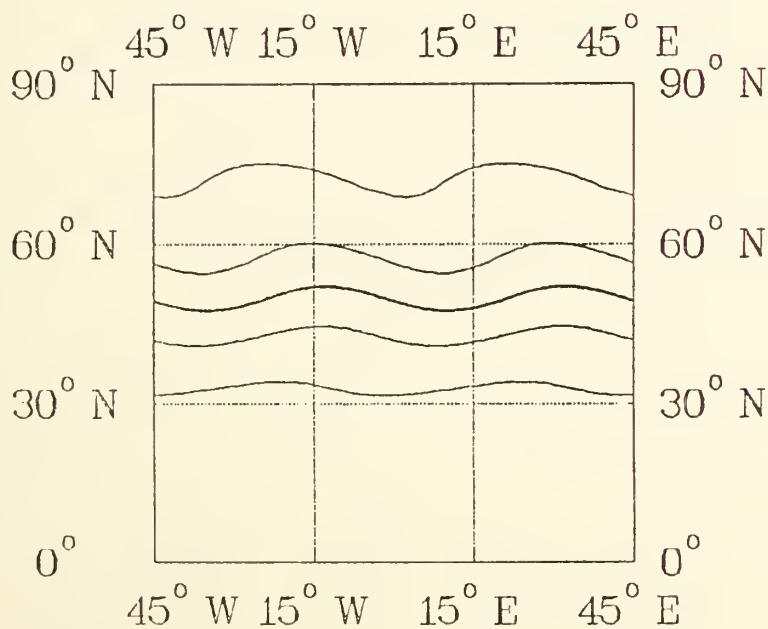
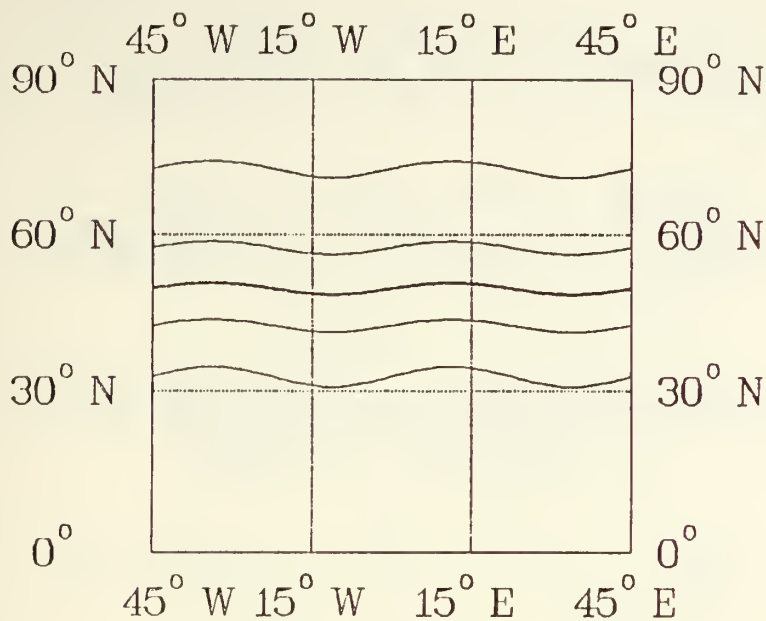
4a



4b

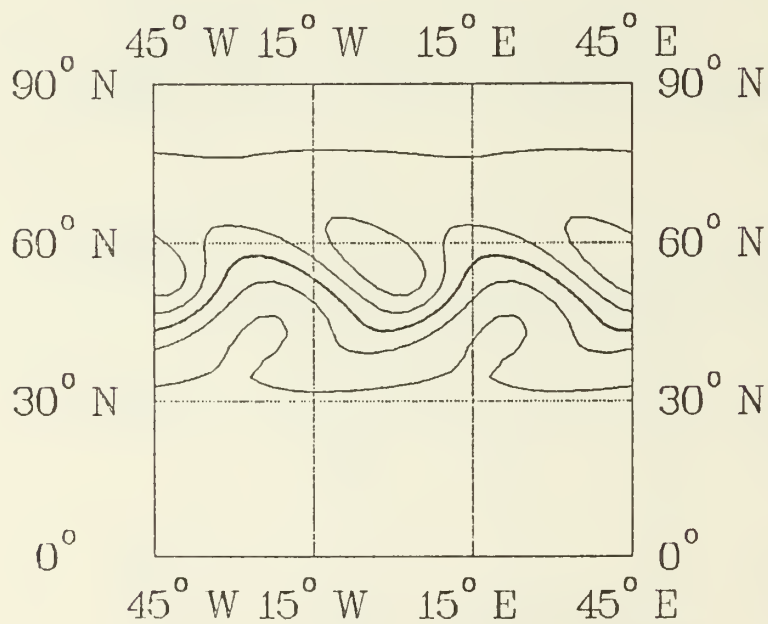
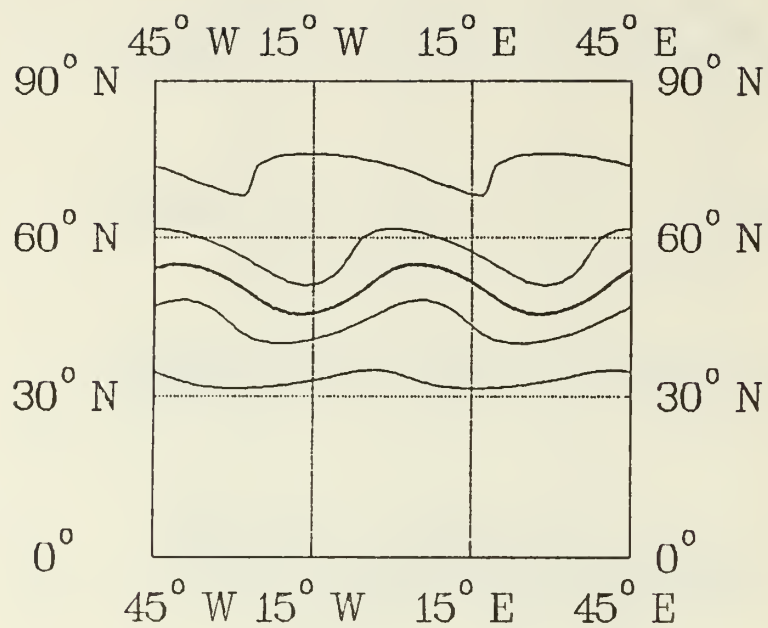


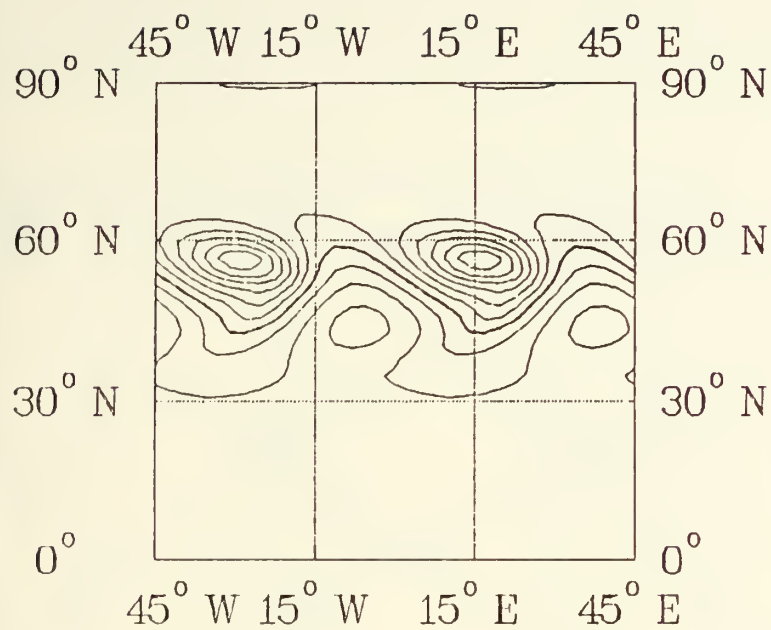
4c



a level pressure for Control run A ($\psi_c(t)$): a) $t = 0$; b) $t = 24$ h; c) $t = 48$ h; d) $t = 72$ h; e) $t =$
h. Contour interval = 5mb; 1010 mb contour is emphasized.

5 a, b





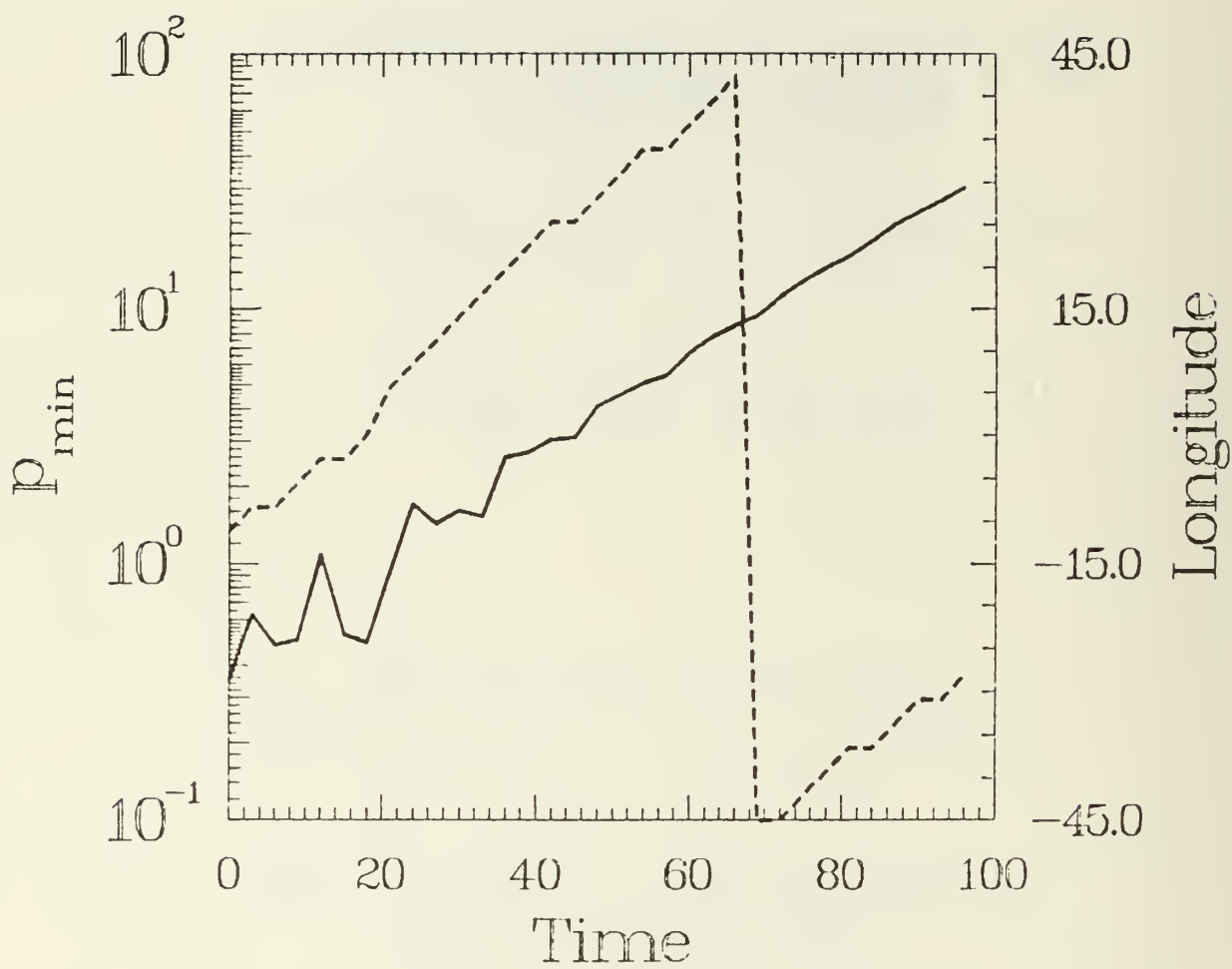


Fig. 6 Magnitude (solid line) and location (dashed line) of the minimum disturbance pressure (ψ'_c) for Control run A.

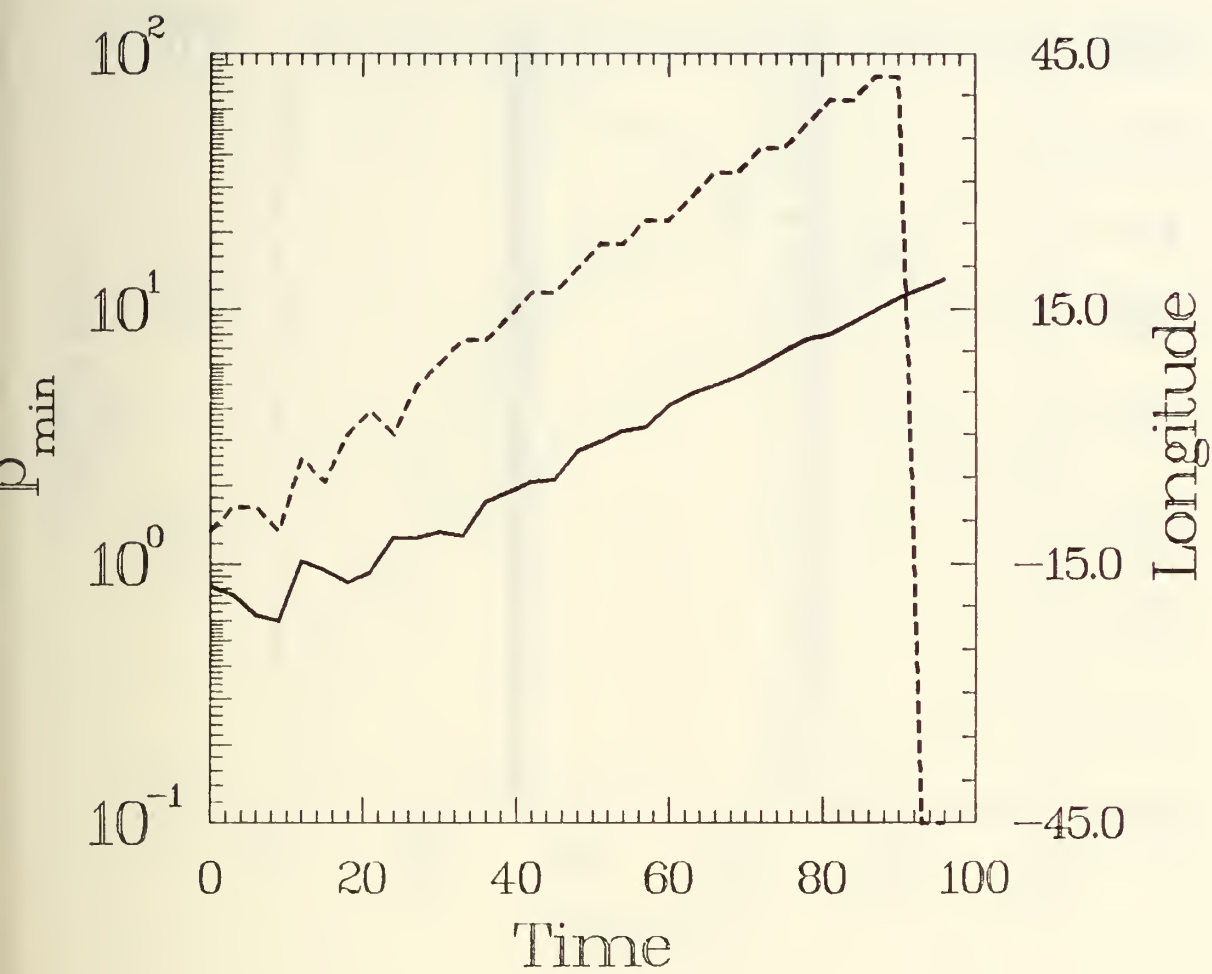


Fig. 7 As in Fig. 6, but for Control run B.

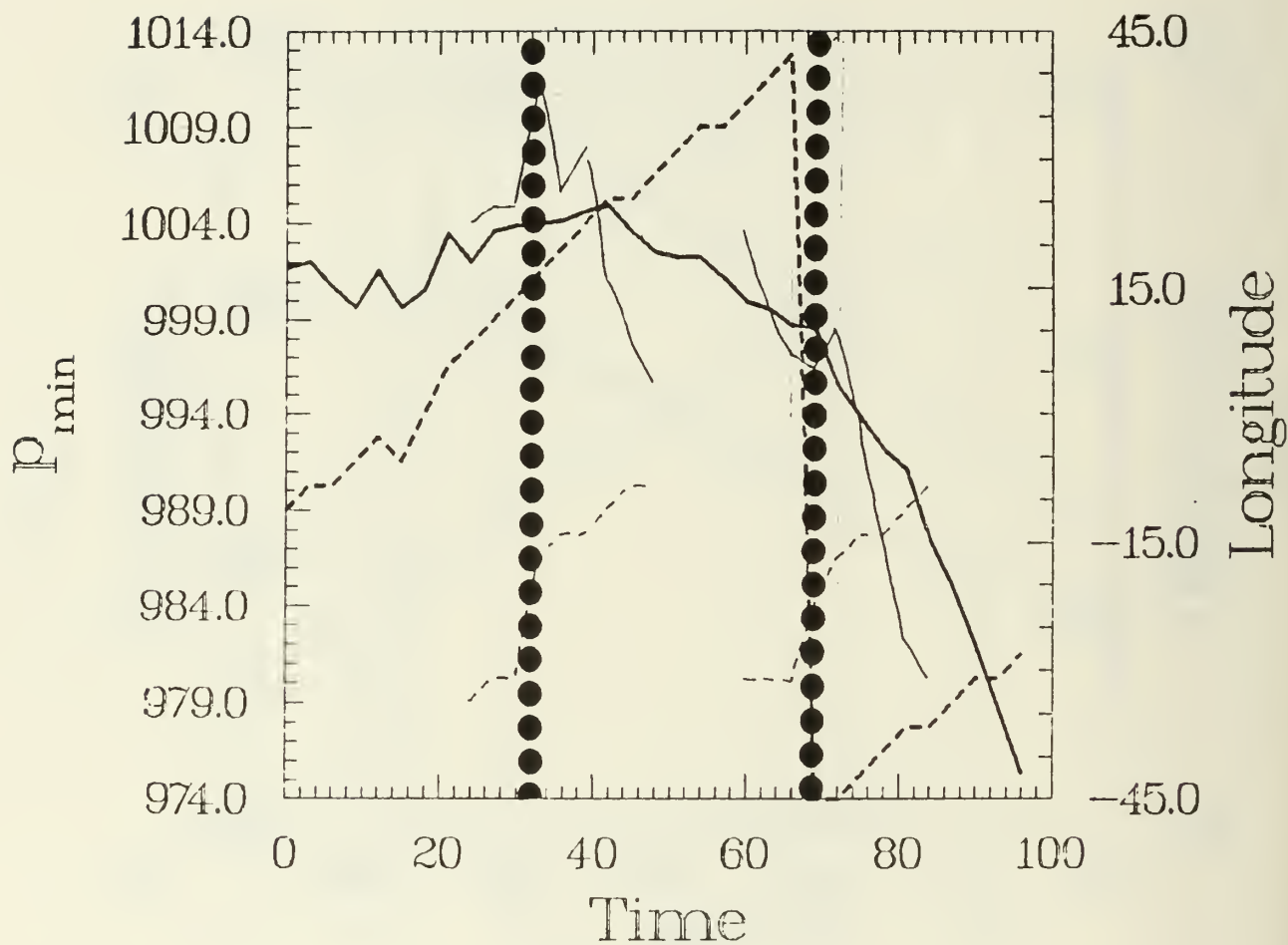


Fig. 8 Magnitude (solid lines) and location (dashed lines) of minimum sea level pressure for Control run A (heavy lines) and for Interactive run of Experiment I (thin lines). Time at which system was near the mountain ridge is indicated by heavy dotted lines.

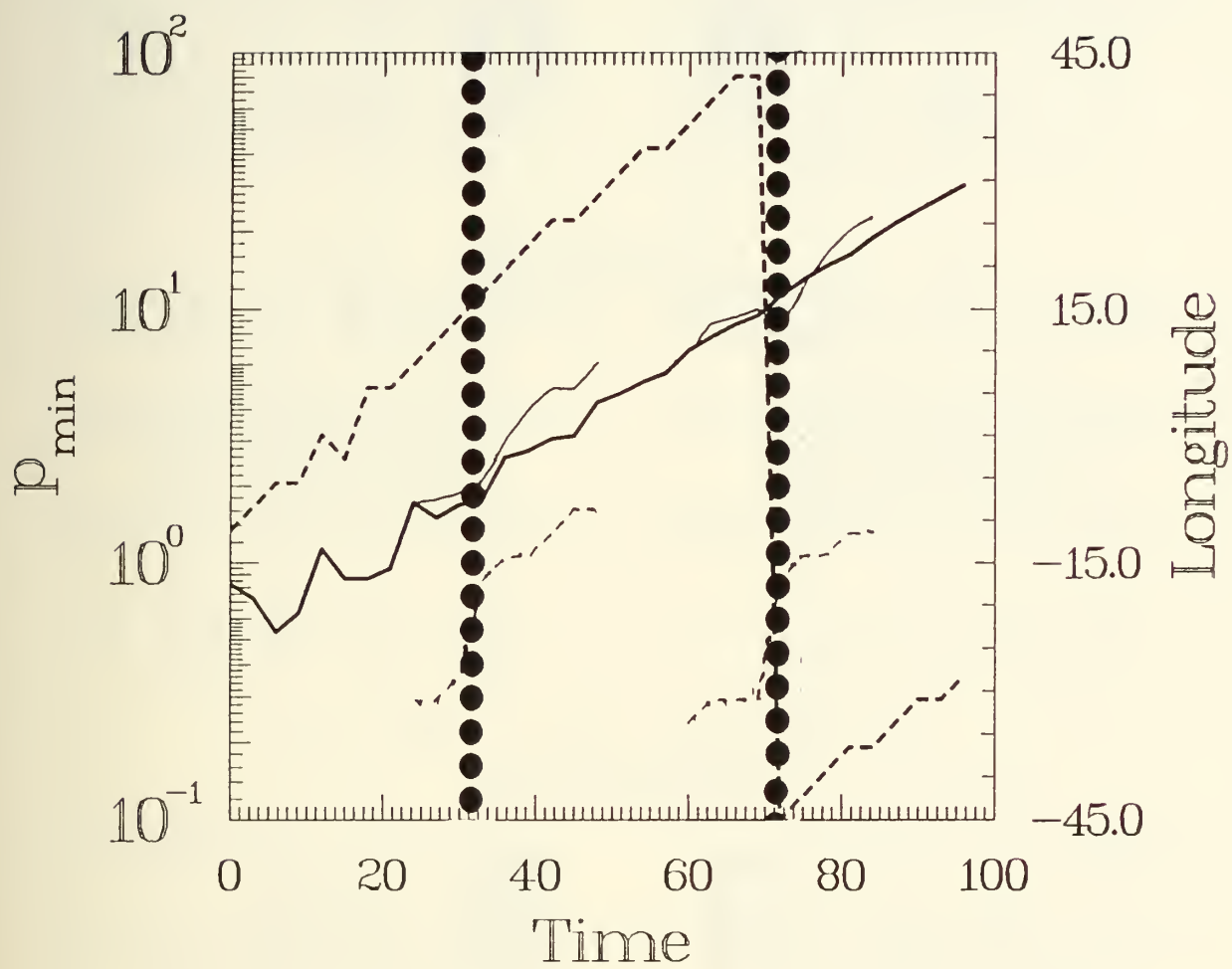


Fig. 9 As in Fig. 8, except for disturbance pressures.

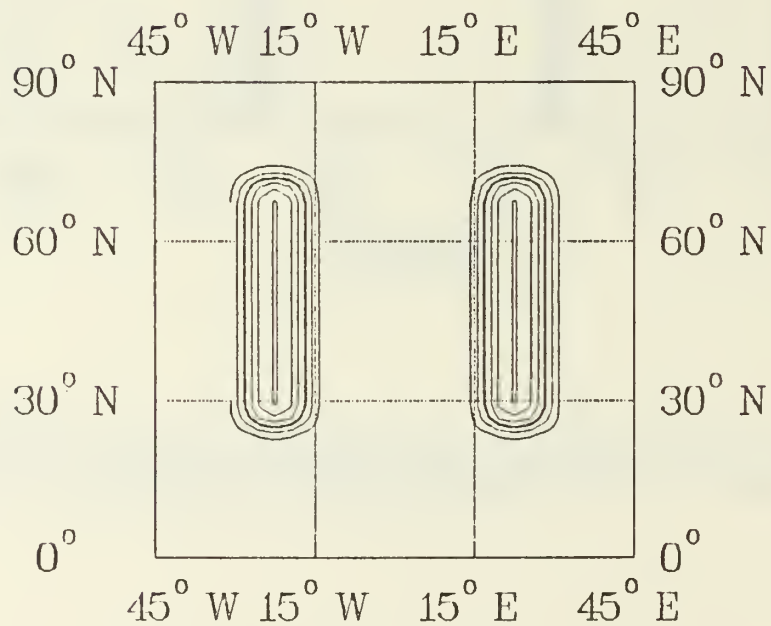
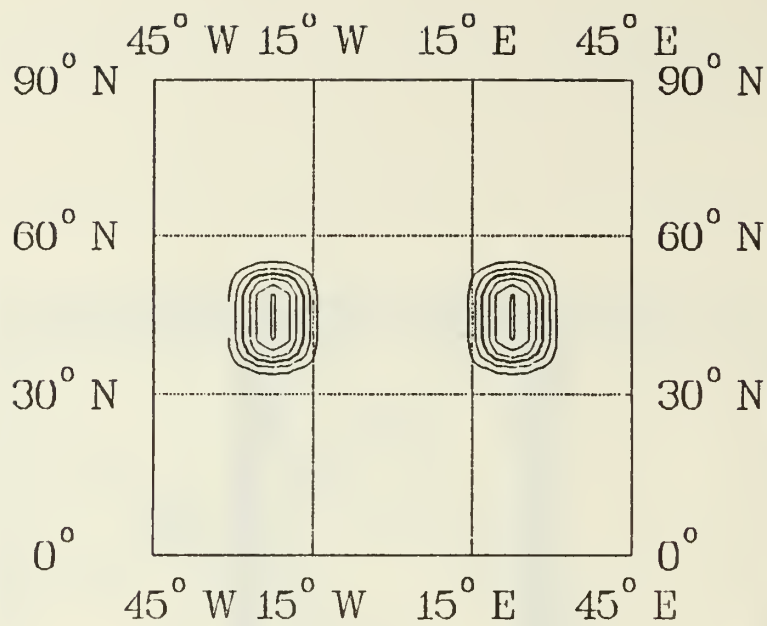
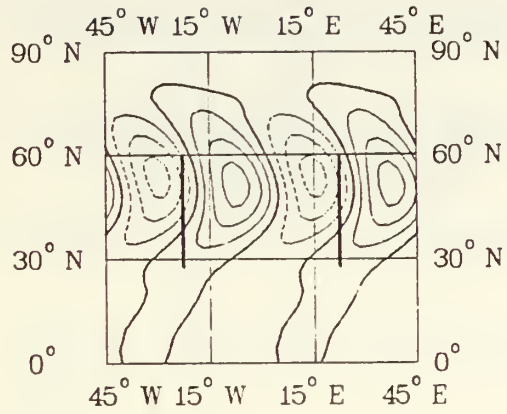
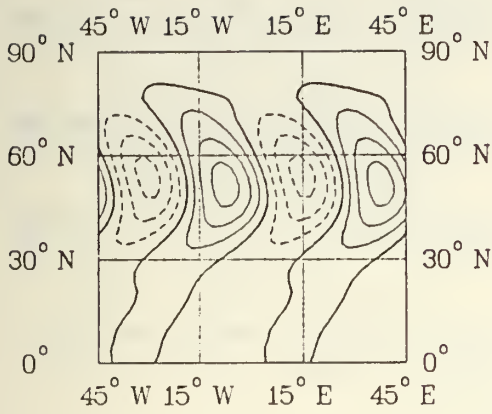
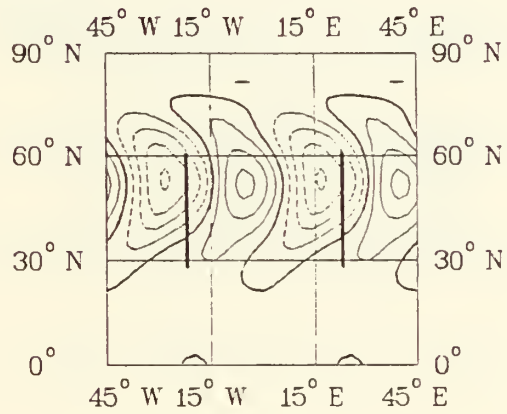
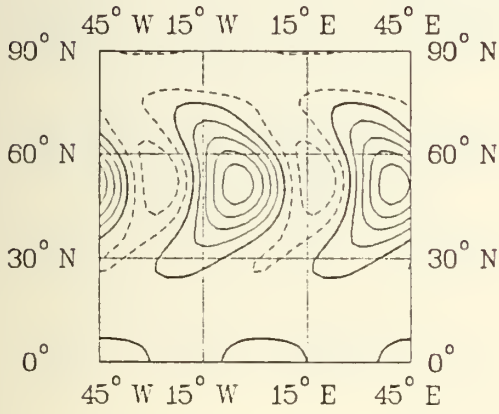


Fig. 10 Mountain topography used for Experiment V.

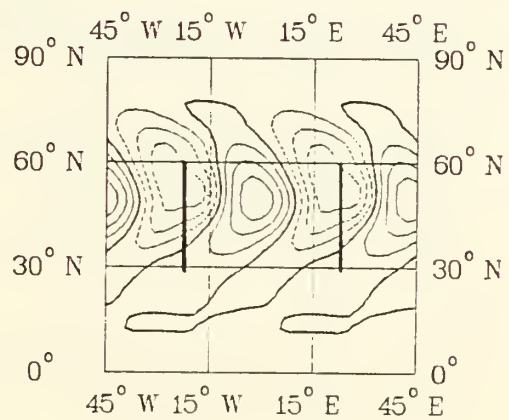
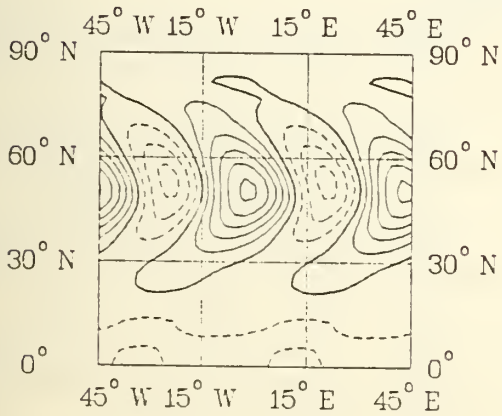
Sfc Pressure at Hour 24



Sfc Pressure at Hour 27

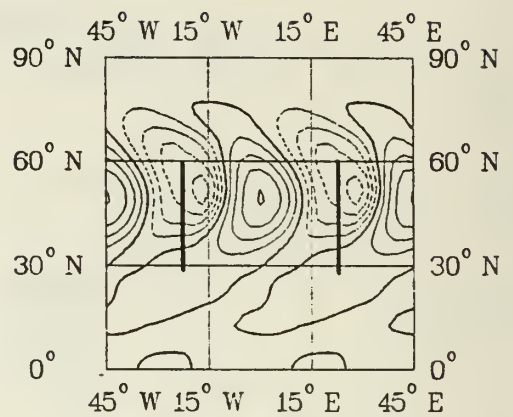
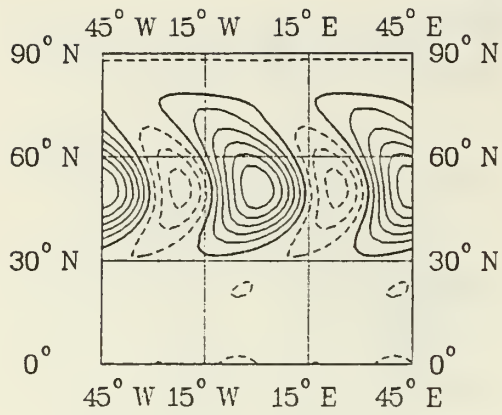


Sfc Pressure at Hour 30

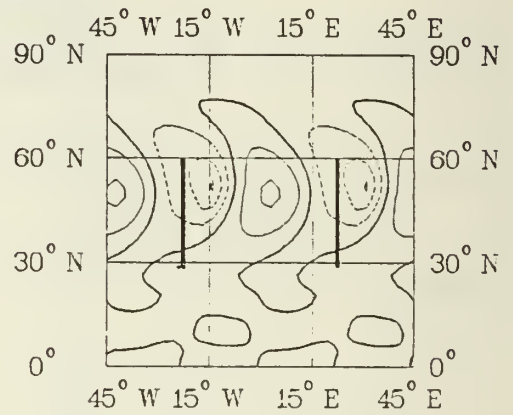
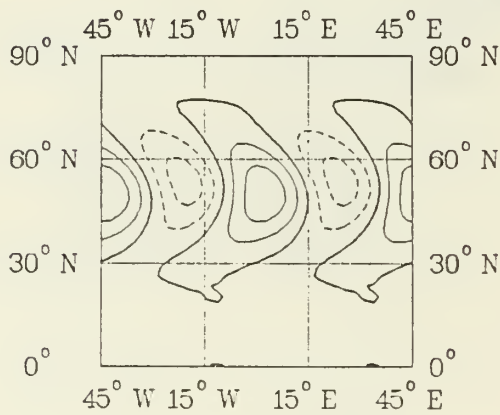


Figs. 11a, b, c

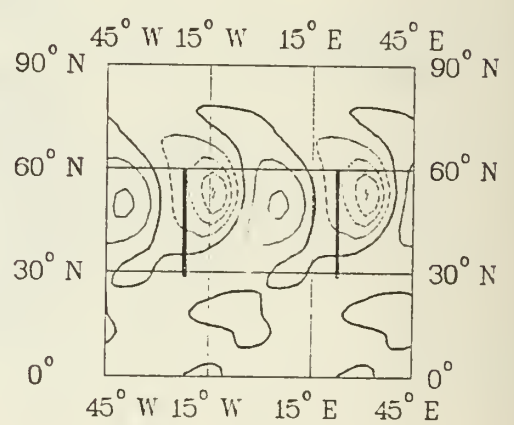
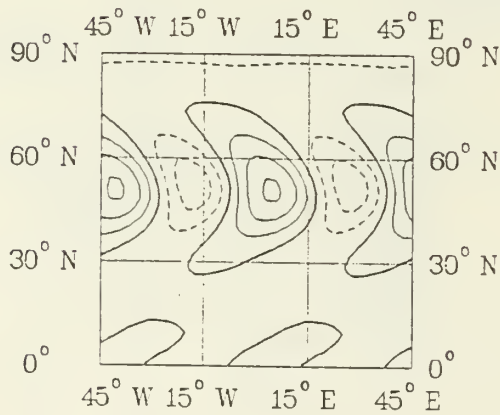
Sfc Pressure at Hour 33



Sfc Pressure at Hour 36

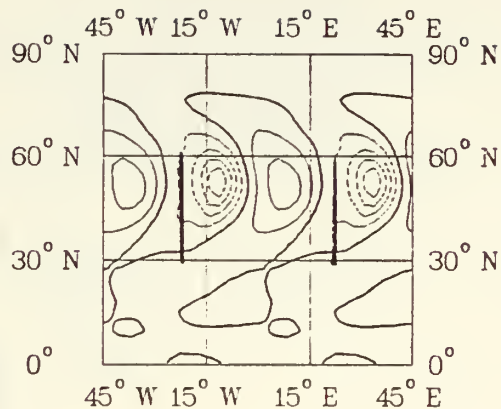
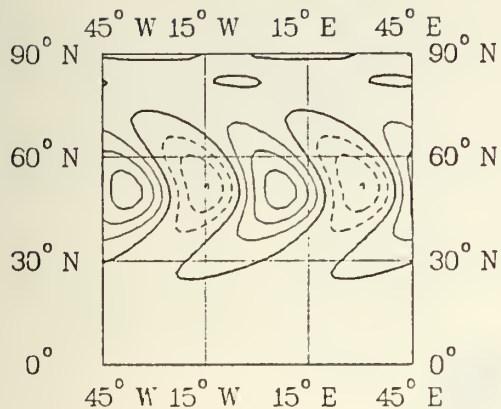


Sfc Pressure at Hour 39

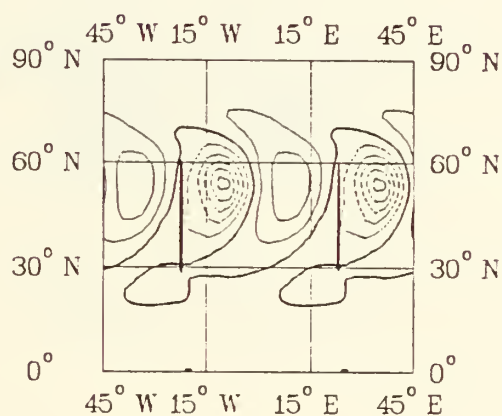
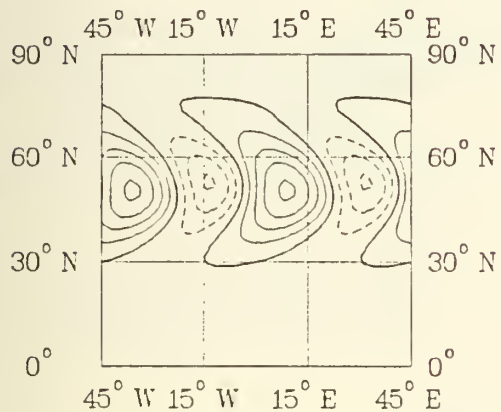


Figs. 11d, e, f

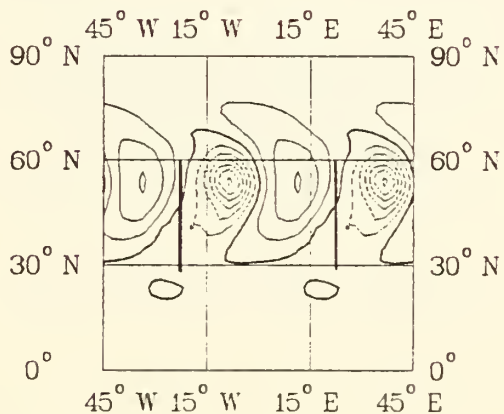
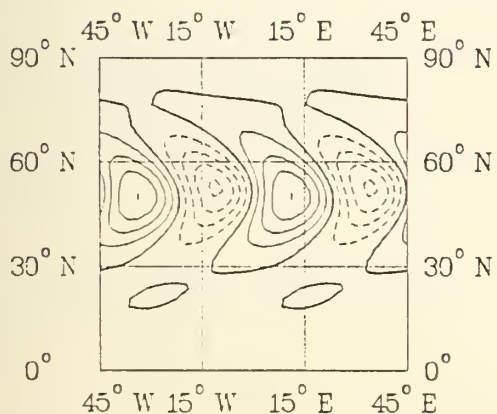
Sfc Pressure at Hour 42



Sfc Pressure at Hour 45



Sfc Pressure at Hour 48



Figs. 11g, h, i

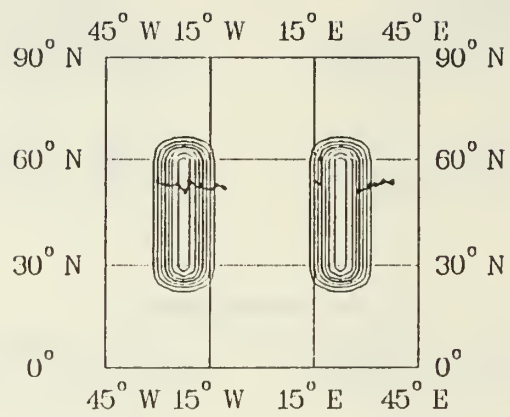
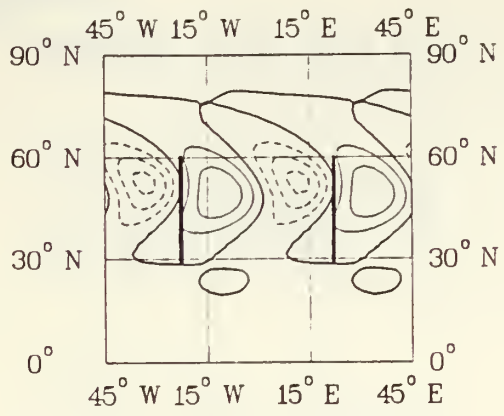
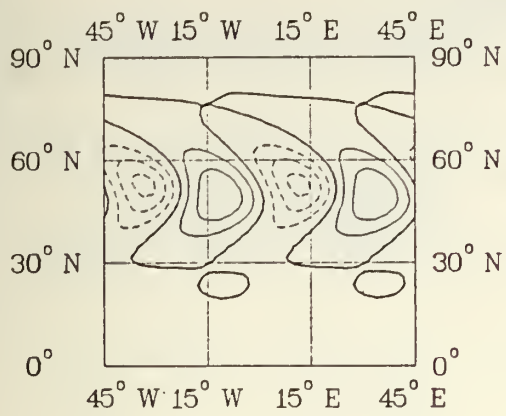
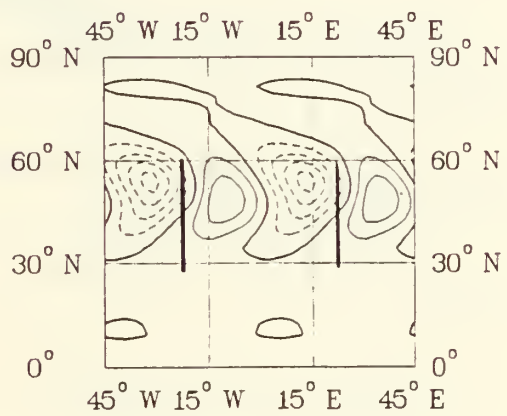
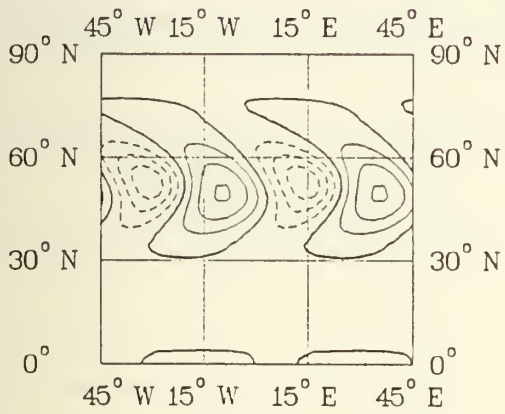


Fig. 11j

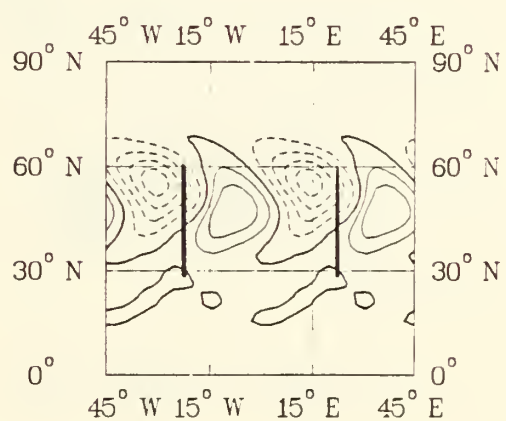
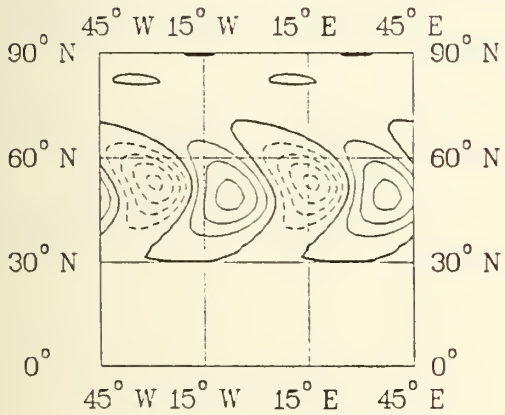
Sfc Pressure at Hour 60



Sfc Pressure at Hour 63

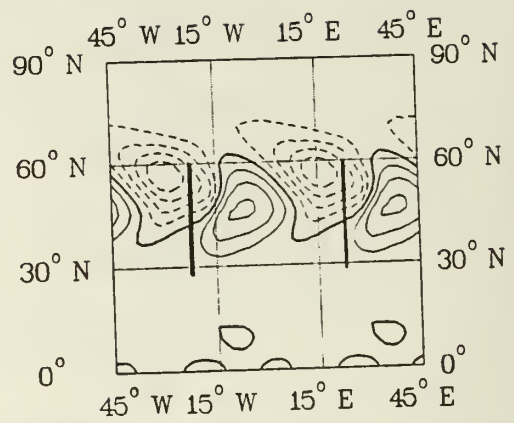
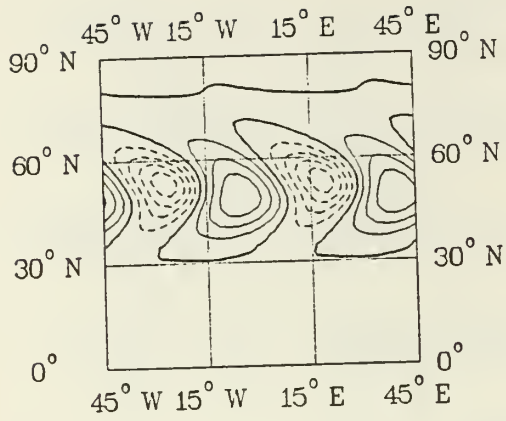


Sfc Pressure at Hour 66

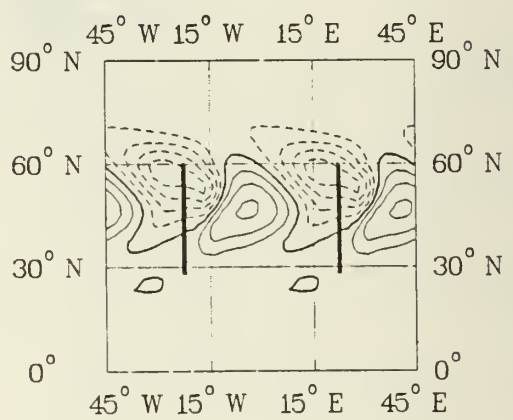
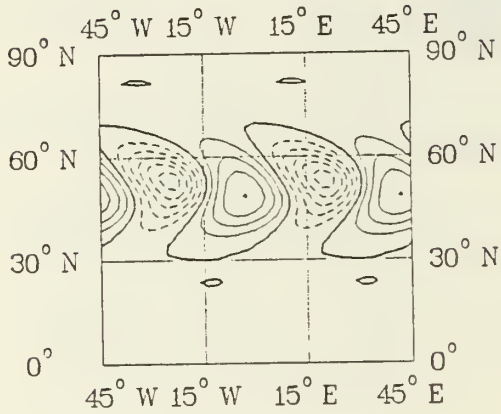


Figs. 12a, b, c

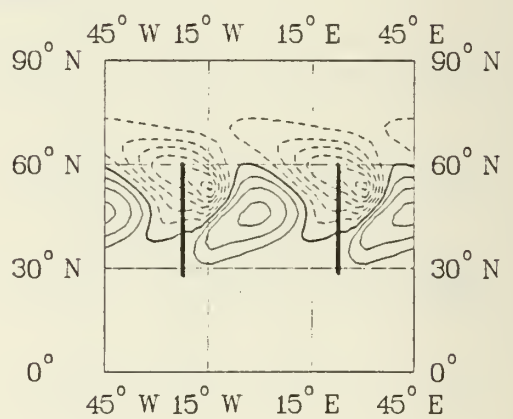
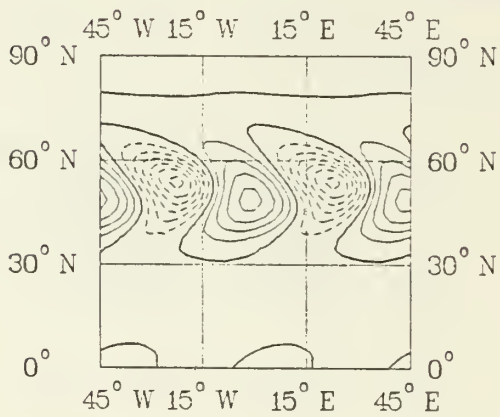
Sfc Pressure at Hour 69



Sfc Pressure at Hour 72

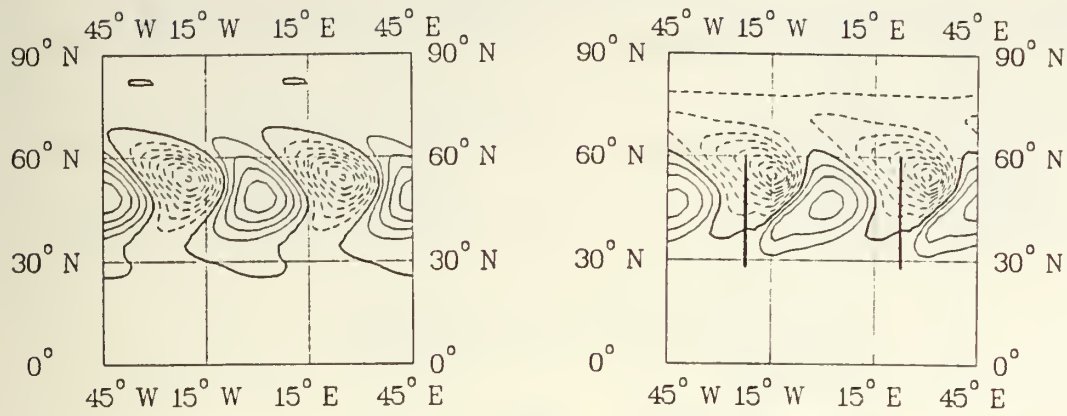


Sfc Pressure at Hour 75

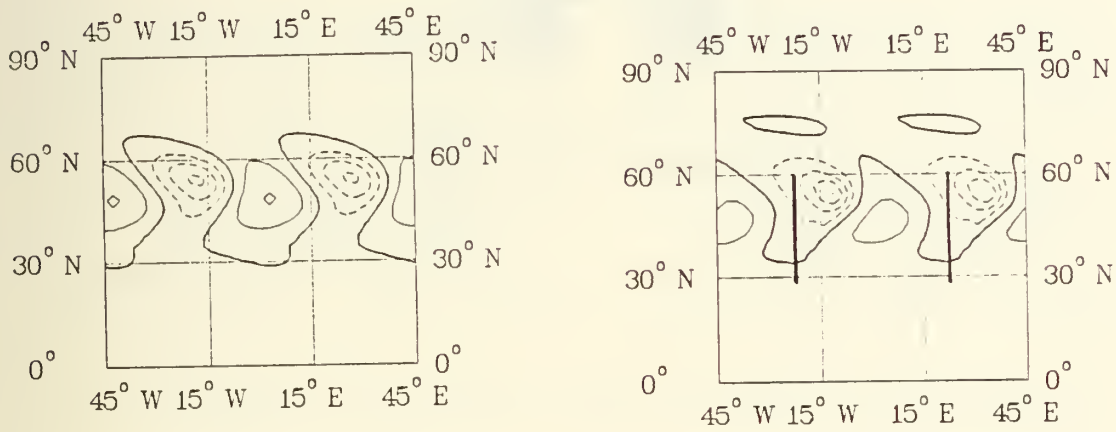


Figs. 12d, e, f

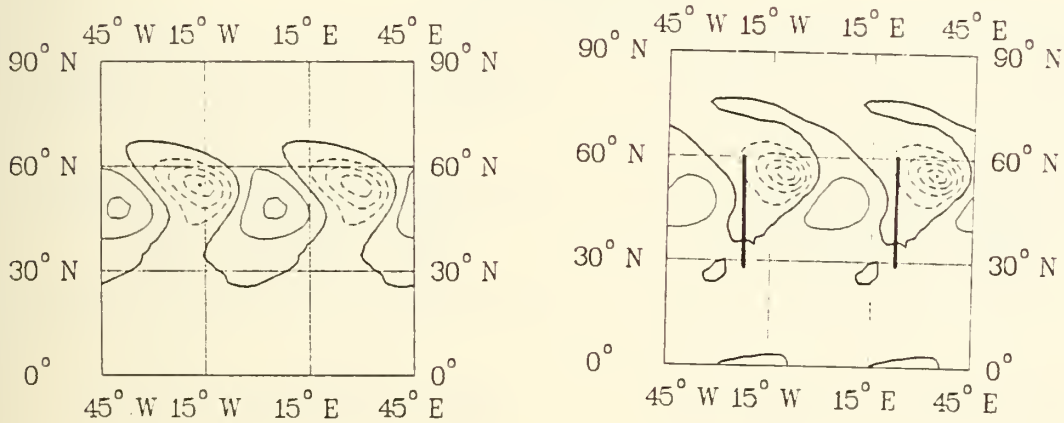
Sfc Pressure at Hour 78



Sfc Pressure at Hour 81



Sfc Pressure at Hour 84



Figs. 12g, h, i

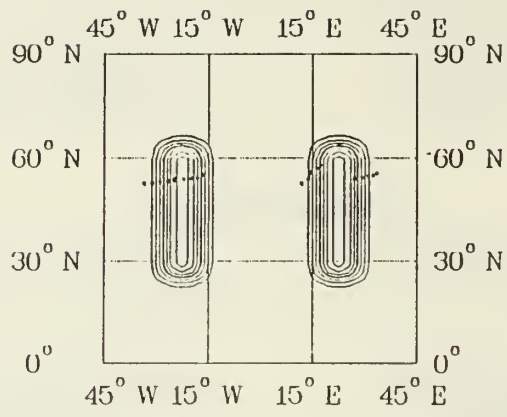
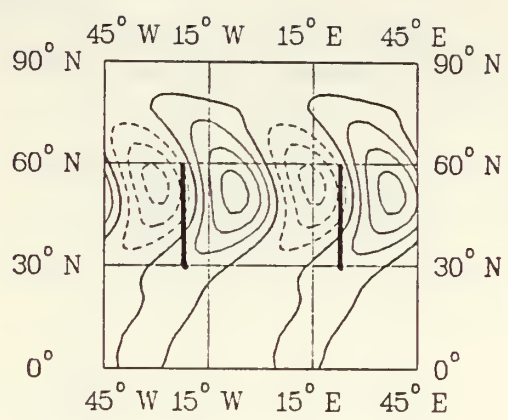
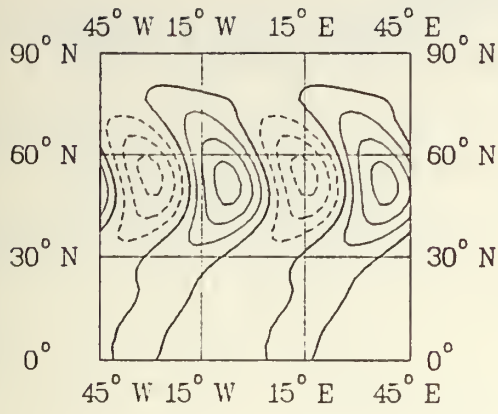
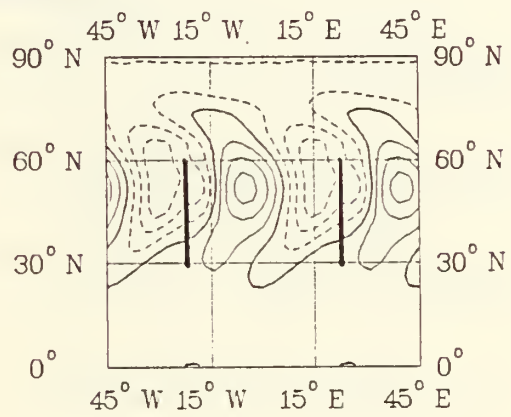
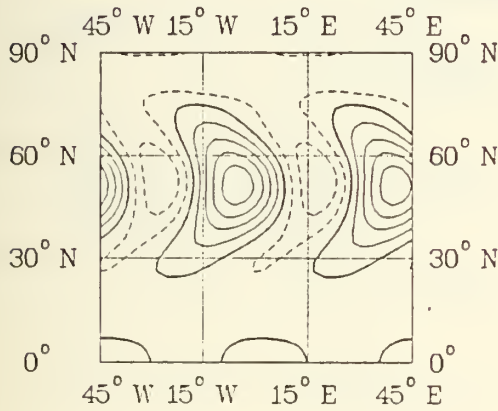


Fig.12j

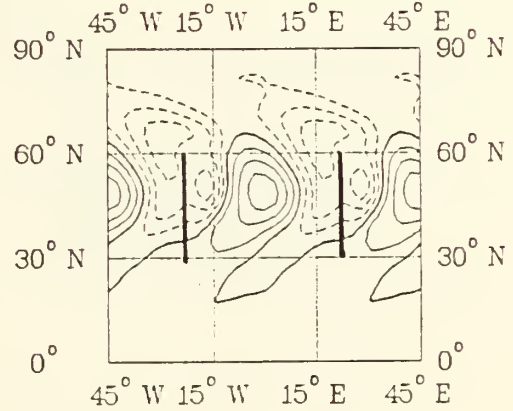
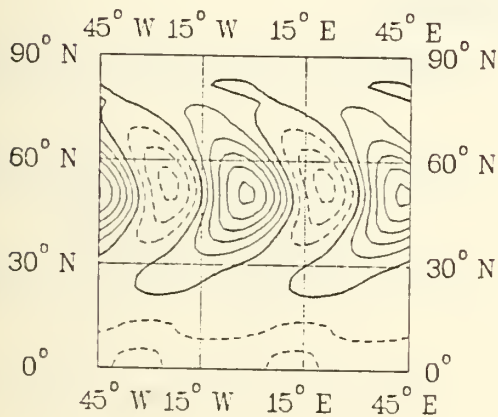
Sfc Pressure at Hour 24



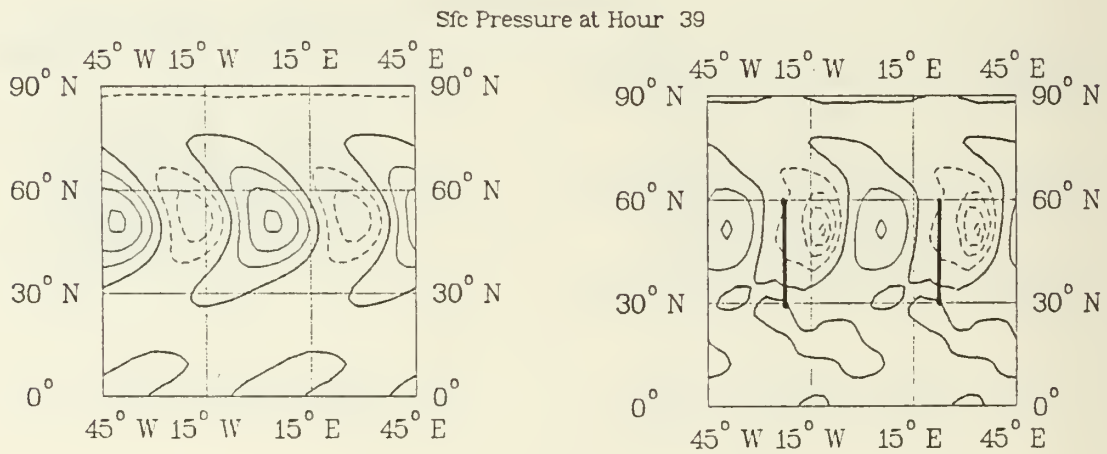
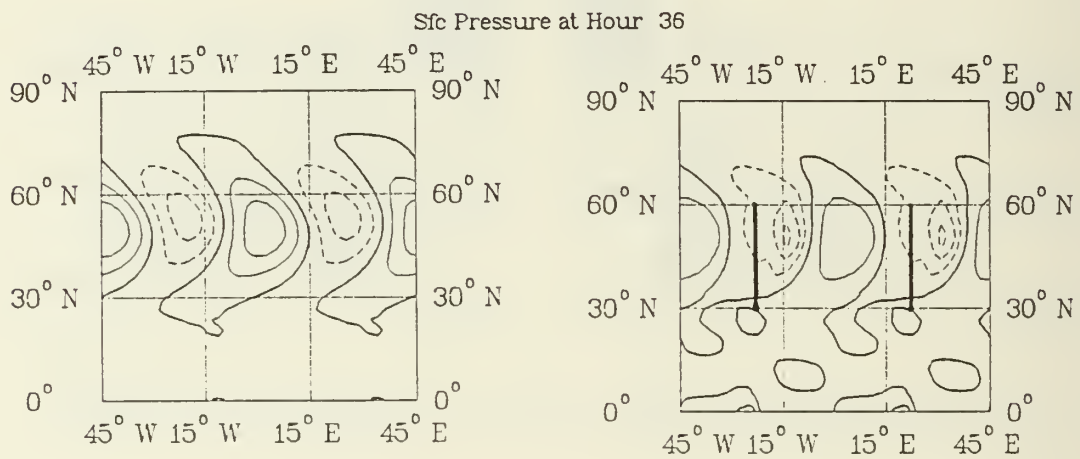
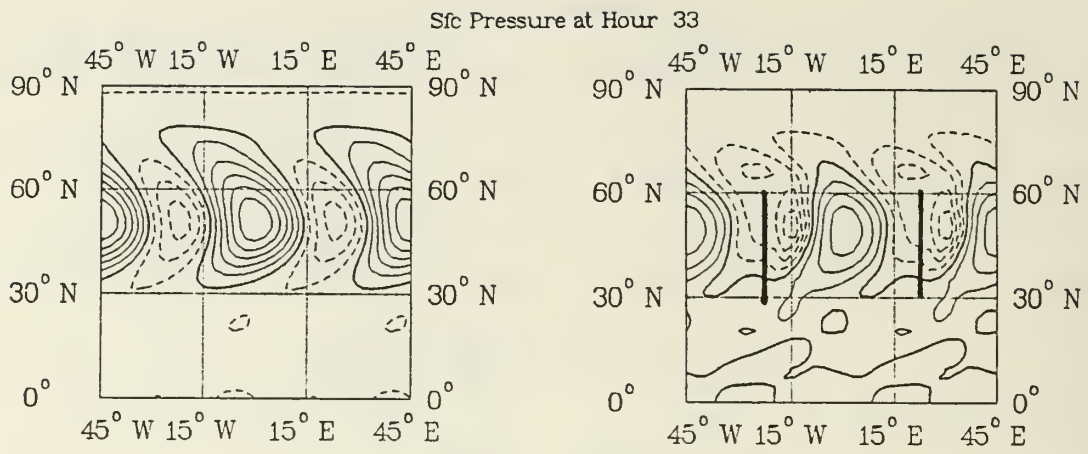
Sfc Pressure at Hour 27



Sfc Pressure at Hour 30

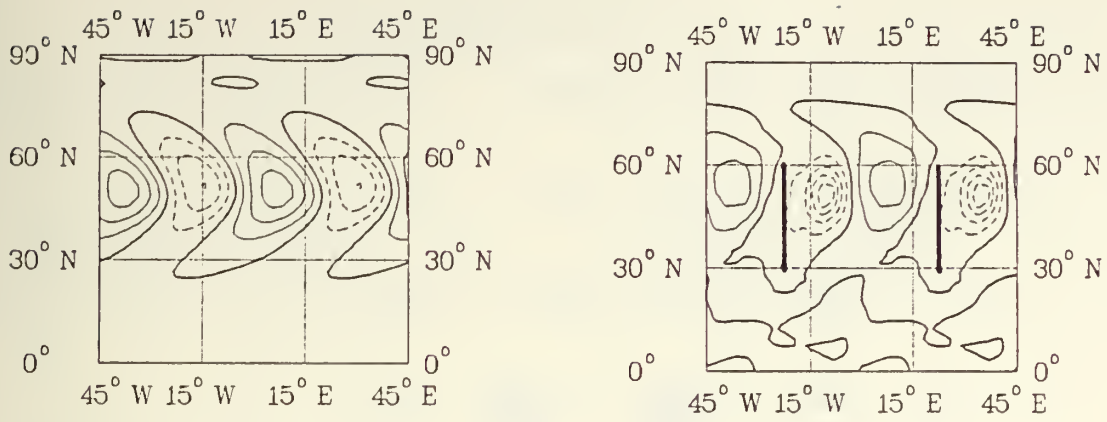


Figs. 13a, b, c

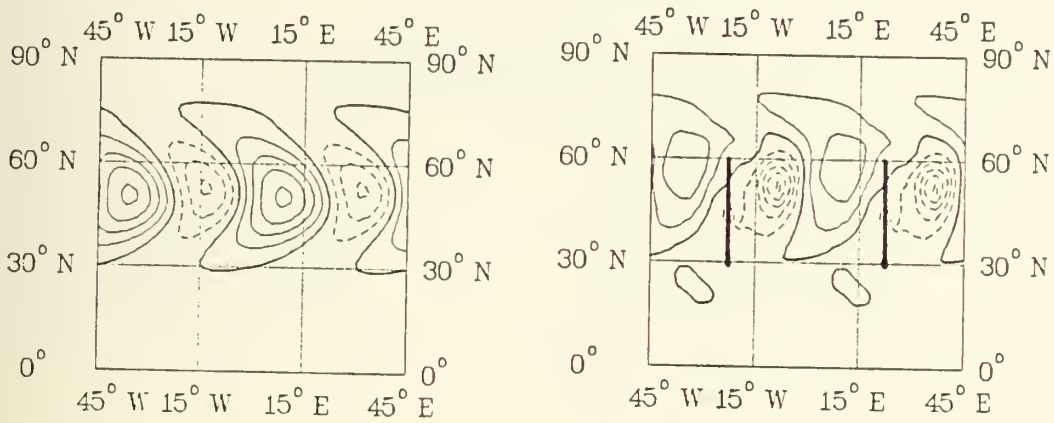


Figs. 13d, e, f

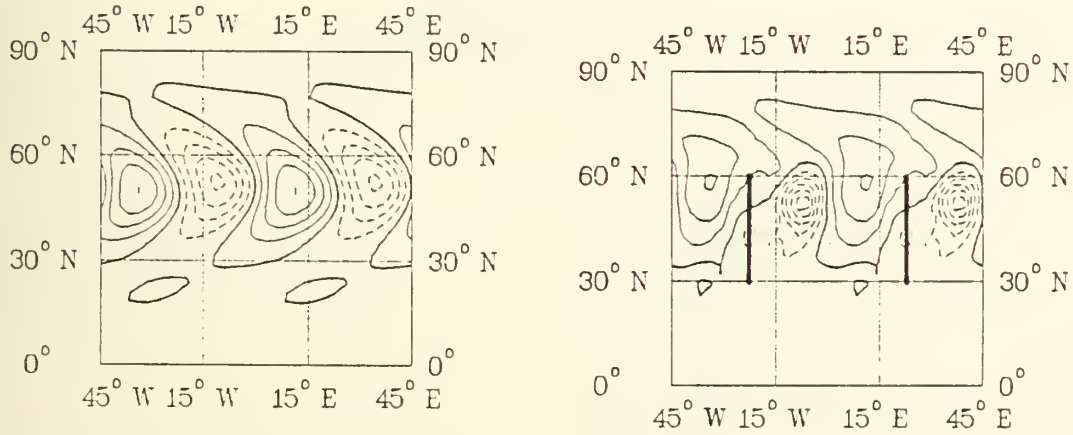
Sfc Pressure at Hour 42



Sfc Pressure at Hour 45



Sfc Pressure at Hour 48



Figs. 13g, h, i

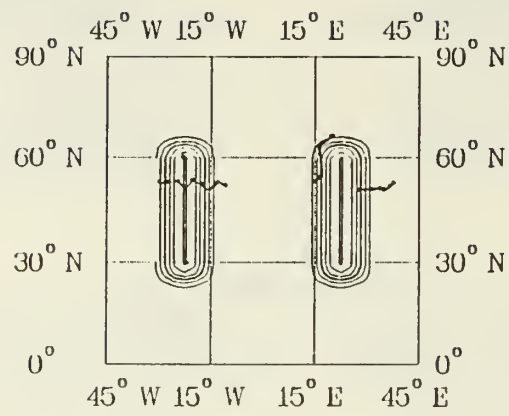
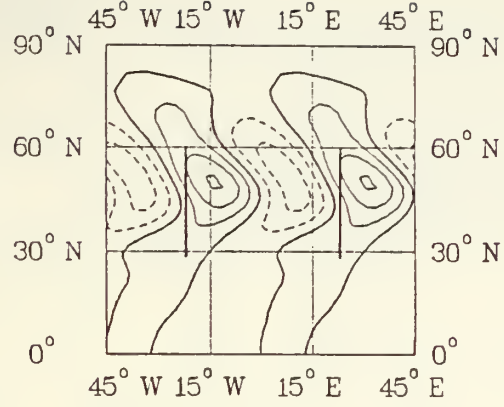
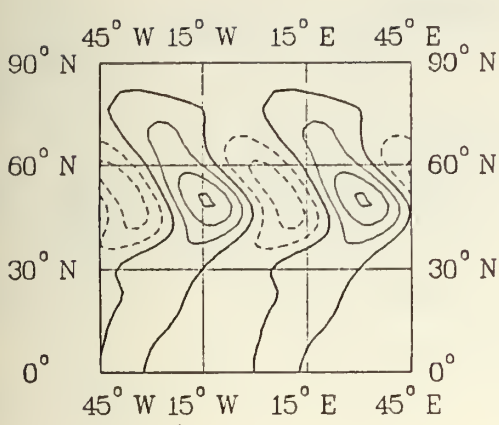
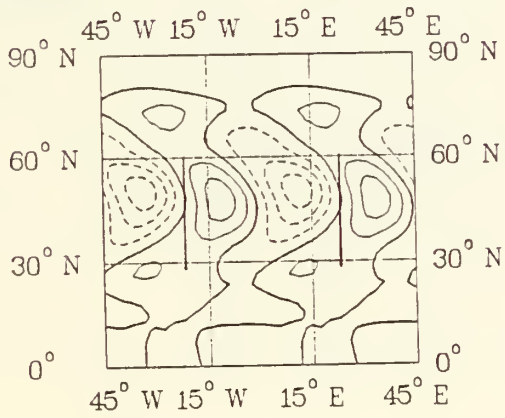
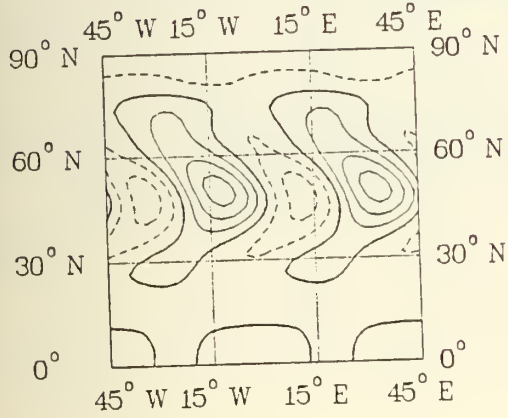


Fig. 13j

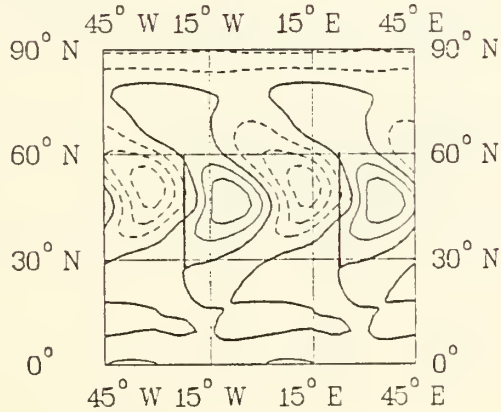
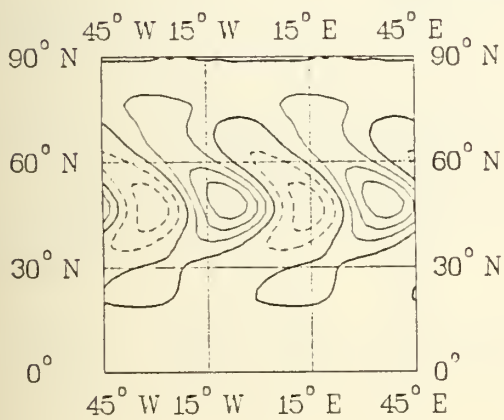
Sfc Pressure at Hour 24



Sfc Pressure at Hour 27

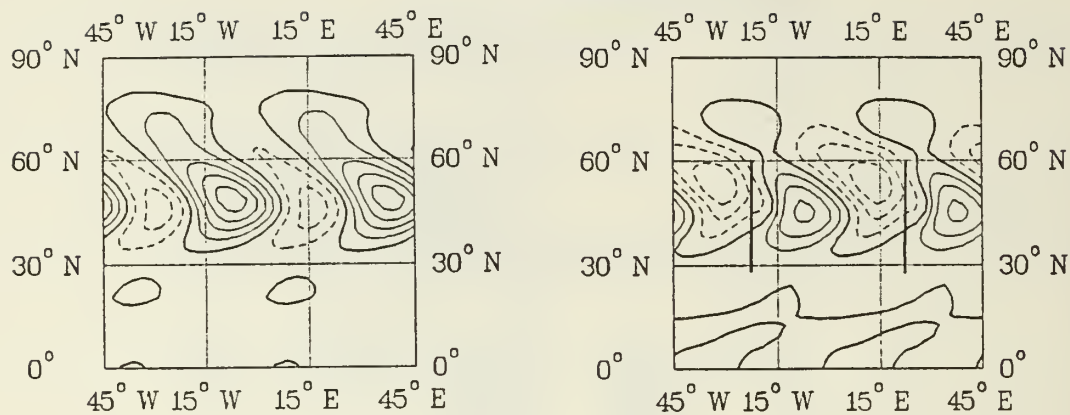


Sfc Pressure at Hour 30

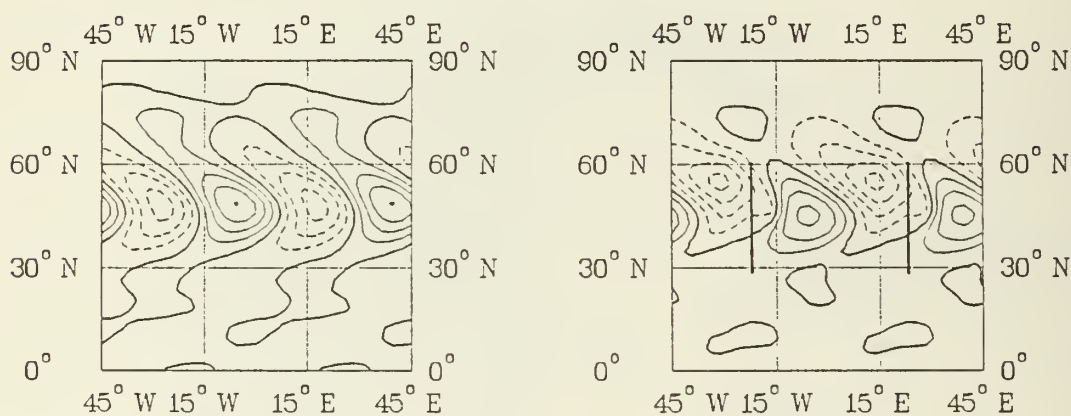


Figs. 14a, b,c

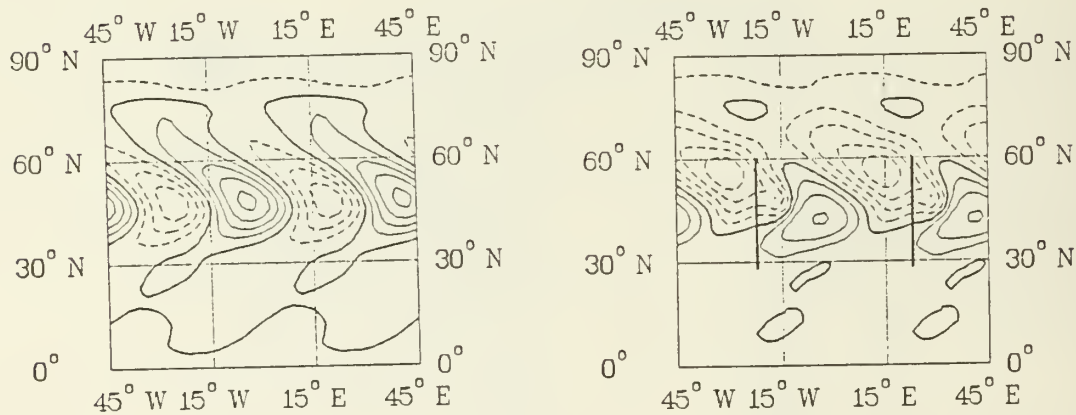
Sfc Pressure at Hour 33



Sfc Pressure at Hour 36

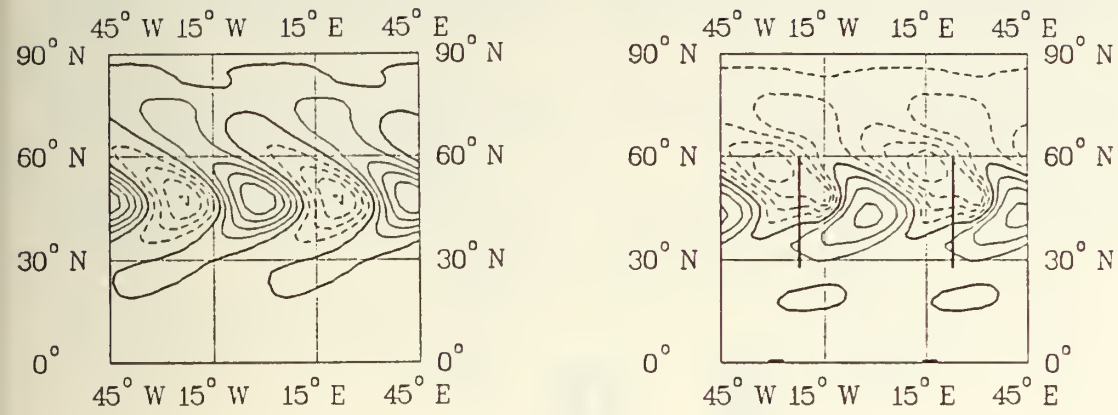


Sfc Pressure at Hour 39

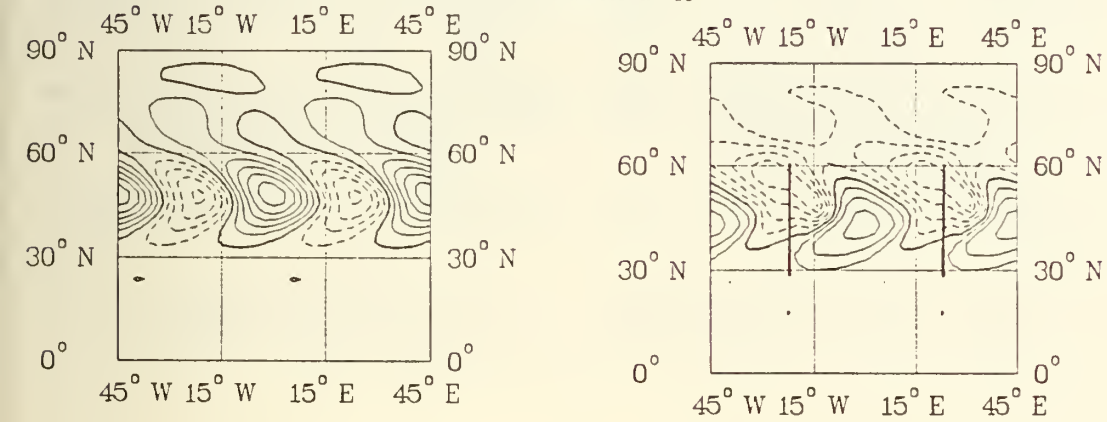


Figs. 14d, e, f

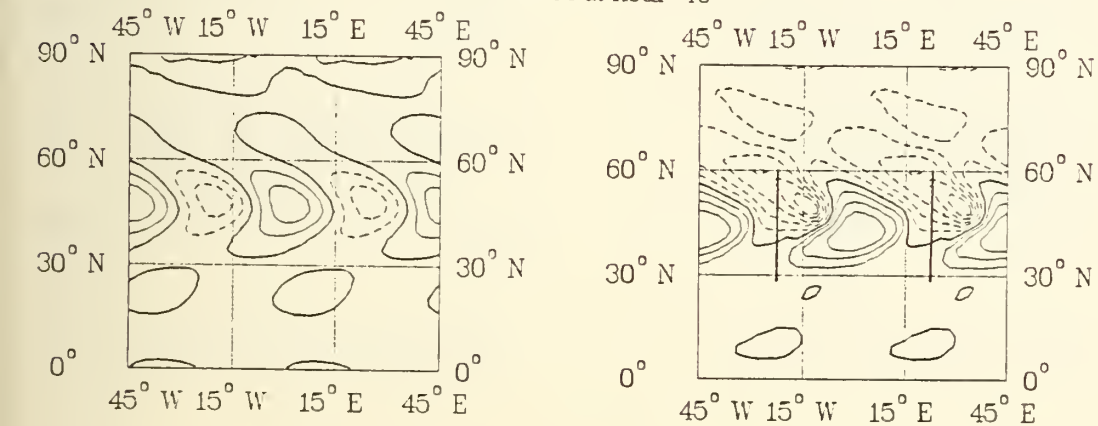
Sfc Pressure at Hour 42



Sfc Pressure at Hour 45



Sfc Pressure at Hour 48



Figs. 14g, h, i

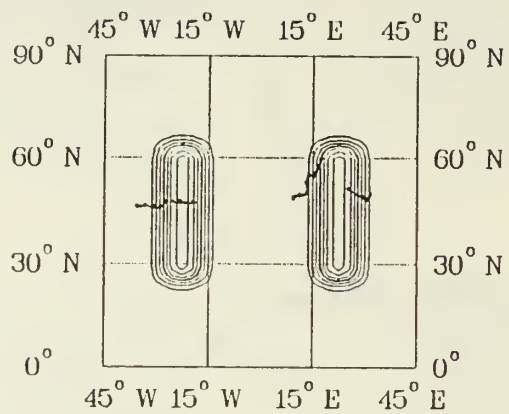
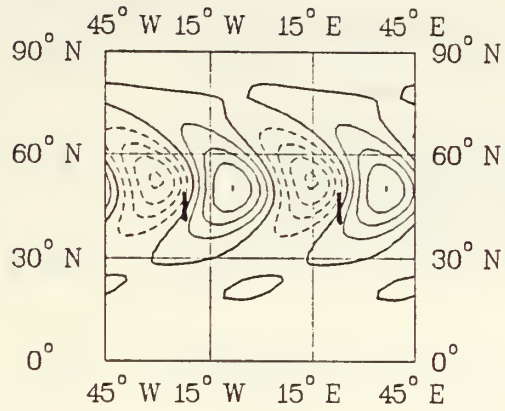
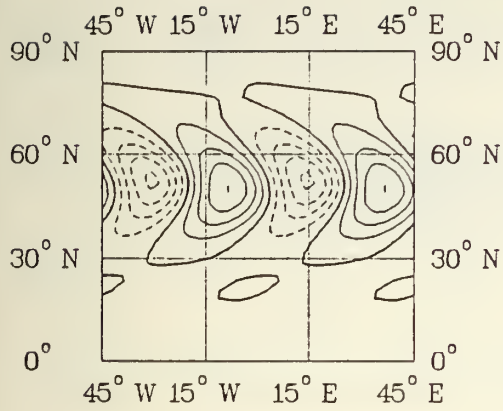
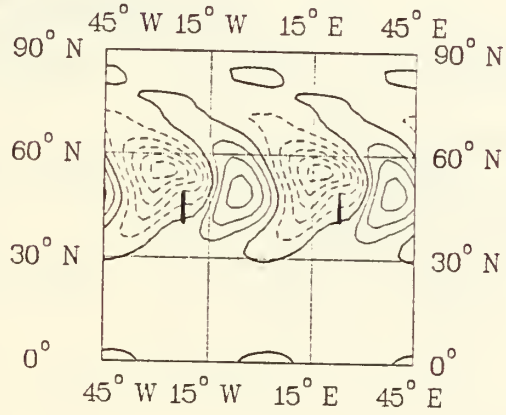
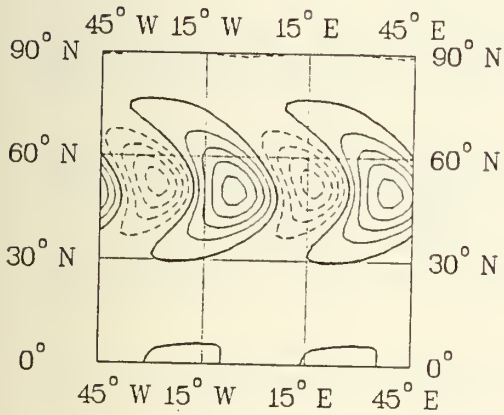


Fig. 14j

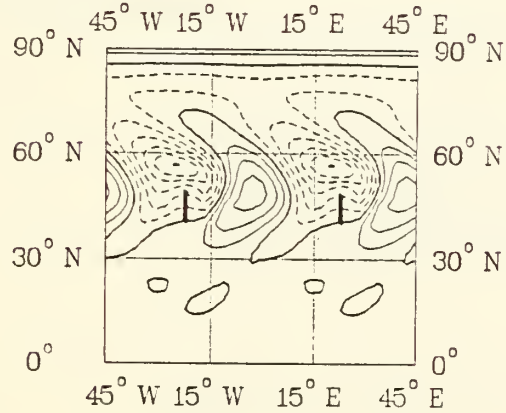
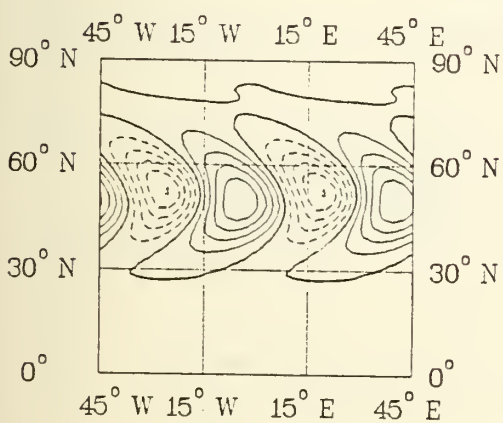
Sfc Pressure at Hour 48



Sfc Pressure at Hour 51

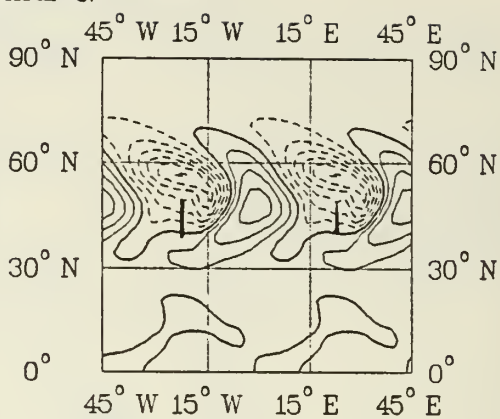
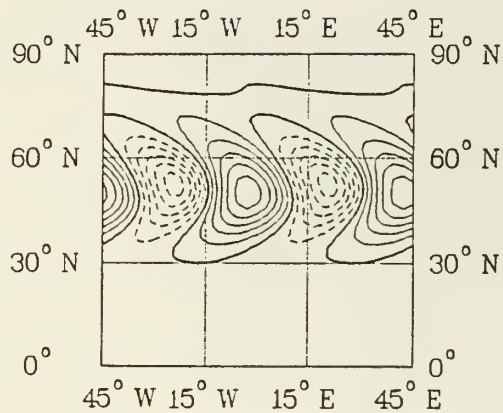


Sfc Pressure at Hour 54

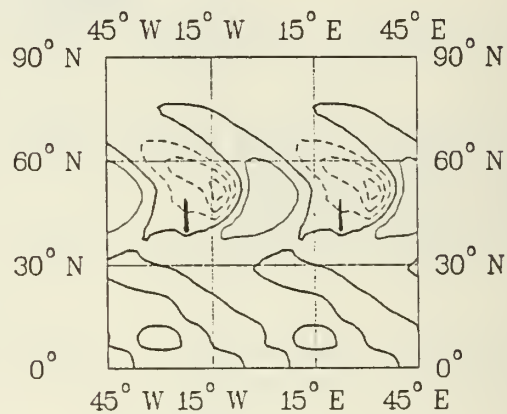
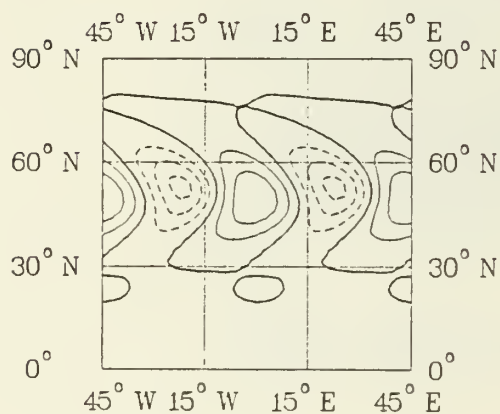


Figs. 15a, b,c

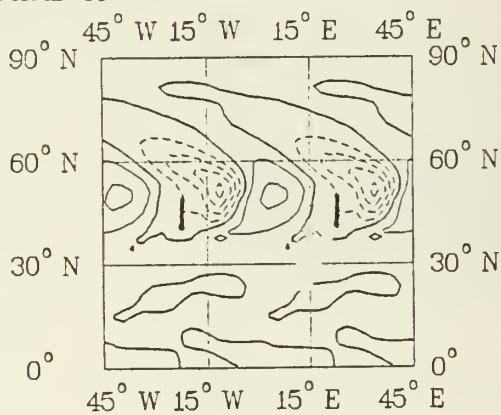
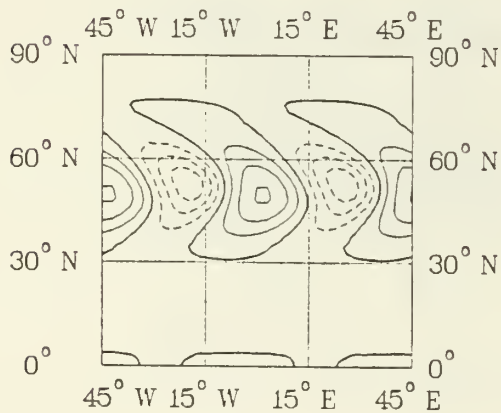
Sfc Pressure at Hour 57



Sfc Pressure at Hour 60

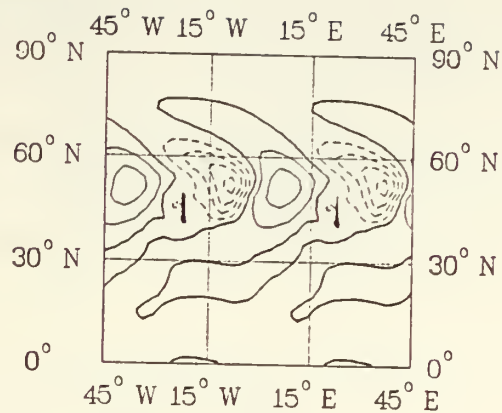
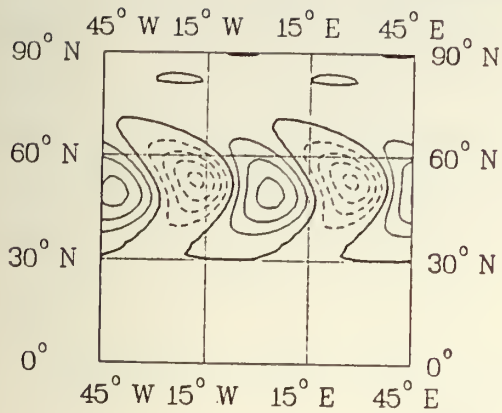


Sfc Pressure at Hour 63

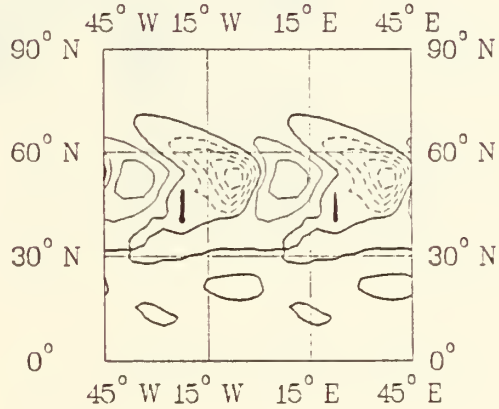
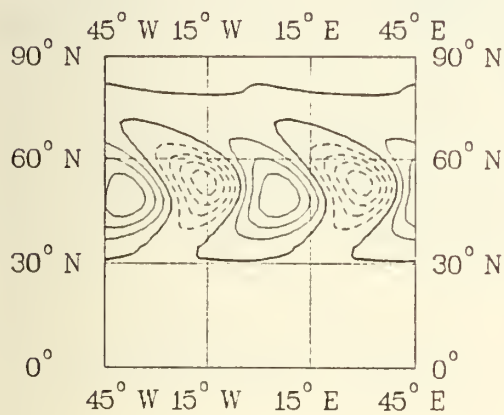


Figs. 15d, e, f

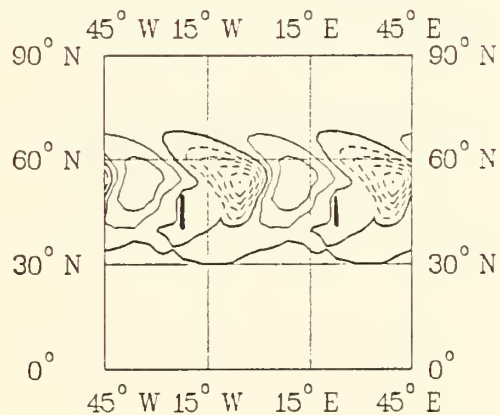
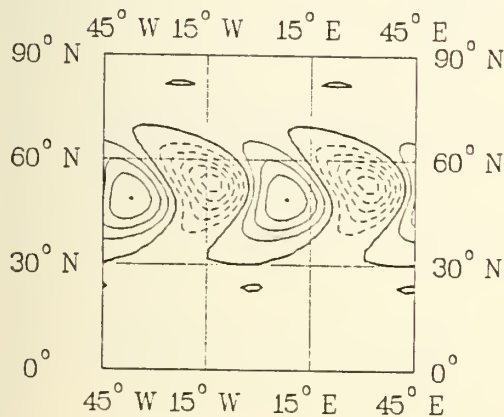
Sfc Pressure at Hour 66



Sfc Pressure at Hour 69



Sfc Pressure at Hour 72



Figs. 15g, h, i

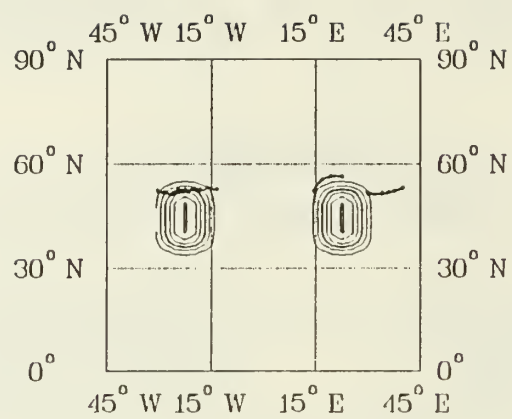
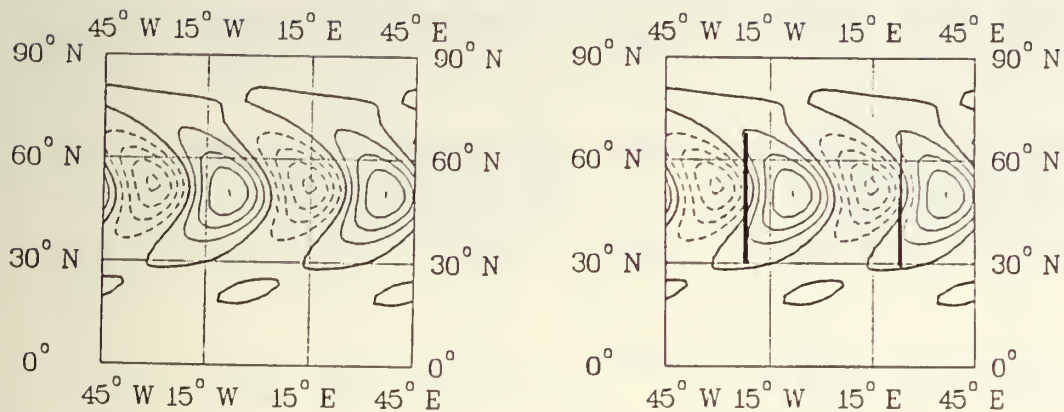
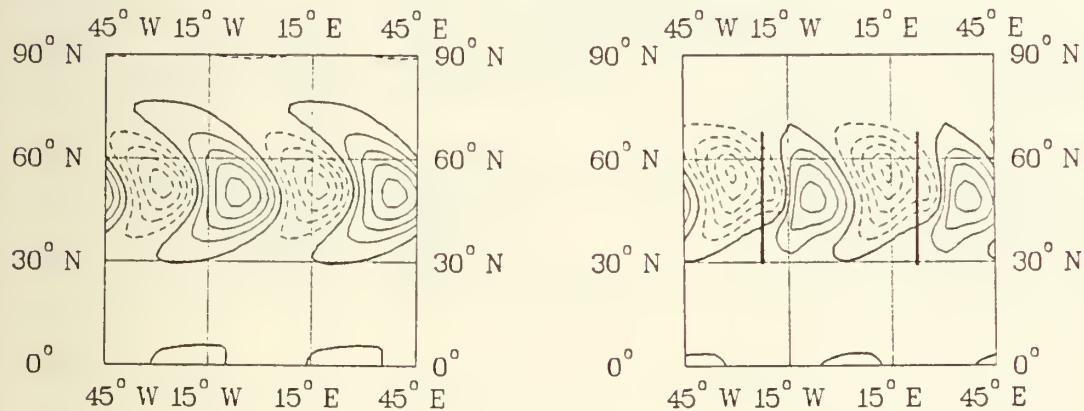


Fig. 15j

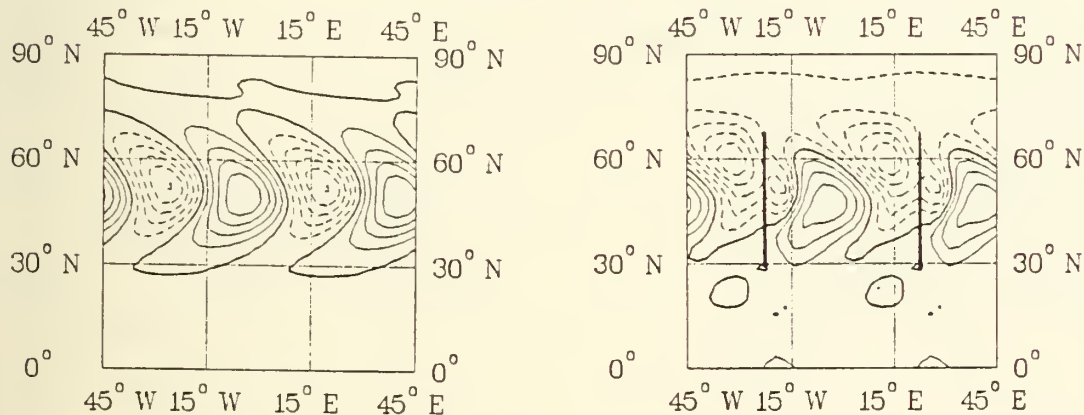
Sfc Pressure at Hour 48



Sfc Pressure at Hour 51

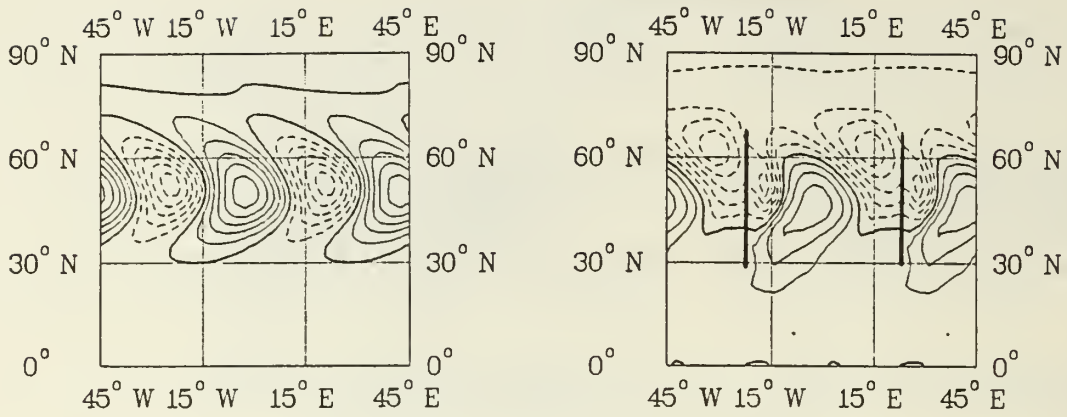


Sfc Pressure at Hour 54

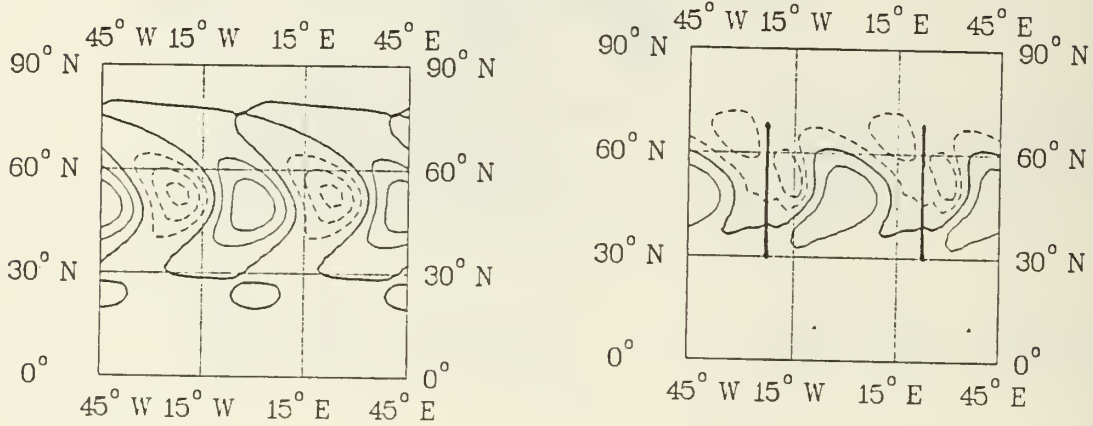


Figs. 16a, b, c

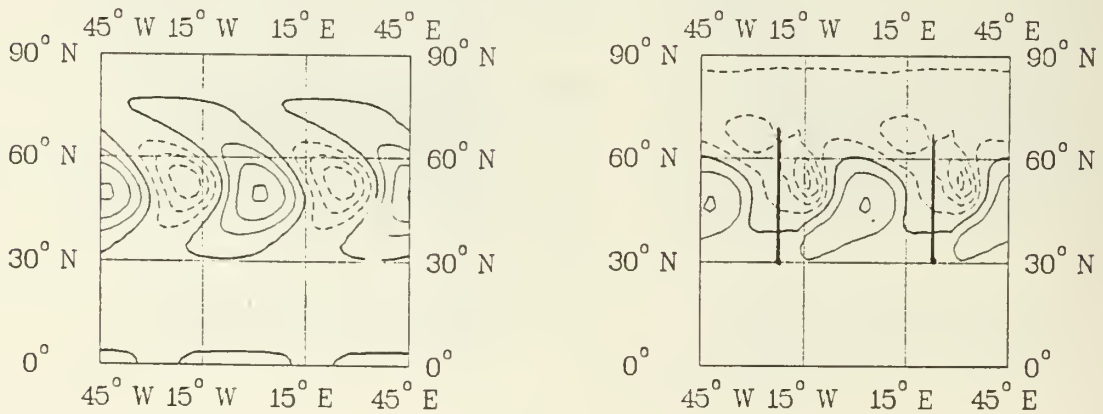
Sfc Pressure at Hour 57



Sfc Pressure at Hour 60

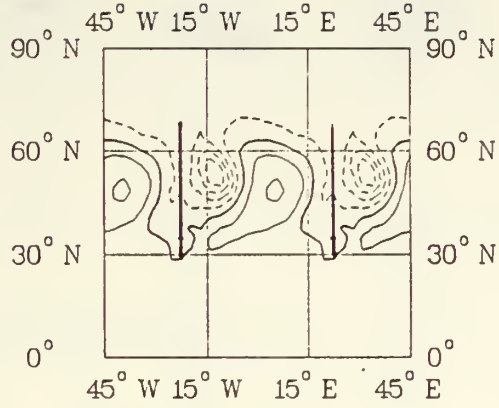
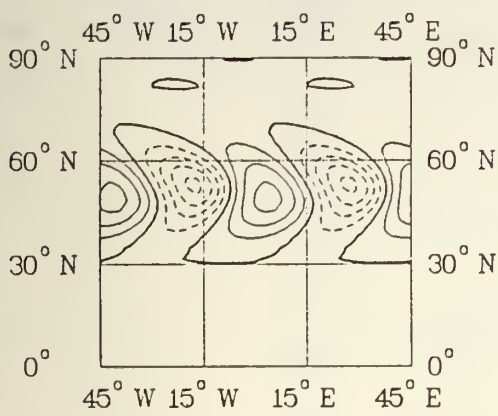


Sfc Pressure at Hour 63

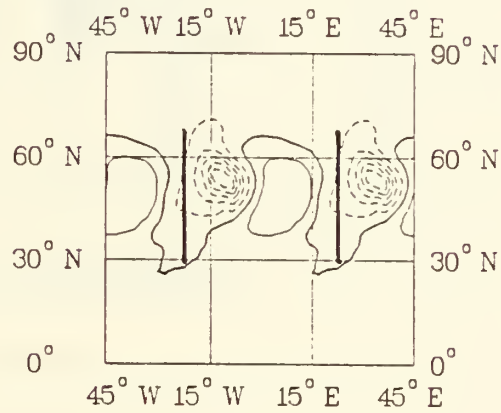
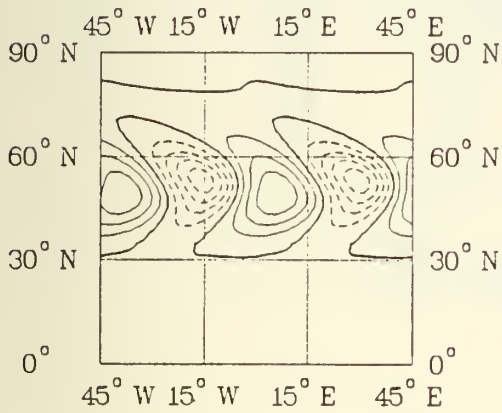


Figs. 16d, e, f

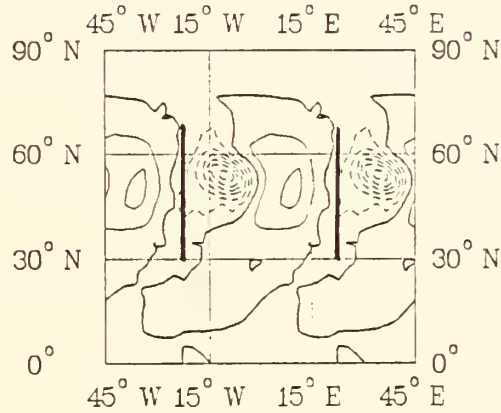
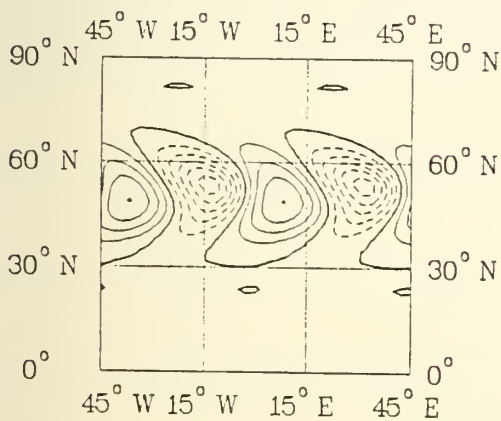
Sfc Pressure at Hour 66



Sfc Pressure at Hour 69



Sfc Pressure at Hour 72



Figs. 16g, h, i

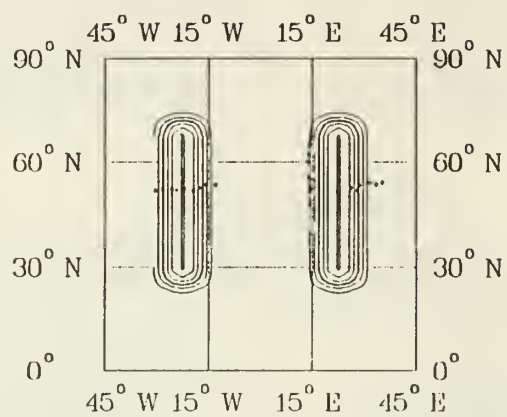


Fig. 16j

Model Run	Jet Width (° latitude)	Mountain Height (km)	t_0 (h)	Doubling Time (h)	Phase speed (° /day)	Lee Growth (mb)	Interaction
Control A	16	0.0	0	14	18		
Control B	8	0.0	0	24	14		
Ia	16	1.5	24	13	22	14.0	9%
Id	16	1.5	60	13	22	11.0	65%
IIa	16	3.0	24	14	25	14.0	12%
IIId	16	3.0	60	13	25	18.4	11%
IIIa	8	1.5	24	23	28	7.0	-9%
IIIc	8	1.5	48	17	28	7.0	33%
IVa	8	3.0	24	21	28	8.0	11%
IVc	8	3.0	48	32	20	7.0	11%
Va	16	3.0	48	20	28	-12.3	-17%
Vb	16	3.0	48	14	22	10.6	22%

Table 1 Summary of Experiments

List of Figures

- Fig. 1** Meridional cross section of the zonal mean wind. Contour interval = 5ms^{-1} ; 20ms^{-1} contour is emphasized: a) Control Run A; b) 'Control Run B.
- Fig. 2** Topographic surface for standard mountains.
- Fig. 3** Meridional cross section of the zonal wind for $\psi_M(0)$: a) away from the mountain; b) at the ridge. Contour interval = 5ms^{-1} ; 0ms^{-1} contour is emphasized. Negative values are dashed.
- Fig. 4** Sea level pressure for $\psi_M(t)$ for standard 1.5 km mountains. Heavy vertical lines indicate the location of the mountain ridge: a) $t = 0$; b) $t = 12\text{ h}$; c) $t = 24\text{ h}$. Contour interval = 5mb; 1030 mb contour is emphasized.
- Fig. 5** Sea level pressure for Control run A ($\psi_C(t)$): a) $t = 0$; b) $t = 24\text{ h}$; c) $t = 48\text{ h}$; d) $t = 72\text{ h}$; e) $t = 96\text{ h}$. Contour interval = 5mb; 1010 mb contour is emphasized.
- Fig. 6** Magnitude (solid line) and location (dashed line) of the minimum disturbance pressure (ψ'_C) for Control run A.
- Fig. 7** As in Fig. 6, but for Control run B.
- Fig. 8** Magnitude (solid lines) and location (dashed lines) of minimum sea level pressure for Control run A (heavy lines) and for Interactive run of Experiment I (thin lines). Time at which system was near the mountain ridge is indicated by heavy dotted lines.
- Fig. 9** As in Fig. 8, except for disturbance pressures.
- Fig. 10** Mountain topography used for Experiment V.
- Fig. 11** Surface pressure deviation fields for Control (left) and Interactive (right) runs at three hour intervals, and tracks of the disturbance centers for Experiment Ia. Heavy vertical lines in Interactive panels show position of ridge line. Contour intervals are 0.5 mb for hours 24-33; 1.0 mb for hours 36-48.
- Fig. 12** As in Fig 11, except for Experiment Id. Contour intervals are 2.0 mb for hours 60-78; 5.0 mb for hours 81-84.
- Fig. 13** As in Fig 11, except for Experiment IIa. Contour intervals are 0.5 mb for hours 24-33; 1.0 mb for hours 36-48.
- Fig. 14** As in Fig 11, except for Experiment IIIa. Contour intervals are 0.5 mb for hours 24-45; 1.0 mb for hour 45.
- Fig. 15** As in Fig 11, except for Experiment Va. Contour intervals are 1.0 mb for hours 48-57; 5.0 mb for hours 60-72.
- Fig. 16** As in Fig 11, except for Experiment Vb. Contour intervals are 1.0 mb for hours 48-57; 2.0 mb for hours 60-72.

st of Tables

ble 1 Summary of Experiments

Distribution List

No. of Copies

Defense Technical Information Center Cameron Station Alexandria, VA 22304-6145	2
National Science Foundation Division of Grants and Contracts Post-Award Project Branch Washington, DC 20440	1
Prof. Gordon Schacher (Code 06) Dean of Science and Engineering Naval Postgraduate School Monterey, CA 93943-5000	1
Library (Code 0142) Naval Postgraduate School Monterey, CA 93943-5000	2
Research Administration (Code 012) Naval Postgraduate School Monterey, CA 93943-5000	1
Dr. M. A. Rennick MMDS Building 702 Fleet Numerical Oceanography Center Monterey, CA 93943-5000	2
Dr. Robert J. Renard (Code 63Rd) Department of Meteorology Naval Postgraduate School Monterey, CA 93943-5000	1
Prof. R. T. Williams (Code 63Wu) Department of Meteorology Naval Postgraduate School Monterey, CA 93943-5000	5
Ms. Pamela Stephens Global Atmospheric Research Program National Science Foundation Washington, DC 20550	1
AIT-CCNAA Cooperative Science Program Division of International Programs National Science Foundation Washington, DC 20550	1

DUDLEY KNOX LIBRARY



3 2768 00337476 0